

(14)

DOT/FAA/CT-82/19

Antimisting Kerosene Atomization and Flammability

R. Fleeter
R. A. Petersen
R. D. Toaz
A. Jakub
V. Sarohia

Jet Propulsion Laboratory
California Institute of Technology
Pasadena, California
(JPL Publication 82-40)

Prepared for
U.S. Department of Transportation,
Federal Aviation Administration
through an agreement with the
National Aeronautics and Space Administration

July 1982

Interim Report

This document is available to the U.S. public
through the National Technical Information
Service, Springfield, Virginia 22161.

DTIC
OCT 25 1982
H



US Department of Transportation
Federal Aviation Administration
Technical Center
Atlantic City Airport, N.J. 08405

82 10 25 069

ADA 120671

82 10 25 069

NOTICE

This document is disseminated under the sponsorship of the Department of Transportation in the interest of information exchange. The United States Government assumes no liability for the contents or use thereof.

The United States Government does not endorse products or manufacturers. Trade or manufacturer's names appear herein solely because they are considered essential to the object of this report.

TECHNICAL REPORT STANDARD TITLE PAGE

1. Report No. DOT/FAA/CT-82/19	2. Government Accession No. DOT-A-82-0171	3. Recipient's Catalog No.	
4. Title and Subtitle Antimisting Kerosene Atomization and Flammability		5. Report Date September 1, 1981	
		6. Performing Organization Code	
7. Author(s) R. Fleeter, R.A. Petersen, R.D. Toaz, A. Jakub, V. Sarohia		8. Performing Organization Report No. JPL Publication 82-40	
9. Performing Organization Name and Address JET PROPULSION LABORATORY California Institute of Technology 4800 Oak Grove Drive Pasadena, California 91109		10. Work Unit No.	
		11. Contract or Grant No. DTFA 03-80-A-00215	
		13. Type of Report and Period Covered	
12. Sponsoring Agency Name and Address Department of Transportation Federal Aviation Administration Technical Center Atlantic City Airport, N.J. 08405		14. Sponsoring Agency Code	
15. Supplementary Notes			
<p>16. Abstract</p> <p>Experimental results are presented exploring various parameters found to affect the flammability of antimisting kerosene (Jet A + polymer additive). Digital image processing has been integrated into a new technique for measurement of fuel spray characteristics. This technique has been developed to avoid many of the error sources inherent to other spray assessment techniques and has been applied to the study of engine fuel nozzle atomization performance with Jet A and antimisting fuel. Aircraft accident fuel spill and ignition dynamics have been modeled in a steady state simulator allowing flammability to be measured as a function of airspeed, fuel flow rate, fuel jet Reynolds number and polymer concentration. The digital imaging technique has been employed to measure spray characteristics in this simulation and these results have been related to flammability test results. Scaling relationships have been investigated through correlation of experimental results with characteristic dimensions spanning more than two orders of magnitude.</p>			
17. Key Words (Selected by Author(s)) Antimisting kerosene Safety fuels Aircraft fire safety		18. Distribution Statement	
19. Security Classif. (of this report)	20. Security Classif. (of this page)	21. No. of Pages 176	22. Price

I. Acknowledgments

This report presents the results of one phase of research carried out at the Jet Propulsion Laboratory, California Institute of Technology, through NASA Task Order RD152, Amendments 249, 250, 252 and was sponsored by the Department of Transportation, Federal Aviation Administration under Agreement No. DTFA03-80-A-00215. The authors extend their gratitude to Mr. Stephen Imbrogno, FAA Technical Center Project Manager, for many valuable technical suggestions throughout this program. The assistance of M. B. Green, M. R. Smither, and W. Bixler is appreciated for fabrication and assembly of the experimental setup.

Accession For	
NTIS GRA&I	<input checked="checked" type="checkbox"/>
DTIC TAB	<input type="checkbox"/>
Unannounced	<input type="checkbox"/>
Justification	
By	
Distribution/	
Availability Codes	
A all and/or	
Dist	Special
<i>A</i>	



TABLE OF CONTENTS

	PAGE
Abstract -----	i
I. Acknowledgements -----	ii
Table of Contents -----	iii
II. Summary -----	v
III. Introduction -----	1
IV. Facilities and Instrumentation -----	4
4.1 Facilities -----	4
4.1.1 Wing Shear Facilities -----	4
4.1.2 Flammability Comparison Test Apparatus -----	6
4.1.3 Nozzle Spray Facility -----	6
4.2 Instrumentation -----	12
4.2.1 Flammability Measurements -----	15
V. Image Processing -----	20
5.1 Introduction -----	20
5.1.1 Methods of Drop Measurement -----	20
5.1.2 Image Processing in Spray Measurements -----	22
5.2 System Overview -----	24
5.3 Illumination -----	30
5.4 Image Recording -----	31
5.5 Image Processing Hardware -----	36
5.6 Image Processing Software Development and Methodology ----	38
5.7 Control Experiment -----	68

TABLE OF CONTENTS (cont.)

	PAGE
VI. Experimental Results -----	77
6.1 Flammability Measurements -----	77
6.1.1 Fuel Mass Flow Effects -----	84
6.1.2 Orifice Effects -----	86
6.1.3 Polymer Concentration Effects -----	94
6.1.4 Radiometer Measurements -----	94
6.1.5 Quality Control and Deterioration Effects -----	102
6.2 Drop Formation and Measurements -----	102
6.2.1 Mini Wing Shear -----	104
6.2.2 Drop Size Measurements -----	105
6.3 Nozzle Flow Behavior -----	140
VII. Scaling Considerations -----	147
7.1 Dimensional Analysis -----	147
7.2 Fuel Jet Parameter Space -----	148
7.3 Aerodynamic Parameter Space -----	152
7.4 Aerodynamic Shearing -----	154
VIII. Conclusions -----	156
Appendix I Derivation of the Nondimensional Temperature, θ , as a Measure of Flammability -----	158
Appendix II AMK Quality Control Measurements -----	162
References -----	163

FIGURES

- Figure 1. Small-scale wing shear facility.
- Figure 2. Schematic diagram of the flammability comparison test apparatus (FCTA)
- Figure 3. Calibration Results for the FCTA Supplied by the FAA: airspeed vs. supply pressure.
- Figure 4. Calibration Results for the FCTA Supplied by the FAA: fuel mass flow vs. speed control setting.
- Figure 5. Nozzle spray facility for fuel atomization measurement (view facing forward).
- Figure 6. Nozzle spray facility for fuel atomization measurement (side view).
- Figure 7. Turbine flowmeter calibrations for modified fuel: (a) 1/2 inch gauge; (b) 1 inch gauge.
- Figure 8. Imaging data paths; formation of initial images may be accomplished with photographic processing (left) or analogue electronic devices (right).
- Figure 9. Image digitization paths; either a microdensitometer (left) or a video digitizer (right) is used.
- Figure 10. Image processing paths; IBM 370/158 or PDP 11/34 computers may be used with VICAR or Mini-VICAR software packages.
- Figure 11. Laser illumination configurations (a) forward scatter; (b) sheet illumination.
- Figure 12. Optical configuration for laser sheet illumination.
- Figure 13. Photographic configuration for nozzle spray imaging.

- Figure 14. Mosaic construction of nozzle spray images.
- Figure 15. Jet A fuel spray images resolved digitally with a 2000 x 2000 pixel array.
- Figure 16. Portion of the Jet A fuel spray corresponding to 1 cm² on the negative, 512 x 512 pixel array, 20 μm microdensitometer aperture and spacing.
- Figure 17. Portion of the Jet A fuel spray corresponding to 0.26 cm² on the negative 512 x 512 pixel array, 20 μm microdensitometer aperture with 10 μm spacing (50% oversampling).
- Figure 18. Portion of the Jet A fuel spray corresponding to 0.26 cm² on the negative 512 x 512 pixel array, 10 μm microdensitometer aperture and 10 μm spacing (no oversampling).
- Figure 19. Portion of the Jet A fuel spray corresponding to 6.6 mm² on the negative, 512 x 512 pixel array, 10 μm microdensitometer aperture and 5 μm spacing (50% oversampling).
- Figure 20. Portion of the Jet A fuel spray corresponding to 6.6 mm² on the negative, 512 x 512 pixel array, 5 μm microdensitometer aperture and 5 μm spacing (no oversampling).
- Figure 21. Portion of the Jet A fuel spray corresponding to 2.4 mm² on the negative, 512 x 512 pixel array, 5 μm microdensitometer aperture, 3 μm spacing (40% oversampling).
- Figure 22. Three subimages composing the Jet A sea level takeoff spray image window 2 cm axially from the nozzle. Stretching has been performed individually to optimize resolution within each subimage (a) first third, (b) second third (c) final third.
- Figure 23. Window configuration for fuel spray image processing.
- Figure 24. Three subimages composing the Jet A sea level takeoff spray image window, 2 cm axially from the nozzle. A single stretching technique has been applied uniformly to all subimages to allow visual mosaicing. (a) first third (b) second third, (c) final third.

- Figure 25. Threshold derived outline; image DN cutoff 22.
- Figure 26. Threshold derived outline; image DN cutoff 18.
- Figure 27. Filtered outline image; DN cutoff 18, 3 x 3 filter, center triple weighted.
- Figure 28. Filtered outline image. DN cutoff 18, 3 x 3 filter, center double weighted.
- Figure 29. Filtered outline image. DN cutoff 18, 3 x 3 filter, center single weighted (uniform weighting).
- Figure 30. Droplet collection apparatus.
- Figure 31. Photograph of droplet impression on coated glass slide (see fig. 44 for scale).
- Figure 32. Photograph of rule used to scale impression photos (smallest division spacing is 10 μm).
- Figure 33. Results of slide impaction and imaging measurement of fuel spray droplets.
- Figure 34. Matrix of wing shear operating conditions. o 0.30% FM-9, .25% FM-9; .20% FM-9; --- nominal matrix.
- Figure 35. Wing shear combustion temperature vs. downstream distance for 0.30% FM-9. Distance is normalized by exit dimension of contraction section. Letters F, M, P refer to fail, marginal, and pass (see text for details of pass/fail criterion).
- Figure 36. Wing shear combustion temperature vs. downstream distance for 0.25% FM-9.
- Figure 37. Wing shear combustion temperatures vs. downstream distance for 0.20% FM-9.

- Figure 38. Average rates of change of temperatures with downstream distance as a function of airspeed. Solid symbols denote fails (a) 0.30% FM-9, (b) 0.25% FM-9 (c) 0.20% FM-9 (see text for discussion of pass/fail criterion).
- Figure 39. Combustion temperatures for 0.30% FM-9 vs. peak airspeed measured with FCTA. Thermocouple located 25 cm downstream from torch ($x/D = 10$).
- Figure 40. Reduced wing shear temperature vs. downstream distance for Jet A.
- Figure 41. Reduced FCTA temperature vs. airspeed for 0.30% FM-9.
- Figure 42. Reduced wing shear temperature vs. fuel massflow. Thermocouple located at $x/d = 12.7$. (a) Airspeed 61.5 m/s (b) Airspeed 3 m/s (c) airspeed 99.3 m/s.
- Figure 43. Envelope of reduced temperatures vs. airspeed for wing shear and FCTA, using 0.30% FM-9. Thermocouple locations were 10 mixing tube diameters behind torch (FCTA) and 10.6 blower diameters behind torch (wing shear).
- Figure 44. Time dependent behavior of modified fuel at various shearing rates, 23.9°C (from ref. 41).
- Figure 45. Reduced temperature vs. shearing rates for various orifice diameters. The critical shearing rate is shown by dashed line. Open figures are mini wing shear data. Closed figures are FCTA data.
- Figure 46. Reduced temperature 10 diameters behind torch vs. jet Reynolds number for 0.30% FM-9 with various orifice sizes. Open symbols: airspeed = 80 ± 2 m/sec; solid symbols: airspeed = 96 ± 1 m/sec.
- Figure 47. Wing shear and FCTA temperature vs. polymer concentration for various fuel flow rates, airspeeds, and batch numbers. Straight line represents a power law relationship.
- Figure 48. Comparison between thermocouple and radiometer measurements of flammability vs. polymer concentration. The radiometer was focused on the thermocouple and measured equivalent black body temperatures. Airspeed = 77 m s⁻¹.

- Figure 49. Comparison between thermocouple and radiometric calorimeter, measurements of flammability of 0.25% FM-9 with airspeed and fuel flow rate. (a) Rate of change of temperature with distance, replotted from figure 50; (b) radiant heat flux measured with the calorimeter located 3.0 m off-axis opposite the torch.
- Figure 50. Comparison between estimates of combustion efficiency based on reduced temperatures and reduced radiant flux for 0.25% FM-9. (a) Reduced temperatures measured at $x/d = 12.7\%$, radiation efficiency defined by eqn (6.1-5). (See text for discussion of pass/fail criterion).
- Figure 51. Summary of quality control test results. Batch numbers are supplied by Imperial Chemical Industries, Ltd. Flammability was measured with the FCTA using procedures summarized in Appendix II.
- Figure 52. Mini wing shear jet breakup photographic perspective. An inch scale ruler is attached to the 1 inch orifice. The ignitor torch flange is visible at the extreme left.
- Figure 53. Breakup of a Jet A by a counterflowing airstream; liquid velocity 1.5 m s^{-1} , air velocity 96 m s^{-1} .
- Figure 54. Breakup of AMK by a counterflowing airstream; liquid velocity 0.5 m s^{-1} , air velocity 96 m s^{-1} .
- Figure 55. Jet A fuel spray photographed under photo-strobe illumination of $\sim 1 \text{ ms}$ duration.
- Figure 56. Jet A fuel spray photographed under pulsed laser sheet lighting of $\sim 1 \text{ } \mu\text{s}$ duration.
- Figure 57. Jet A fuel spray photographed under pulsed laser sheet lighting of $\sim 25 \text{ ns}$ duration.
- Figure 58. Spray of undegraded AMK at cruise flow rate.
- Figure 59. Spray of 84% degraded AMK at cruise flow rate.
- Figure 60. Spray of 90% degraded AMK at cruise flow rate.

Figure 61. Spray of 93% degraded AMK at cruise flow rate.

Figure 62. Atomization of 93% degraded AMK at ignition fuel flow rate.

Figure 63. Atomization of Jet A at ignition fuel flow rate.

Figure 64. Portion of the Jet A fuel spray image 5 cm downstream of the nozzle cruise flow rate, after application of image processing.

Figure 65. Histogram of drop sizes for the Jet A, cruise fuel flow rate spray, 5 cm downstream of the nozzle.

Figure 66. Appearance of liquid spray formed in the mini wing shear facility. Downstream (right) of the nozzle is the oxyacetylene torch with shroud used for fuel spray ignition.

Figure 67. Viewing window for mini wing shear drop size measurements. The torch flame is visible below the 3 inch mark on the ruler.

Figure 68. Drops formed by breakup of a Jet A + 0.30% FM-9 in an airstream of 96 m s^{-1} velocity (fire test failed under these conditions).

Figure 69. Drops formed by break up of Jet A + 0.30% FM-9 in an airstream of 60 m s^{-1} velocity (fire test passed under these conditions).

Figure 70. Histogram of drop characteristic length observed at the mini wing shear ignition source; Jet A + 0.30% Fm-9 fuel, 60 m s^{-1} airspeed. (Fire suppression test passed under these conditions.)

Figure 71. Histogram of drop characteristic length observed at the mini wing shear ignition source; Jet A + 0.30% FM-9 fuel, 96 m s^{-1} airspeed (fire suppression test failed under these conditions).

Figure 72. Histogram of drop characteristic length observed at the mini wing shear ignition source; Jet A + 0.25% FM-9 fuel, 60 m s^{-1} air speed (Fire suppression test passed marginally under these conditions).

Figure 73. Histogram of drop characteristic length observed at the mini wing shear ignition source; Jet A + 0.20% FM-9 fuel, 60 m s^{-1} airspeed (fire suppression test failed under these conditions).

- Figure 74. Histogram of drop characteristic length observed at the FCTA ignition source; Jet A + 0.25% FM-9 fuel, 6.1 atm accumulator pressure (fire suppression test passed under these conditions).
- Figure 75. Histogram of drop characteristic length observed at the FCTA ignition source; Jet A + 0.20% FM-9 fuel, 6.1 atm accumulator pressure (fire suppression test failed under these conditions).
- Figure 76. Total number of droplets identified for each test, normalized to the number identified in the test corresponding to failure of the fire suppression test.
- Figure 77. Fuel mass flow rate as a function of nozzle pressure drop; primary jet.
- Figure 78. Fuel mass flow rate as a function of nozzle pressure drop; secondary jet.
- Figure 79. Nondimensional analysis of nozzle calibration data.
- Figure 80. Reduction of nozzle calibration data using derived viscosity values.
- Figure 81. Parameter space relevant to fuel jet similarity. The Deborah number is referred to the fuel critical shear rate, γ_c .
- Figure 82. Parameter space relevant to aerodynamic similarity of fuel breakup and atomization. The Deborah number is referred to the fuel critical shear rate, γ_c .
- Figure 83. Comparison of pass-fail boundaries measured in JPL and FAA wing shear experiments. JPL data, from figure 50; FAA data, from ref. 5. Each set of curves denotes boundaries of marginal regions.

II. Summary

Results of an experimental and analytical investigation on the atomization and flammability of a modified aircraft gas turbine engine fuel (Jet A with FM-9 polymer additive of Imperial Chemical Industries, Ltd.) are presented in this report. Both the ability of the fuel to resist ignition during an aircraft crash with fuel spillage and to atomize in a turbojet engine combustor nozzle have been investigated. Image processing techniques have been developed to characterize the fuel sprays formed during simulations of aircraft crashes and by engine fuel nozzles. Methods for automated measurement of drop size and density in fuel sprays and flammability tests have been developed to study fuel spray ignition in aircraft crashes.

A steady state crash simulator, the mini wing shear device, was constructed for the flammability studies. The apparatus consists of a wing section of 8 cm chord immersed in the potential core of a free air jet. Fuel may be sprayed upwind through an orifice in the wing leading edge. Aerodynamic shearing forces and the turbulence of the fuel jet then combine to disintegrate the jet and atomize the fuel. The fuel mist formed is convected downstream where it passes an ignition region formed by an oxyacetylene torch. The temperature and heat released by the burning fuel are measured with thermocouples, a radiometer and a calorimeter for a range of fuel and air mass flow rate, fuel jet Reynolds number, antimisting polymer concentration, fuel temperature and fuel supply line inner diameter. Results are compared with those of larger and smaller scale flammability test facilities to assess the effects of physical scale and experimental consistency.

Analysis of the dynamics of jet breakup and atomization has lead to an organization of scaling studies by four nondimensional variables: the hydrodynamic Deborah number of the fuel jet, De_L , the aerodynamic Deborah number

De_A , the hydrodynamic Reynolds number of the fuel jet, Re_L , and the Weber number, We . It is shown that because of the diverse nature of the scaling parameters, no small scale model can replicate all aspects of the full scale event simultaneously. The net effect of increasing size is estimated to allow extrapolation of the current results to the full scale case.

Jet and drop breakup were studied individually using photographic, image processing and glass slide collection techniques in three facilities. A vertical wind tunnel was used for studies of individual drop and laminar jet breakup. Engine fuel nozzle atomization performance was measured using a nozzle spray facility centered around a turbine aircraft engine (JT8-D) fuel nozzle. Observations were made of the jet disintegration without ignition in the mini wing shear facility.

As part of these investigations an image processing data path has been established including pulsed ruby laser sheet illumination of sprays, high resolution photographic film recording, microdensitometer image digitization of 4 micron resolution, magnetic tape storage and processing with the JPL IBM 370/158 computer. Algorithms have also been developed incorporating low pass filtering and automatic intensity thresholding which are capable of measuring drop perimeter, area, and number density. Results of spray analyses using this new technique are reported. The need is described for development of more efficient algorithms for adequate characterization of sprays with large spatial variations of properties over distances several orders of magnitude larger than the average drop diameter.

Scaling studies of fuel atomization indicate that small scale experiments such as the mini wing shear yield only an upper bound to the atomizing behavior of a candidate fuel/additive system. Finer atomization of a larger proportion of ejected fuel is expected in a full scale aircraft crash. In

terms of reduced temperature, results of the mini wing shear tests and the Federal Aviation Administration (FAA)-developed Flammability Comparison Test Apparatus (FCTA) are found to be similar. As expected from the scaling arguments they are found to indicate greater fire suppression capability than that seen in larger scale facilities (i.e. the FAA full scale wing shear experiment).

At the highest air velocities and fuel mass flow rates, combustion efficiency increased with fuel/air ratio indicating that combustion is vapor limited (lean burning regime). Entrainment of ambient air which increases fuel vapor dilution and heat transfer are both augmented in the open jet models compared with the dynamics of an actual crash. This hinders prediction of actual crash flammability from open jet test results of any scale.

Radiometric calorimetry, while not as precise as thermocouple measurement, does allow resolution of a fire suppression performance pass/fail boundary. These results are, however, particularly sensitive to the presence of radiating surfaces.

Drop size measurements indicate a general correlation of decreasing drop size with increasing combustion efficiency. In general, drop size information must be coupled with spray density data to fully characterize mist flammability within a given flowfield. These additional data may also be extracted from photographic images using digital processing techniques.

A sensitive measure of polymer degradation level has been suggested. It is based upon the effective viscosity of the liquid during flow through a nozzle.

III. Introduction

Because turbojet engine fuel is difficult to ignite without first being atomized, it is possible to suppress post-crash fires by engineering a fuel resistant to atomization. Investigations of the atomization and flammability of an antimisting fuel have been undertaken and the results of one year's efforts are reported here. The fluid dynamic processes leading to atomization and the combined fluid mechanics, thermodynamics, chemical kinetics, and heat transfer problems posed by analysis of fuel spray combustion may only be treated comprehensively for the most elementary atomization/combustion situations. In contrast, the dynamics of an actual airplane crash with fuel spillage, atomization by pressure and airblast mechanisms, and ignition of fuel by various heat sources is richly complex. Every aircraft crash is unique with respect to such parameters as fuel, air and runway temperature, aircraft crash velocity and local windspeed, fuel tank rupture geometry, fuel dump rates, and existence of potential ignition sources. Compared to the laboratory environment, significant scales are very large in a crash. Ruptures of several meters diameter with dump rates of hundreds of kilograms of fuel per second have occurred. Airspeeds must be considered up to the maximum impact survivable crash speed, approximately 85 m s^{-1} .

Given the large number of possible events and the wide range of parameters which may exist, adoption of a fuel for crash fire safety must be preceded by a program of testing and analysis to determine fuel performance both during the crash and in operation as a turbojet engine fuel. The significance of variables describing the crash environment needs to be examined experimentally to determine individual effects on ignition and flame propagation. Modeling and scaling of the crash dynamics must be accomplished to allow development of a laboratory scale experimental apparatus which yields results

readily related to actual crash situations.

A steady state model of fuel ejection, atomization and ignition during an aircraft crash has been employed to study the effects of fuel flow rate, jet Reynolds number, temperature, pre-shearing and antimisting polymer concentration, as well as airspeed on the fuel flammability. Primary measurement of flammability has been with thermocouple temperature sensing downstream of the ignition source. Temperature variations with axial location are mapped as a means of discerning cases of polymer success and failure to suppress significant fuel ignition. Calorimeter and pyrometer measurements are also made to gain additional information on the flame temperature. Scale effects are treated through comparison of results from these tests with those from larger and smaller scale tests already in use.

Because the fuel drop size distribution and density are key factors in fuel mist ignition, a new tool has been developed to measure these quantities. This tool is based on digital image processing techniques originally developed at JPL in support of lunar and planetary exploration. Significant progress is reported in the development of this technique and preliminary results are reported in support of flammability data.

Digital image processing of moving sprays involves selection of suitable illumination and imaging arrangements. These have been assembled during the course of the work. Imaging and analysis of drops as small as 10 μm diameter in an overall spray several centimeters in extent with large spatial variations in drop size population places severe requirements on imaging and analysis techniques. Preliminary image enhancement and drop resolution algorithms including stretching, thresholding, gradient edge detection and spatial filtering have been investigated and implemented.

To determine whether antimisting fuel will perform properly as a turbojet

engine fuel, image processing techniques are also applied to analysis of engine fuel nozzle sprays. The effect of the polymer additive on spray cone angle and drop size distribution has been quantified using both this and the more classical techniques of direct measurement from film images and drop collection on coated glass slides.

IV. FACILITIES AND INSTRUMENTATION

4.1 Facilities

Two small scale versions of the FAA wing shear facility, described by Salmon⁵ were used to study the atomization and flammability of the modified fuel. A laboratory scale spray Flammability Comparison Test Apparatus (hereafter referred to as the FCTA) was supplied to us by the FAA/Technical Center and was used to study the effect of scale on flammability and for quality control testing. A fuel nozzle from a Pratt & Whitney JT8-D engine was used to study the polymer degradation necessary to produce a combustible spray.

4.1.1 Wing Shear Facilities

A wing shear apparatus provides a steady state simulation of a fuel spill during an airplane crash. The fuel spill is simulated by a stream of fuel ejected from the leading edge of a small airfoil that impinges against an airstream produced by an open jet wind tunnel. The heat sources present in an airplane crash are simulated by an oxyacetylene torch.

The wing shear apparatus is shown in figure 1. The blower is powered by a 50 hp motor and has outlet dimensions of 38.1 cm by 31.4 cm. The flow passes through a stilling section, a contraction section, and a 17.8 cm square test section with viewing ports of heat treated glass. The stilling and test sections are designed to control the freestream turbulence. This capability will be useful for later studies of flame propagation and heat transfer from various ignition sources. For the purposes of the present study, the apparatus was operated without damping screens or turbulence-generating grids. The maximum airspeed was 105 m/sec.

Orifices of various sizes were used in order to vary the fuel shearing rate independently of the massflow. High shearing rates were provided by four different orifices located in the leading edge of a symmetrical airfoil with a

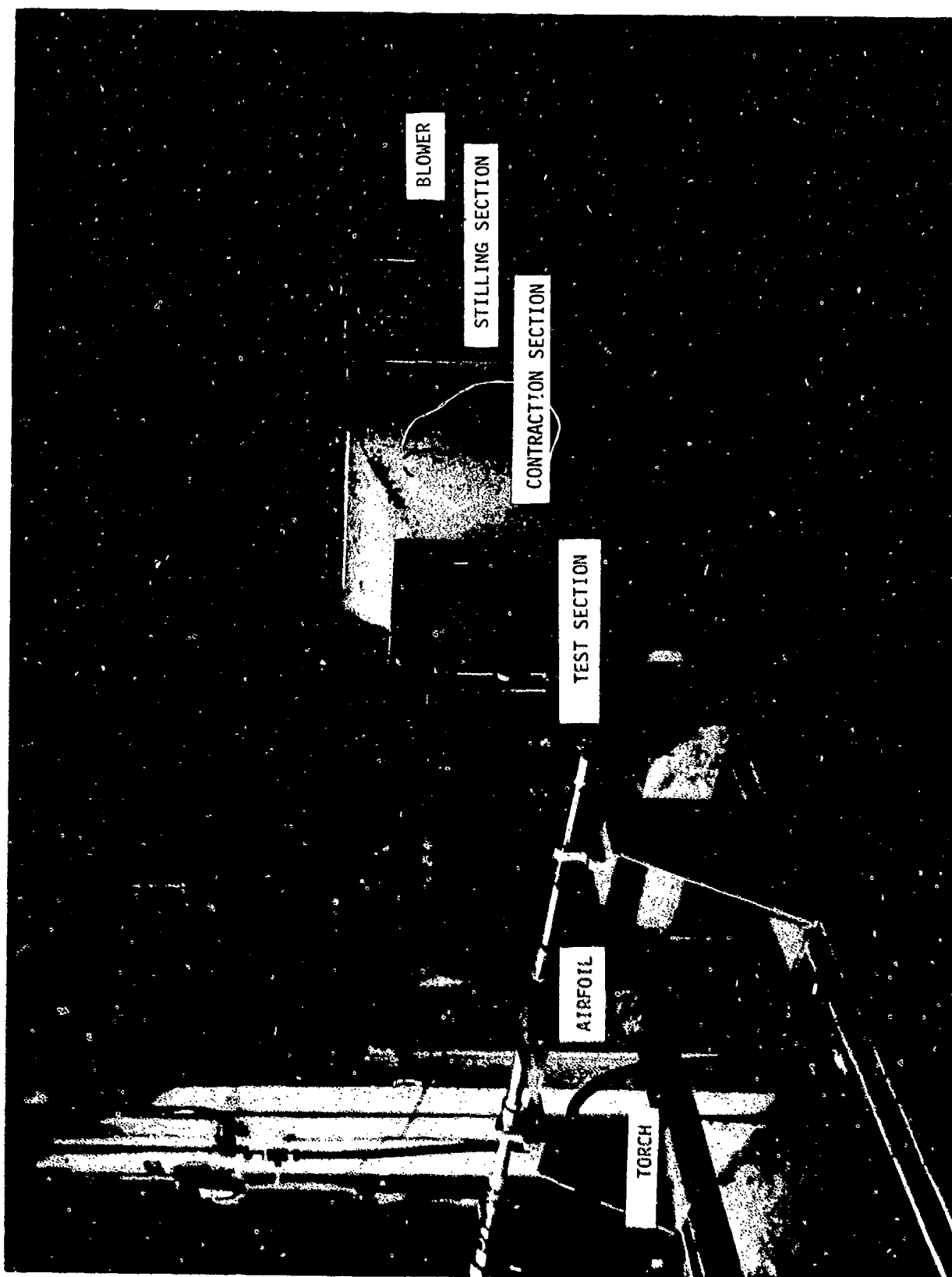


Figure 1 - Small-scale wing shear facility.

2.5 cm thickness and a 10.4 cm chord. Three of these orifices were circular and had diameters of 0.25 cm, 0.34 cm, and 0.79 cm. The fourth orifice was 0.5 cm square. High mass flow rates (up to 0.9 Kg/s) were provided by using a 1 inch pipe elbow with a 2.2 cm inside diameter in place of the wing (see figure 97). The elbow was the same size as the fuel lines and was used for most of the wing shear measurements reported here. Fuel flow rates were controlled by pressurization of the fuel tank.

4.1.2 Flammability Comparison Test Apparatus (FCTA)

The FCTA, shown schematically in figure 2, is described in detail by Eklund and Neese¹ and by Ferrara². Briefly, air is released from a pressure vessel through a sonic orifice into a straight tube, where it atomizes a small jet of fuel. The spray issues through a conical diffuser into ambient air and is ignited by a butane torch. The fuel is delivered by a single stroke displacement pump, and issues through an upstream facing elbow with an inside diameter of 0.52 cm. The inside diameter of the straight mixing tube is 2.66 cm. The air massflow is controlled by varying the air pressure and the fuel massflow is controlled by a constant speed actuator that regulates the fuel pump. Once the air pressure and speed control are set by the operator, the operation of the apparatus is controlled by an automatic sequencing switch.

The airspeed vs. tank pressure calibration is plotted in figure 3. Airspeeds were measured with a pitot tube, and they exhibit good agreement with hot film measurements reported by Eklund and Neese¹. The speed control calibration is shown in figure 4. Fuel massflow was measured by collecting and weighing the fuel.

4.1.3. Nozzle Spray Facility

Observations of fuel atomization by an aircraft engine nozzle were

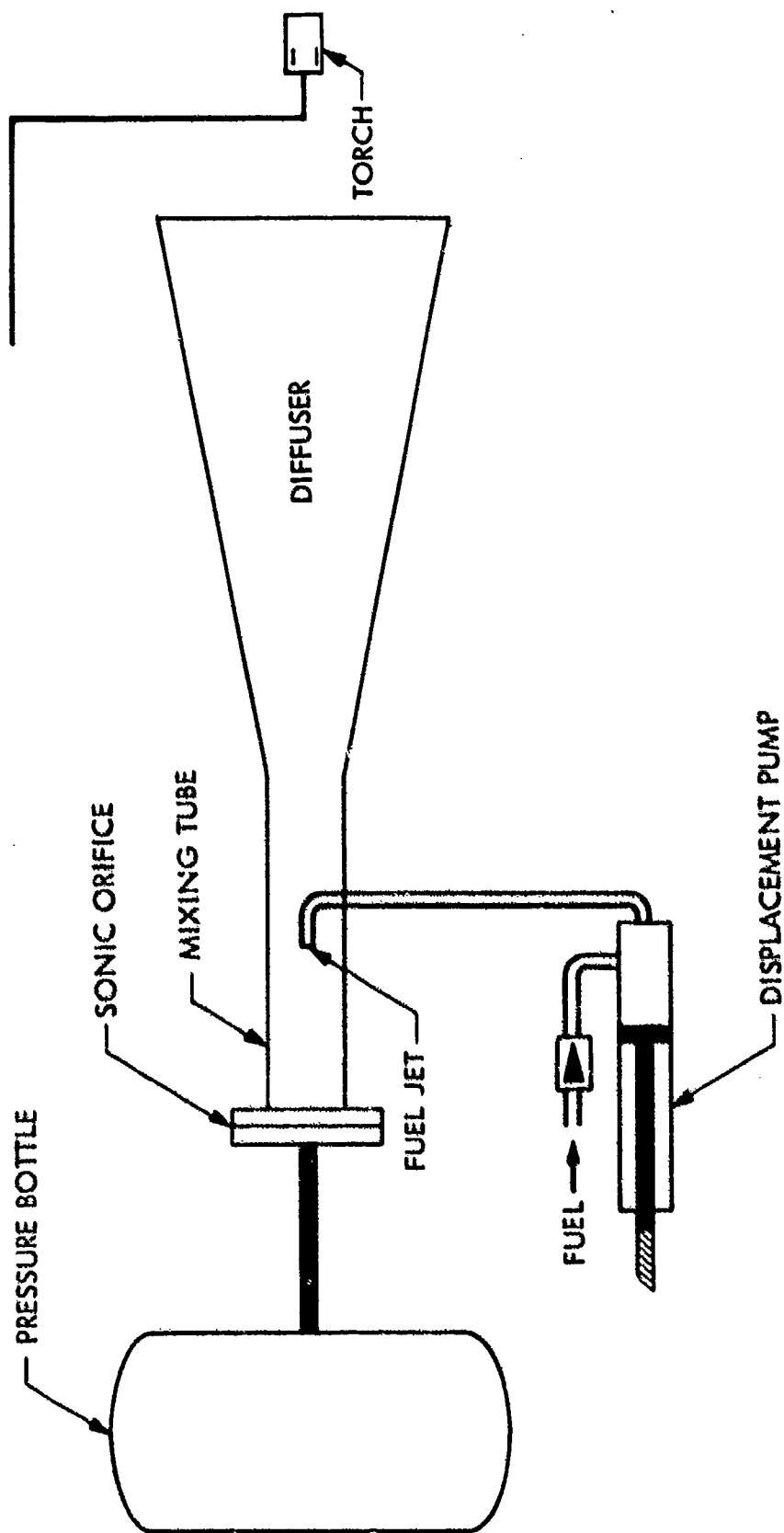


Figure 2 - Schematic diagram of the flammability comparison test apparatus (FCTA)

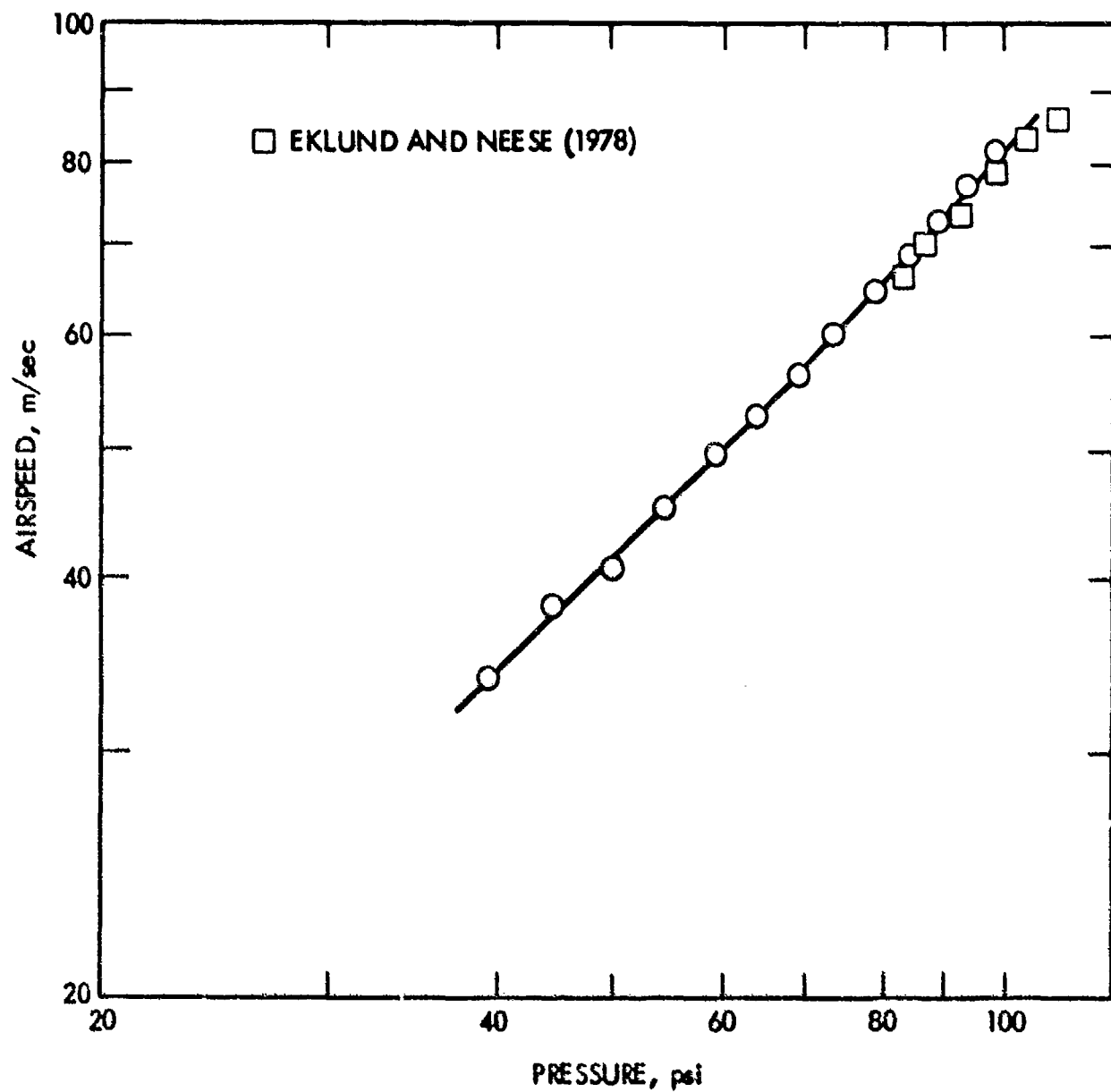


Figure 3. Calibration Results for the FCTA Supplied by the FAA: airspeed vs. supply pressure.

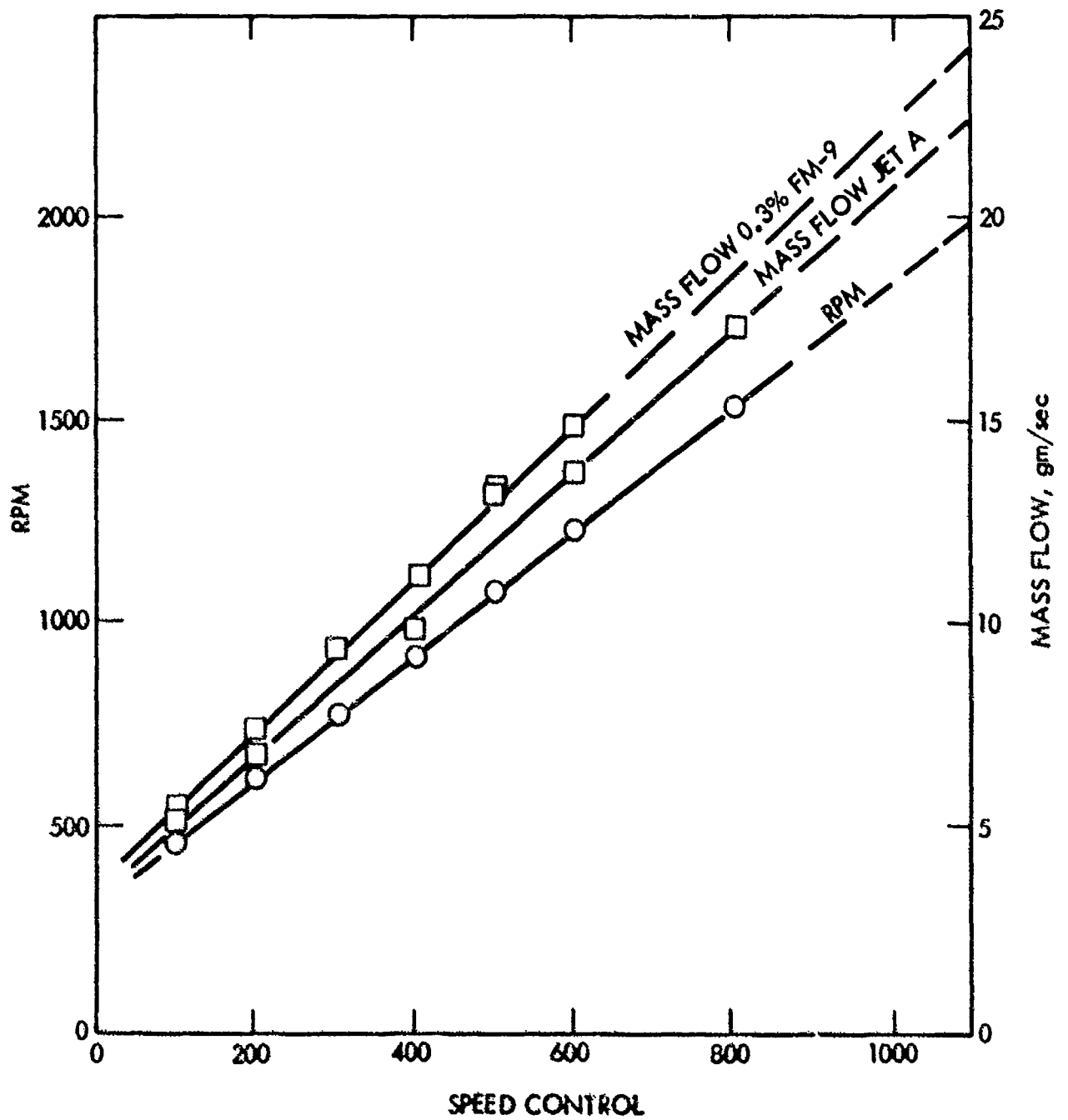


Figure 4. Calibration Results for the FCTA Supplied by the FAA: fuel mass flow vs. speed control setting.

carried out using the Nozzle Spray Facility. Figure 5 shows the facility. A Pratt and Whitney JT8-D engine fuel nozzle, 1, is mounted onto a polymethylmethacrylate (plexiglas) housing, 2. The housing is an open-ended box which provides protection from stray fuel droplets during observation and shields the spray from the influence of local air motion. The housing dimensions were chosen to allow observation with a line of sight normal to the spray centerline up to 40 cm downstream of the nozzle. No spray capturing devices were employed as part of the housing. Droplet recirculation is minimized by allowing the spray to exhaust into the combustion test area which is provided with coflowing ventilating air, and floor drains and separators for waste collection. For improved viewing the housing is fitted with an optical grade glass window, 3.

The Pratt and Whitney Bill-of-Material nozzle is a duplex type that is provided with two separate fuel supply systems. Fuel is pressurized by high pressure nitrogen from 135 atm tanks, 4, 5. Pressure regulators, 6, 7, maintain the chosen nitrogen pressure applied to the fuel reservoirs, 8, 9, which are 160 atm stainless steel tanks of 111 capacity. Before reaching the nozzle, the fuel passes through solenoid-controlled pneumatic valves, 10, 11, which are operated either by locally mounted, 12, or remotely mounted switches. The remote switches are situated in an adjoining room for safety when pulsed laser illumination is being used. Pneumatic actuator pressure is supplied from another 135 atm tank, 13, and regulator, 14. Air supply for the nozzle nut is provided by another 135 atm nitrogen tank, 15, and regulator, 16. The use of nitrogen instead of air was felt to enhance the safety of the test with no effect on nozzle performance. The nitrogen for the nozzle nut is supplied to a canister, 17, which surrounds the rear of the nozzle. The entire apparatus is mounted on a frame, 19, constructed of steel angles with

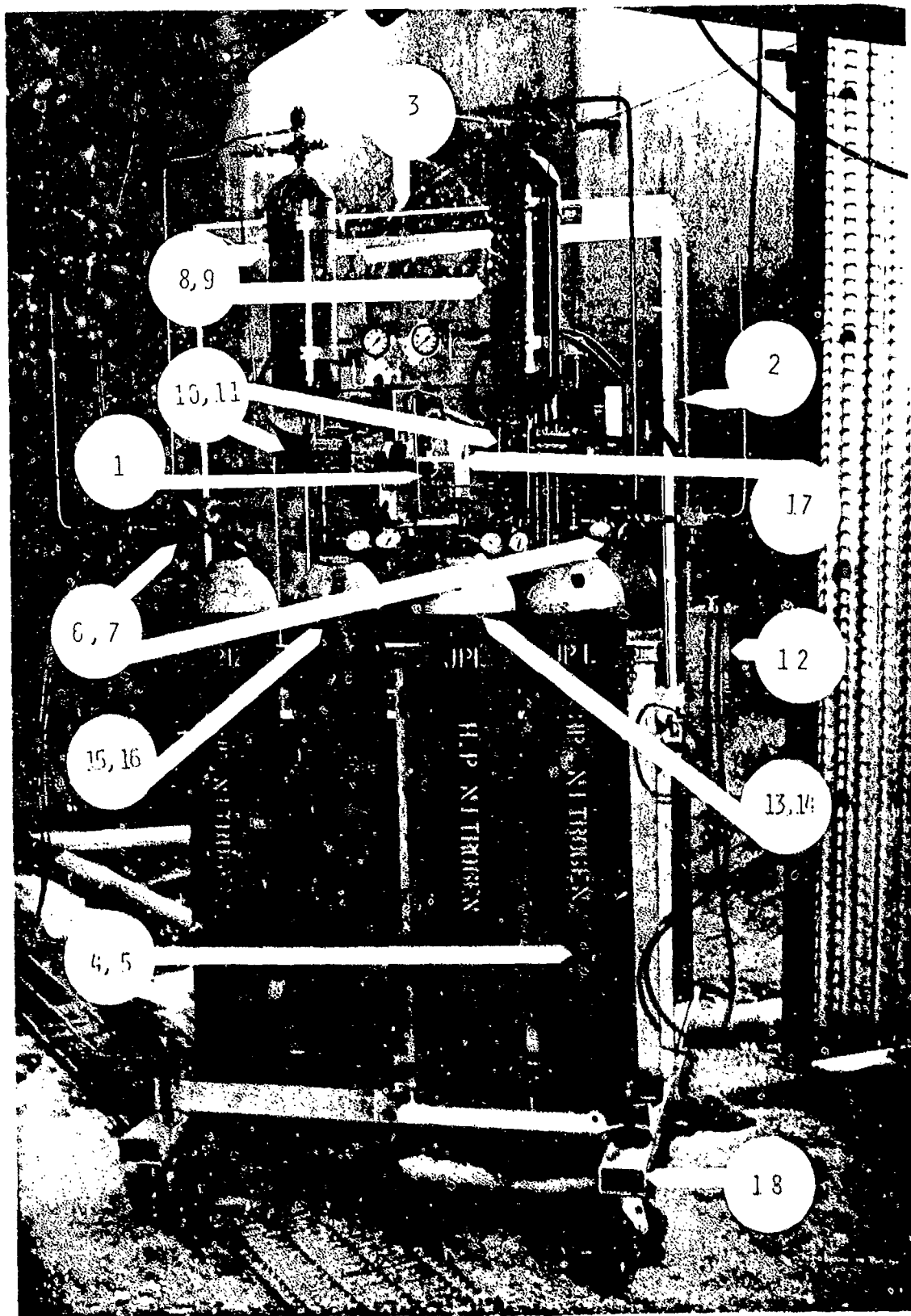


Figure 5 - Nozzle Spray facility for fuel atomization measurement (view facing forward).

rubber wheels so that it may be moved into the combustion test facility during operation. Figure 6 shows the nozzle spray apparatus in place for operation.

4.2 Instrumentation

Blower airspeed was measured with a pitot tube and fuel flowrates were measured with calibrated turbine flowmeters. Flammability was measured with chromel vs. alumel thermocouples, a radiometer, and a calorimeter.

Data acquisition during the wing shear flammability tests was automated. Voltages from the thermocouples, pitot tube system, and flowmeter were digitized, low pass filtered, and converted to physical units.

When partial degradation of the polymer was required, the modified fuel was processed either in an industrial food blender (Waring commercial 1 gallon) or an ultrasonic laboratory system (Ultrasonics Ltd. Rapidis 300). The degree of degradation was measured by the standard ICI cup test and the standard filter test, which are both described by Yavrouian⁴.

The turbine flowmeters consist of a turbine whose angular frequency is a function of volume flow rate and viscosity. A magnetic pick-off senses the spin rate of the rotor. If the working liquid is Newtonian, there is a range of rotational frequencies that vary linearly with volume flowrate and are independent of the liquid viscosity. In the case of the modified fuel, however, the flowmeter must be calibrated for each specific polymer concentration. Figure 7 is a family of calibrations for a 1/2-inch and a 1-inch flowmeter, and for FM-9 polymer concentrations of 0.20%, 0.25% and 0.30% by weight. The quantity K is defined by the expression:

$$K = \frac{f}{M} \quad (4.2.1)$$

where f is the turbine frequency and M is the massflow of the modified fuel. Over the linear range of operations K is constant. The tanh profiles are

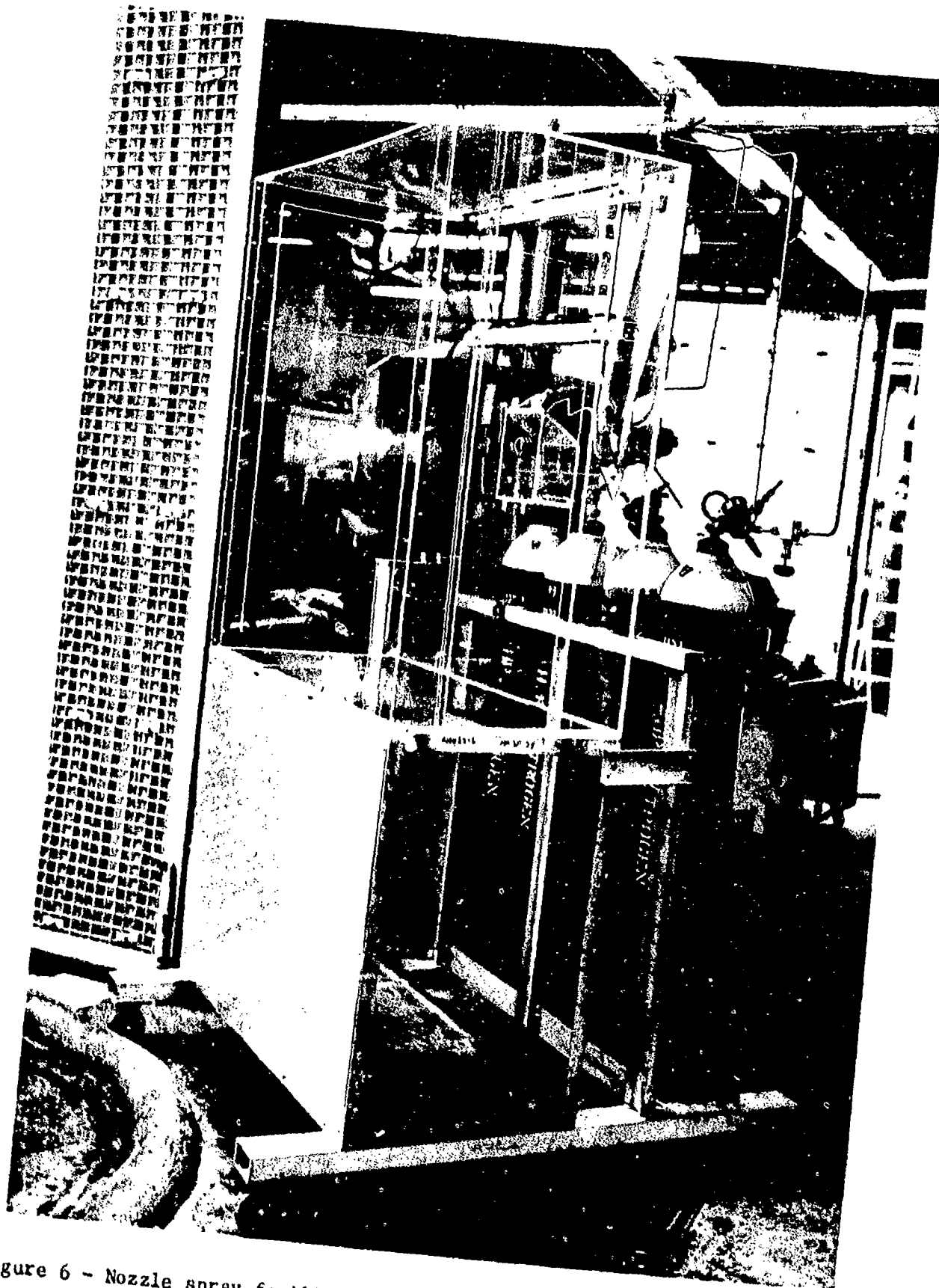


Figure 6 - Nozzle spray facility for fuel atomization measurement (side view)

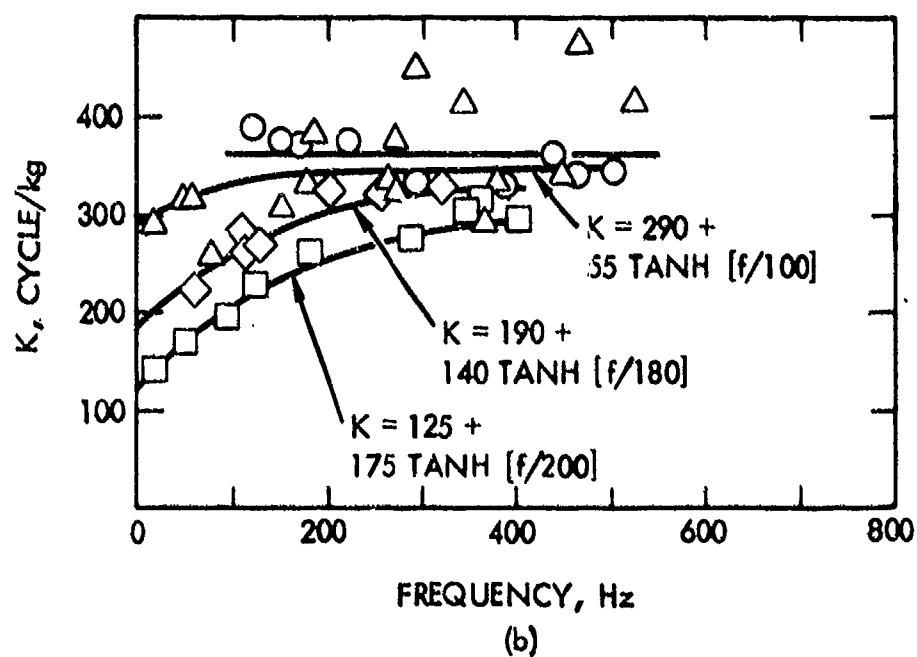
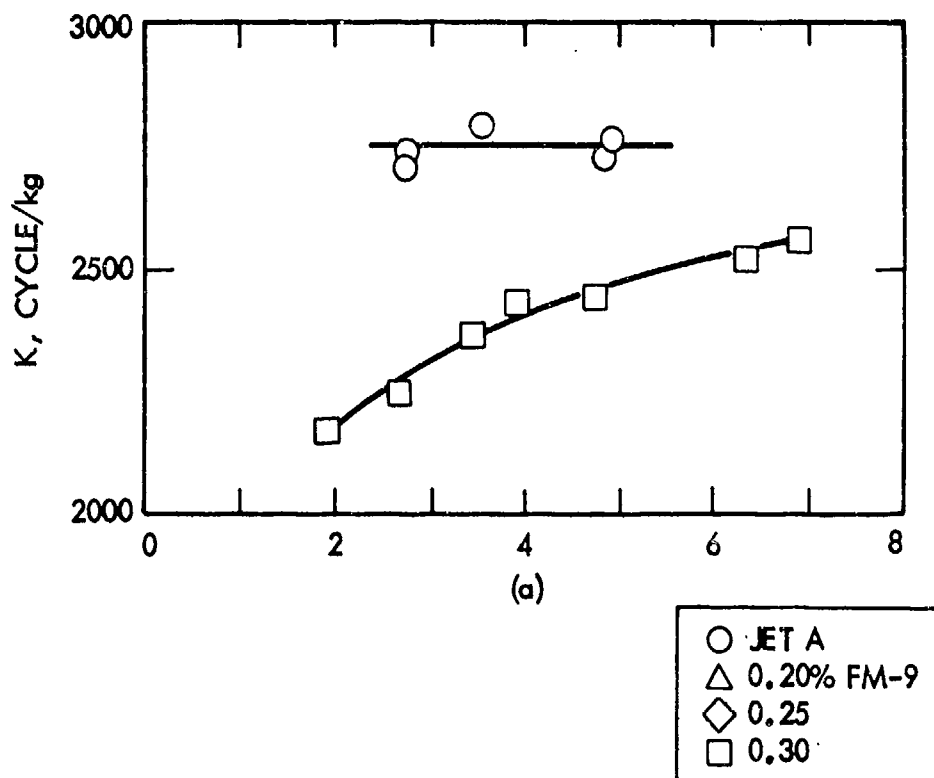


Figure 7. Turbine flowmeter calibrations for modified fuel: (a) 1/2 inch gauge; (b) 1 inch gauge.

convenient functional forms that seem to fit the calibration data, but they have no other physical significance. For some reason the repeatability of the 0.20% FM-9 calibration was poor and so there is large scatter in the data at that concentration.

4.2.1 Flammability Measurement

The emphasis of the flammability measurements in the past has been to determine whether or not the modified fuel provides fire protection under a given set of circumstances. Because there is usually some combustion taking place, this amounts to establishing a "pass/fail" criterion for the maximum amount of combustion that can be tolerated. The criterion is subjective and is often related to whether fuel adhering to physical boundaries such as (wetted) walls and ground catches fire. Because the present study is concerned with identifying scaling parameters, reliable quantitative measurements are necessary. The most popular tools for measuring flammability have been photography, radiometers and temperature probes.

Photography was used by Salmon⁵ to determine pass/fail in connection with the wing shear facility at the FAA Technical Center. Because the combustion is unsteady, the growth of a single fireball can be measured by following it through successive frames of a high speed cinema. Salmon found that fireball growth rates greater than 6 m/sec, were considered to be in the "fail" region. Photography has the great advantage of being a remote measurement. It is probably the only suitable technique for measuring flammability during a crash test, for example. The main disadvantage of frame-by-frame analysis is that it is time consuming, even if it is done with a video digitizing system. Also, the fireball growth is artificially limited by the boundaries of the air jet mixing region. It should probably not be considered related to the flame propagation speed but rather a measure related to the amount of fuel burned.

Radiometers measure thermal radiation. Two types of radiometers potentially useful to flammability studies are infrared imaging systems and radiometric calorimeters. The imaging systems frame a small area of the flame and a radiometer then measures the equivalent black body temperature of that area. By scanning the flame, it is possible to measure temperature distributions. Radiometric calorimeters measure the radiant heat flux onto an isothermal surface of known emissivity. Unlike the infrared imaging systems, calorimeters are omnidirectional and the measured heat flux decreases with increasing distance from the source. In principle the total radiation could be measured by integrating the output voltages from an array of calorimeters located in the thermal far field of the flame. Radiometry, like photography, has the advantage of being a remote measuring technique, albeit without the spatial information available in a photograph. The main disadvantage of radiometers is that they are sensitive only to radiation. Because the emission spectra from gases are discrete, the effective emissivity is a function of both temperature and local gas composition. For this reason black body temperatures measured by the imaging systems are unreliable except as figures of merit. Radiometric calorimeters, since they measure the heating of a calibrated surface, are more quantitative. However, their usefulness is generally confined to cases where there is considerable combustion. In any case, the emissivity of solid surfaces is much higher than that of gases. Consequently, radiometers are sensitive to radiation from walls and surfaces.

Temperature probes provide a relatively continuous combustion measurement. If there is no liquid phase present they measure local gas temperatures. If there is significant wetting of the probe, vaporative cooling will lower the probe temperature. Even in that case temperature probes can provide a reasonably sensitive figure of merit. For these reasons they are useful in

cases where the amount of combustion is small. The main disadvantage of temperature probes is that they provide local measurements. This means that probe arrays must be used in order to obtain spatial information. Also, at very high temperatures, radiation losses introduce errors.

Because temperature seems to be the most direct measurement of combustion extent, temperature probes were used for the primary flammability measurements. The other techniques have important advantages, and some may prove most useful in the long run. Consequently, a secondary goal of the investigation has been to relate the various techniques. The temperature probes used are chromel-alumel thermocouples, with exposed junctions 0.76 mm in diameter. The time constant is 1.7 sec at an airspeed of 20 m/s. The convective heat transfer to the junction considered as a sphere is described by King's Law of Cooling:

$$\frac{\dot{Q}}{\lambda d (T - T_p)} = A + B [Pr^{1/3} R^{1/2}] \quad (4.2-2)$$

Where \dot{Q} = heat flux into junction;

λ = thermal conductivity of air (= 0.024 W/m K);

T = local temperature;

T_p = volume average temperature of probe junction;

d = diameter of the probe junction (= 0.76 mm).

Pr = Prandtl number of air (= 0.71)

R = Ud/ν = Reynolds number

U = local airspeed

ν = kinematic viscosity of air (= 0.15 cm²/s)

A, B = empirical constants

(For purposes of this calculation, the properties of the mixture of air, fuel and combustion products have been identified with those of air).

The heat flux into the junction is (ignoring conduction to the leads):

$$\dot{Q} = mc \dot{T}_p \quad (4.2.3)$$

where:

m = mass of probe junction (=0.0020 g)

c = specific heat of junction (=0.486 J/g)

For large Reynolds number, the probe response is described by combining eqns. (4.2-4) and (4.2-3):

$$\dot{T}_p + K U T_p = K U T$$

$$\text{where } K = \frac{B \lambda d^{3/2} \rho_r^{1/5}}{mc v^{1/2}} = 0.119 B(\text{ms})^{1/2} \quad (4.2.4)$$

The probe response is calculated by solving eqn. (4.2-4) for a step change in temperature. Thus:

$$T_p = T [1 - e^{-K U}] \quad (4.2-5)$$

At $U = 100$ m/s, the time constant, $\tau = 0.76$ sec. The time constant depends on $d^{3/2}$, so the response can be improved by reducing the size of the probe. The smallest practical junction diameter is about 0.03 mm. At $U = 60$ m/s the time constant would be 8 ms. The smallest scale that could be resolved would be about 50cm. Consequently, the only practical combustion measurements possible with these probes are time average temperatures.

For evaluation purposes, some radiometer measurements were taken simultaneously with the temperature measurements. An infrared imaging system and a calorimeter were each evaluated. The imaging system used a Casagrainian lens to focus an element of surface area onto a heat sensor. Signal to noise was enhanced by chopping the optical path and using synchronous detection. The radiometer was located 3.5 m laterally from the blower centerline, and the field of view at that distance was approximately 3 cm wide (angle of view was 0.5°). The calorimeter measured the heat flux through a surface of known

emissivity. The heating was measured with a water cooled, sensitive thermopile. The active surface was 2.54 cm in diameter, the response was approximately 250 ms and the range was 57 kw/m².

V. IMAGING AND IMAGE PROCESSING

5.1 Introduction

In both post-crash fire protection and engine fuel combustion applications, the ability of antimisting kerosene to suppress formation of small droplets is the basis for its performance differences from neat jet fuel. Drop sizes and their distribution are key factors in the determination of fuel spray combustion performance⁶. For this reason, a detailed investigation of the atomization performance of these fuels has found an important role in this study.

5.1.1 Methods of Drop Size Measurement.

Over the past 50 years, a large variety of experimental techniques has been devised to measure drop sizes in liquid sprays. These methods are summarized in comprehensive review papers of B.J. Azzopardi⁷, A.R. Jones⁸, .. C.G. McCreath and J.M. Beer⁹, and A. Burkholz¹⁰, the last of which treats mechanical sizing methods in a more up to date manner. The large number of techniques described in the literature may be organized by their general approach, each of which carries with it certain advantages and drawbacks. Technique development specific to a particular spray geometry or application has resulted in the proliferation of measurements techniques. Following Azzopardi⁷ the methods may be grouped as: Photographic; Impact; Thermal; Electrical; Optical; Time of Residence; and "Indirect via Velocity". More recent work of Skifstad¹¹ would add another category, blending aspects of Photographic and Optical approaches.

To choose an existing method or to design a new one, the specific needs of this analysis were addressed. Because of the non-Newtonian nature of AMK and the irregular breakup which may result when fuel is ejected from moving aircraft into stagnant air during a crash, no drop size distribution function

could be chosen a priori. Thus accurate measurement of drop population over the size range of 10 to 1000 μm , the size range most significant to spray combustion behavior¹², was desired. This requirement eliminates most time of residence methods such as laser anemometry which operates most successfully on larger droplets ($> 100 \mu\text{m}$).

Optical methods were eliminated for a variety of reasons despite their wide acceptance in the field of fuel nozzle development. Scattering behavior occurs in different modes as droplet size changes relative to the scattered beam wavelength. This limits the dynamic range obtained by many of the methods. As the polymer additive may affect fuel optical qualities such as index of refraction and opacity, additional data and perhaps more sophisticated scattering data not currently available would have been necessary to incorporate scattering and obscuration methods. The cloudiness sometimes apparent in AMK may sharply influence scattering measurements. Because earlier experience with polymer fuel additives indicated the atomized drops were slow to relax to a spherical shape¹³, methods which assume spherical droplets, as many scattering techniques do, were considered inadequate.

Frozen wax methods are unsuitable because of the need to investigate specific liquids whereas these methods investigate the breakup of a substitute material (melted wax) which would not have similar rheological properties.

Impact methods suffer from large uncertainties in relating impact impression and actual droplet sizes^{14, 15, 16}. Also, when adjusted to operate at mean mass fluxes, an encounter with a large fluid mass typical of AMK sprays may ruin an entire slide. This method was employed at a secondary level in support of the major effort in droplet sizing. It is reported more fully in section 5.7.

In summary the unique requirements of a spray analysis system capable of

operating with sprays of wide fuel drop concentration, size, and shape variations of a locally time-varying nature, comprised of a fluid of unknown optical properties, render most existing techniques unsuitable. Photographic recording with suitable illumination could meet these requirements, but manual counting and sizing of thousands of droplets in photographic images is tedious and subject to operator-induced errors of up to 30%^{17,18,19,20}. Because of these problems, automated particle analyzers, notably the British Quantimet²¹ and the Parker-Hannifen²² systems, have appeared on the market. The principle of operation of these analyzers is described by Graf²³. They rely on simple pattern recognition algorithms to identify and measure droplets in an image of a spray. Because of their limited computing power they cannot eliminate out-of-focus drops nor can they interpret overlapping and non-spherical drops accurately. Absolute counted drop size is a function of picture brightness and operator preference.

5.1.2 Image Processing in Spray Measurements

The recent dramatic increase in ability to handle large amounts of data has permitted the development of digital image processing as contrasted to the simpler counting schemes characteristic of Quantimet. Digital image processing may be defined as the representation of images as large arrays of discrete data values and the manipulation of these arrays according to specific algorithms. The impact of this development is that much more of the vast quantity of information available in an image may be used for the quantitative analysis of the image content (image analysis). Also, information either present in the images or known about the conditions present during the original imaging may be used to reduce imperfections such as blurring, excesses or deficits in contrast, uneven subject lighting and foreign object interference (image enhancement).

Image processing techniques have been developed at the Jet Propulsion Laboratory over the last 22 years mainly in support of unmanned lunar and planetary probes (see the discussion of this development given in the appendix of reference 24). Digital image processing techniques have also been applied at JPL to problems such as imaging of data from non-visible sources (ref. 24 p. 387), mapping of vorticity in planetary circulation ²⁵, automated computation of stellar magnitudes from astronomical images ²⁶, automated reconstruction of side-looking sonar-generated images ²⁷, geological analysis of aircraft scanner data ²⁸, and extraction of lost handwriting in historical documents ²⁹.

Through use of pre-existing algorithms developed for programs such as those mentioned above and new algorithms tailored to this application, image processing has been applied in this effort to the characterization of fuel sprays. The sprays analyzed are from various simulations of the aircraft crash fuel spill dynamics and from engine fuel nozzle performance observations (see Section 6.2). Both image enhancement and image analysis capabilities were exploited in this investigation. Enhancement was used to eliminate film grain, lighting variations and out-of-focus objects from recorded images. Automated analysis was employed to measure the perimeters and area of the large number of droplets (500-1000) ^{7,30} which must be counted in each subject spray to yield valid statistical results.

The system described in sections 5.2 through 5.6 is free of assumptions concerning droplet shape, velocity, refractive index, opacity and flow time invariance which seriously limit the confidence which should be placed in results of scattering methods. It does not rely on the inversion of signal conditioning integrals which may have broad areas of insensitivity and even singularities which may hamper many optical and optical/photographic tech-

niques. Capabilities have been developed to ensure maintenance of a large enough viewing field to adequately represent large drops (up to 2 mm diameter) with sufficient resolution to represent small drops to below 10 μ m diameter. No assumptions are made concerning drop size distributions and the ambiguity introduced in assessing drop size from impact impressions is absent. Finally, unlike other available automated imaging systems, absolute picture brightness level³¹ and illumination distribution effects do not disturb the measurements. The system represents a new application of image processing technology and an advance in the state of the art of fuel spray analysis.

5.2 System Overview

The initial investigation of the application of image processing techniques to jet fuel flammability studies began by using the facilities at JPL's Image Processing Laboratory (IPL). Several alternative data paths were conceived through which the stored image information of the fuel spray imaging experiments could be transferred to the IPL for digitization, processing, and hard copy image output (figs. 8, 9, 10). For the initial study, a methodology was selected which fulfilled the task objectives most efficiently, satisfied physical and material constraints, and provided the necessary environment for image processing technique development.

Fuel droplet illumination requires a light source that will freeze the high speed particles, enabling an imaging device to record an accurate picture of the in situ fuel droplet behavior. Accuracy and uniformity in the depth of field of illumination must be achieved in order to control the statistical relation between subscenes within both a single image and among a collection of images for varying experimental conditions. A pulsed ruby laser system serves as the illumination source which satisfies the imaging experiment requirements (see Section 5.2).

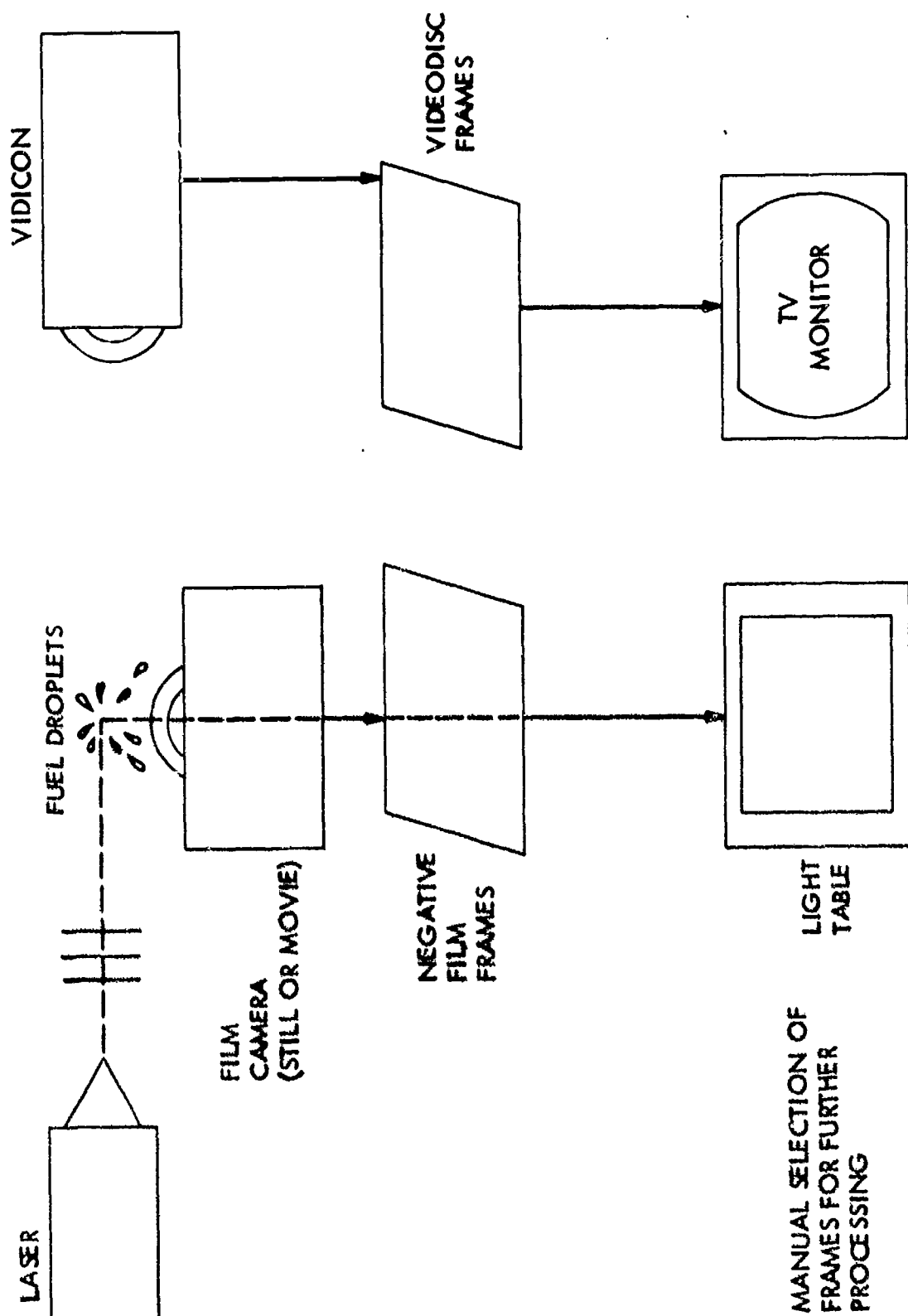


Figure 8. Imaging data paths; formation of initial images may be accomplished with photographic processing (left) or analogue electronic devices (right).

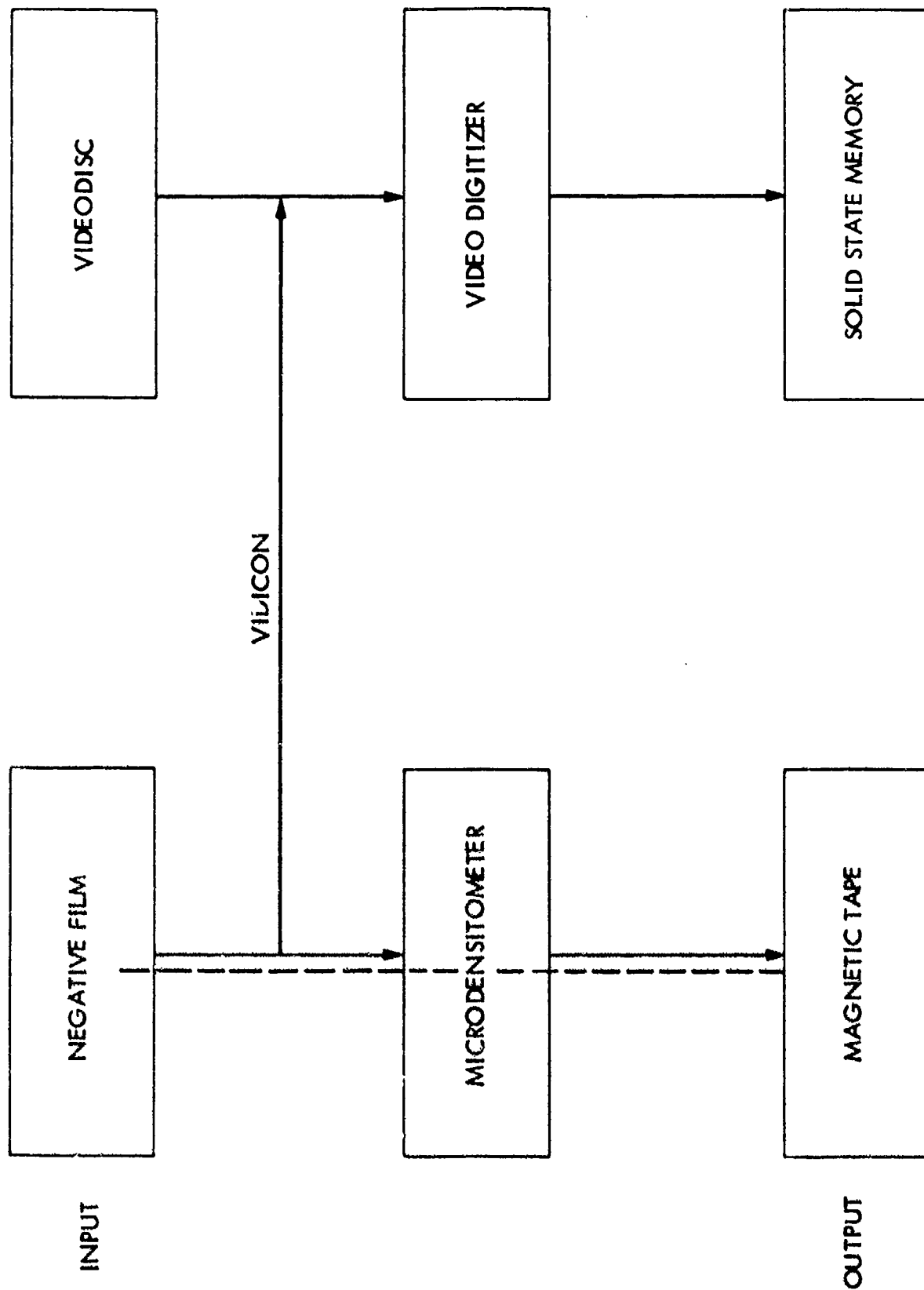


Figure 9. Image digitization paths; either a microdensitometer (left) or a video digitizer (right) is used.

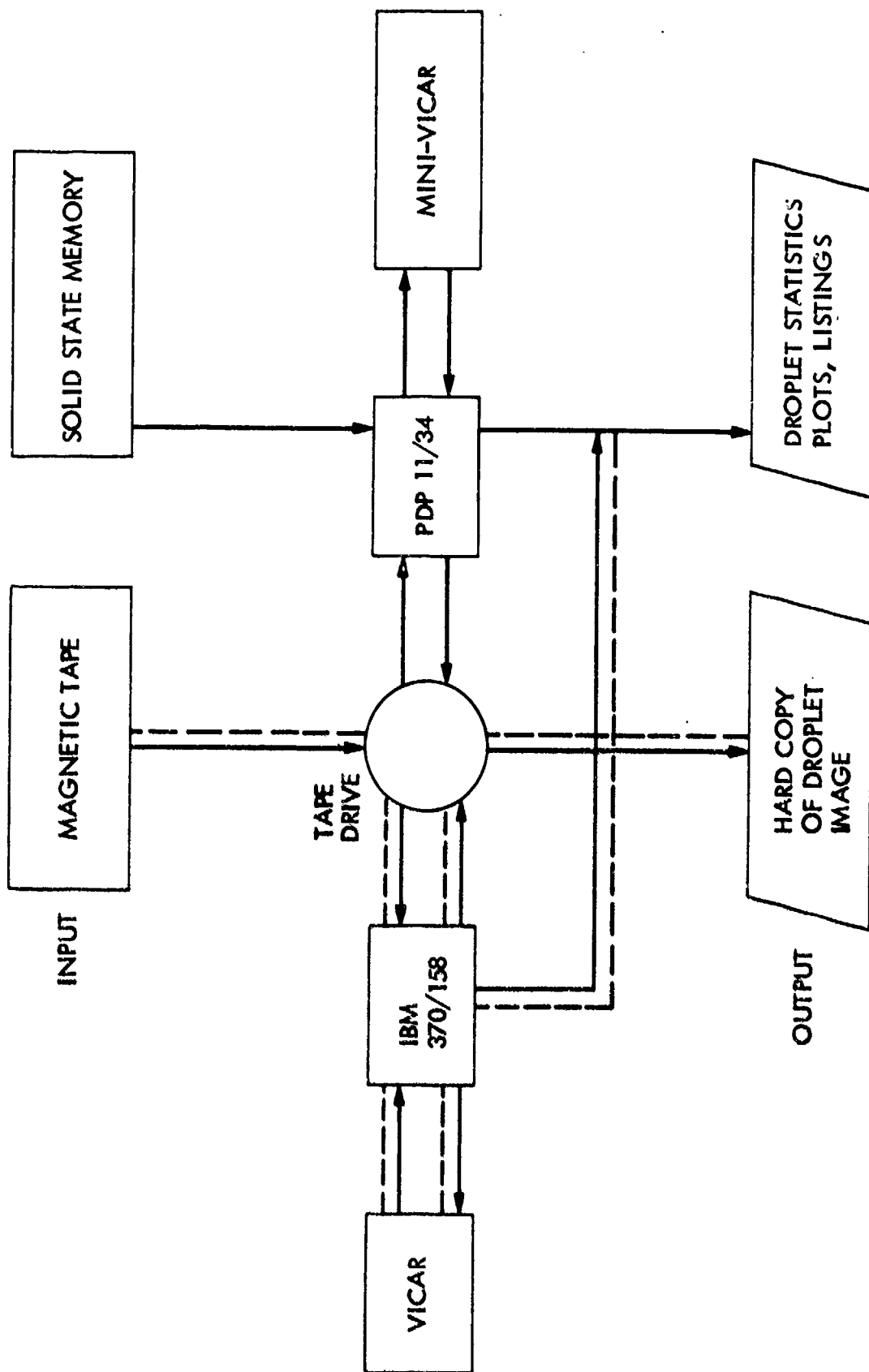


Figure 10. Image processing paths; IBM 370/158 or PDP 11/34 computers may be used with VICAR or Mini-VICAR software packages.

Recording the laser-illuminated fuel droplet scene allows two viable options as recording media: photographic film or video frames. A 4x5 inch film format provides a high resolution analog recording with a large field of view. At a 1:1 optical magnification, a microdensitometer digitization procedure can achieve a pixel (picture element) resolution as high as 3 microns. This combination of resolution and field of view allows the researcher to study fuel droplets with diameters below 10 microns and simultaneously gather global statistical information about the droplet size characteristics by simultaneously sampling a large physical area of the fuel mist. Vidicon imaging has as its foremost advantage a higher data throughput rate where direct digitization and image display of the digitized signal are accomplished at video rates. Field of view and resolution are limited by the 512 square element matrix of data sites available for the storage and digitization of each video signal frame. However, the data processing speed provides compensation by making it possible to record a large sampling of subscenes within the experiment and then combine particle statistics for both adjacent and separated droplet image sections. As a preliminary tool for the development of fuel droplet image processing techniques, the highest quality image possible was desired to investigate the maximum achievable resolution of the experiment and to examine a wide spectrum of image data. Furthermore, the images recorded at the experimental site had to be transportable to the IPL facility to provide access to a large library of image processing software necessary to accomplish the Phase I research. For these reasons a highly sensitive photographic film, Technical Pan, developed by Kodak and characterized by a submicron film grain, was used to record the fuel droplets.

The final stage in the development of images suitable for computer enhancement involves the digitization of the recorded fuel droplet data. In the

case of a video frame, a compatible video digitizer is the single method available for digitization. These analog video frames can be digitized to a 512 x 512 element array at a rate of 30 frames/sec. At this point, the digitized image is stored in solid state hardware memory and is readily accessible by the digitizer's host computer. A De Anza ID-5400 Image Display System was acquired to perform video digitizing and first order image processing of the AMK fuel data ³². The video signal digitizer can perform video rate digitizations of 512 x 512 frames with 8-bit accuracy, thus allowing up to 256 image pixel values. Film recordings of the fuel data can also be digitized by re-imaging the film negative via a vidicon and then digitizing the output video signal. Digitization noise resulting from the quality of the analog signal and sampling effects must be accounted for in the image processing scheme to minimize image artifacts that may interfere with the fuel droplet detection process. A second method of film digitization that succeeds in lowering the digitization noise is to scan the film negative with a microdensitometer. In extensive use at the IPL is a PD5 10 x 10 G Scanning Microdensitometer capable of digitizing film negatives at varying resolutions and optical configurations ³³. The microdensitometer scans the film in a raster format, recording the optical density of the film negative as measured by an electronic sensor. The viewing window used in determining each digital value and the spacing interval between each window are adjustable to the requirements and specifications of the particular application. For this study, the Technical Pan film negatives were digitized on the PDS microdensitometer and a set of digital images were created on magnetic tape for subsequent image processing technique development and testing.

Digitized fuel data in image format enables a computer to perform image processing operations to enhance and thus distinguish the fuel droplets from

extraneous information in the images. To perform the necessary image processing tasks for the fuel droplet imagery, a customized computer facility with interactive image processing capabilities and comprehensive image processing software was essential. The IPL facility at JPL provided all of the above and served as the primary site for the initial image processing research 34.

5.3 Illumination

Subject illumination is a critical consideration in the design of an imaging/image analysis system. Elimination of blurring due to subject motion becomes particularly critical as subject size decreases and velocity increases. The time, t , for a subject to traverse its diameter, d , is

$$t = \frac{d}{V}$$

where V is the subject velocity.

For sharp imaging only a small fraction (~ 20%) of the subject diameter may be displaced during an exposure. Given the system requirements to image $10\mu\text{m}$ droplets (Section 5.1) moving at up to 100 ms^{-1} (Section 4.1.1), the light source must be no longer than 20 ns in duration. The light energy which is to be provided during this short interval is a function of the size of the area to be illuminated, receptor optics and sensitivity, and the light reflecting/scattering capacity of the subject. Forward scattering schemes have been devised to take advantage of this relatively efficient scattering mode 10, 35. As shown in figure 11a, the forward scattered beam illuminates drops through the entire spray. The only means to examine individual drops in dense sprays without overwhelming drop image overlap problems is through imaging optics with a short depth of field yielding a limited focal volume. Because focus is used to choose the observation region, a determination must be made of which drops are in focus and which are not. This is extremely difficult in practice. Small droplets at the margins of the focal volume will not be resolved,

whereas large droplets at the same axial location will be. This skews the measurements obtained toward larger sizes.

Figure 11b shows the sheet illumination chosen for this investigation. Here the focal volume is not significant as the only droplets imaged must lie in the plane of the sheet. The sampled volume is well defined in this arrangement so that the fuel loading, which is the volume occupied by liquid fuel or a fraction of the total volume examined, may be measured along with drop sizes. Because of the relatively weak scattering at right angles to the light source, a bright light is required. For this application a one Joule pulsed ruby laser was chosen (Apollo Laser Systems). The laser is equipped with a Pockels cell to compress the radiated energy into a 20 ns pulse, meeting the duration requirement for sharp imaging. Referring to figure 12, the laser, which has an initial beam diameter of 20mm, is passed through a spherical lens of 1m focal length, which reduces the beam thickness to approximately 10mm as it tranverses the spray. The beam then passes through a cylindrical lens of 25 mm focal length. This spreads the beam about 1 axis, forming the flat sheet. Viewing along a line normal to this sheet, one can see a thin cross section of the spray.

5.4 Image Recording

As previously discussed (sec. 5.2) photographic film was chosen as the most compatible medium for initial data recording and subsequent digital analyses. Resolution of a statistically significant number of drops ranging in size from 10 to 2000 μm at widely separated regions of a spray places extreme requirements on optical and film resolution. Three avenues were taken toward meeting this requirement: design of the photographic system, film choice, and image mosaicking.

A 4 x 5 inch format view camera was employed so that the image size could

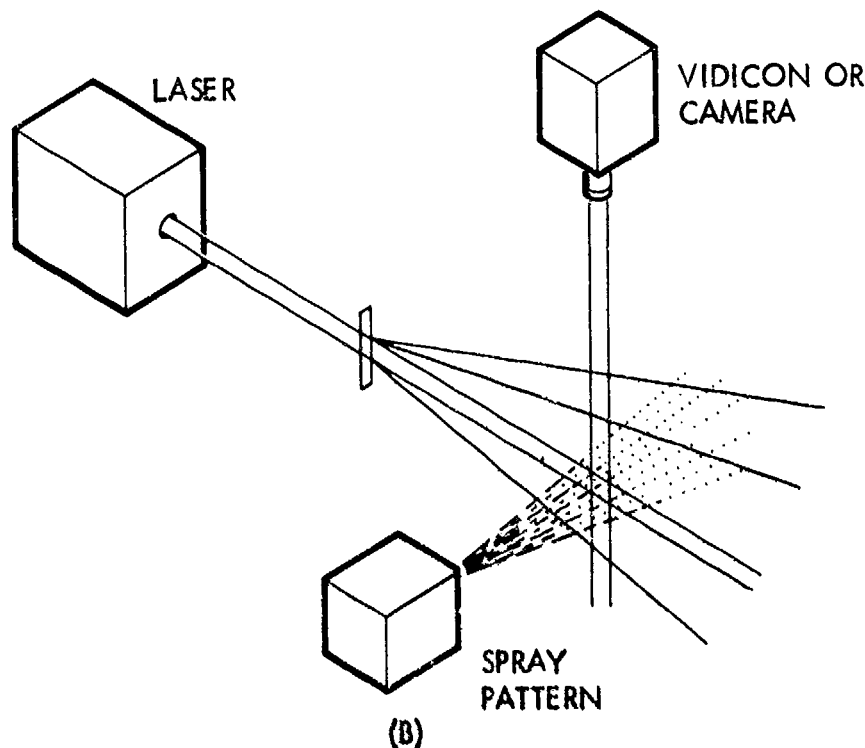
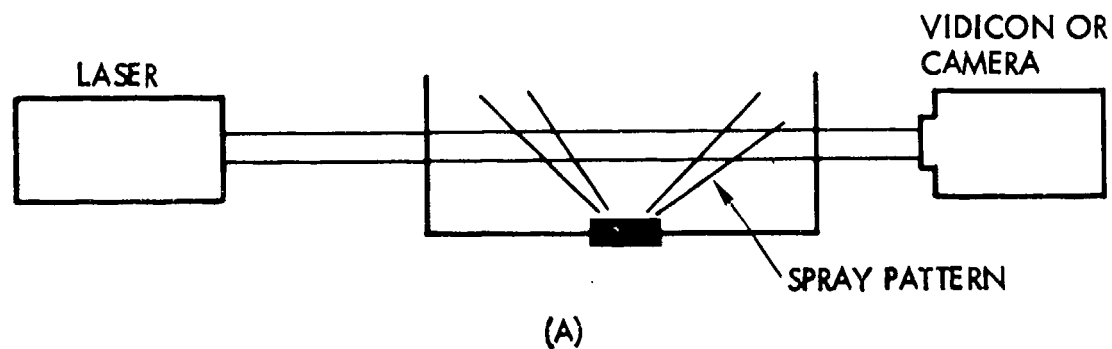


Figure 11. Laser illumination configurations (a) forward scatter; (b) sheet illumination.

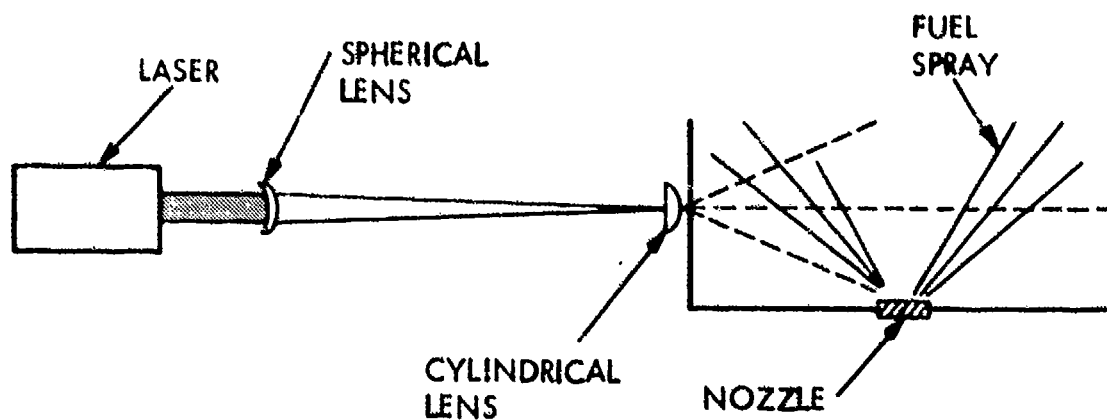


Figure 12. Optical configuration for laser sheet illumination.

be kept relatively large compared with the subject size. The camera was mounted, in the case of the nozzle spray observations, 75 cm above the focal plane so that it would not disturb the fuel spray. To maintain image size at this distance, a 380 mm focal length lens was used with an 86 cm extension. This configuration, shown in figure 13, yields images approximately equal in size to the subject.

Besides offering resolution of drop images at least as small as $10\text{ }\mu\text{m}$, film chosen for this application must be sufficiently sensitive to form an image with the light available via 90° scattering of the diffused laser. Use of these large lenses limits shutter/flash synchronization speed to 0.02 second, but imaging via ambient light must still be minimal to avoid blurring. Many orthographic and lithographic films were considered but found unsuitable because of their low sensitivity and extreme contrast. The digitization process can resolve 256 gray levels (8 bits of information) in each pixel. The availability of the large number of gray levels in the original recorded image may be crucial to the performance of processing algorithms. Often a brightness gradient is used to help identify particle edges, and resolution of only a small number of gray levels typical of high contrast emulsions would cause extreme variations in these derivatives. The requirements for high sensitivity and spatial resolution with moderate gray level resolution were met best by Kodak Technical Pan film (Ref. 5). Though rated at a daylight ASA of 125, its sensitivity is skewed toward the red causing it to perform at an effective ASA 6000 when used with ruby laser illumination. The specified resolution of the film is 330 lines per millimeter. Exposures were made through a Kodak #24 red filter at 0.02 second exposure with an aperture setting of f16. No trace of daylight illumination is detectable in the images. Processing was carried out by a Kodak Versamat processor operated at a film speed of 4.1 cm/s.

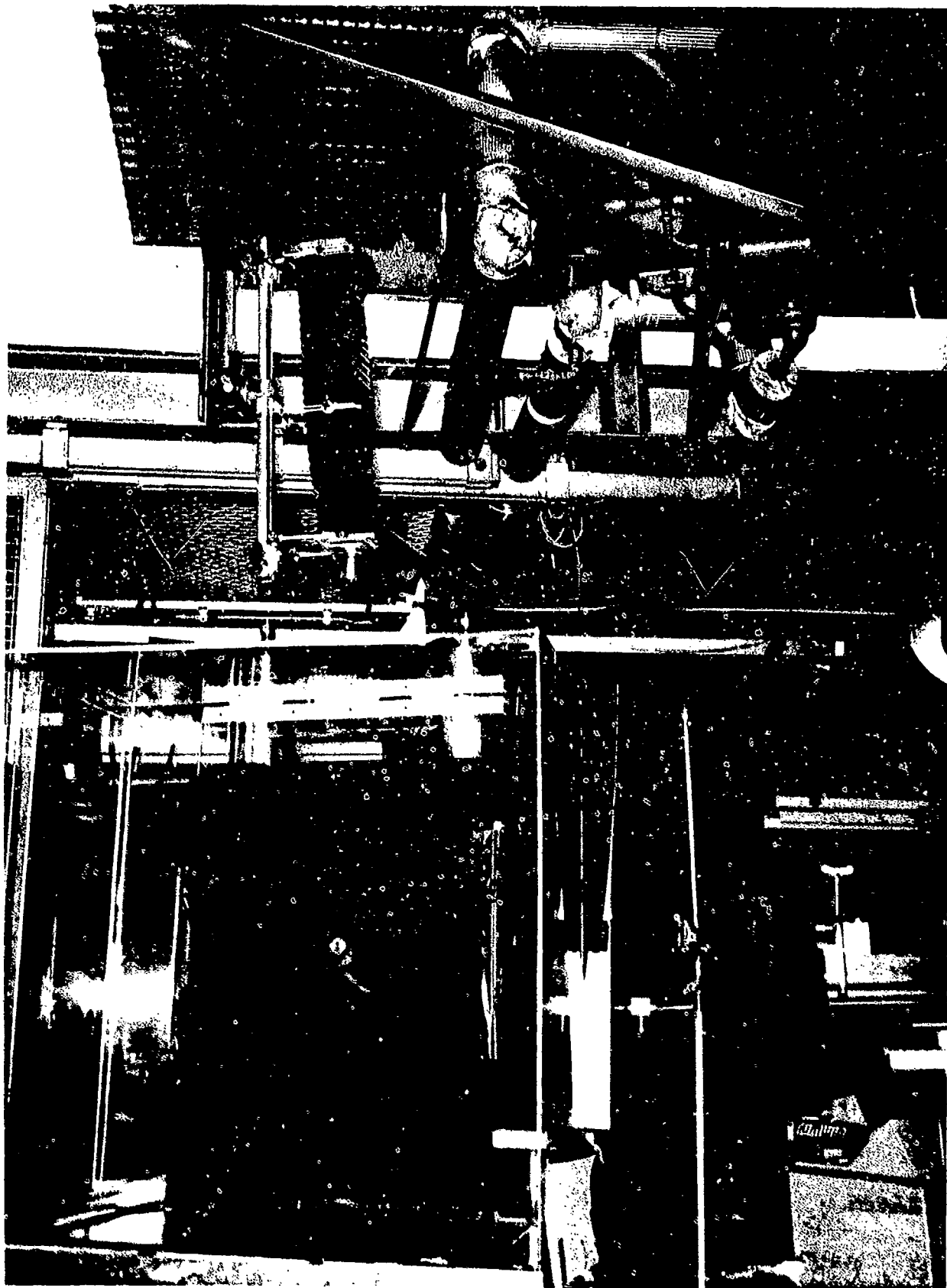


Figure 13. Photographic configuration for nozzle spray imaging.

Imaging of the entire fuel spray of interest was possible on one negative only with the mini wing shear and FCTA facilities. Nozzle sprays were to be analyzed from 0 to 12 cm downstream, necessitating formation of a composite of 3 images as shown in figure 14. To create the mosaics the camera was mounted on a steel bracket which could be repositioned to each of the three imaging locations.

5.5 Image Processing Hardware

With the set of digitized fuel droplet images compiled and stored on magnetic tape, a digital computer becomes the necessary link to perform image processing. Each image consists of an array of digital numbers (DN), each of which represents the value of one picture element or pixel. The storage required for each pixel value is dependent on both the type of data being analyzed and the dynamic range of interest in the stored digital information. Integer, real or complex numbers may be assigned to each pixel as appropriate for the image type or mathematical function being stored. Typically, an 8-bit unsigned integer fills each pixel storage location, i.e., one byte of computer storage. Image data sets to be held in hardware storage devices range in array size anywhere from several thousand to several million pixels. For the AMK task, video digitization produces images containing approximately 262K bytes, while a film digitization may create images of over 4 megabytes. Sufficient disk space must be provided to store a collection of images as they are being processed and allow temporary storage space allocations to hold additional input, output, and intermediate data sets which certain computing algorithms require. At the IPL, the total disk storage capacity exceeds 2900 M bytes, allowing a large multi-user interactive and batch system to catalog and process a wide range of digital imagery.

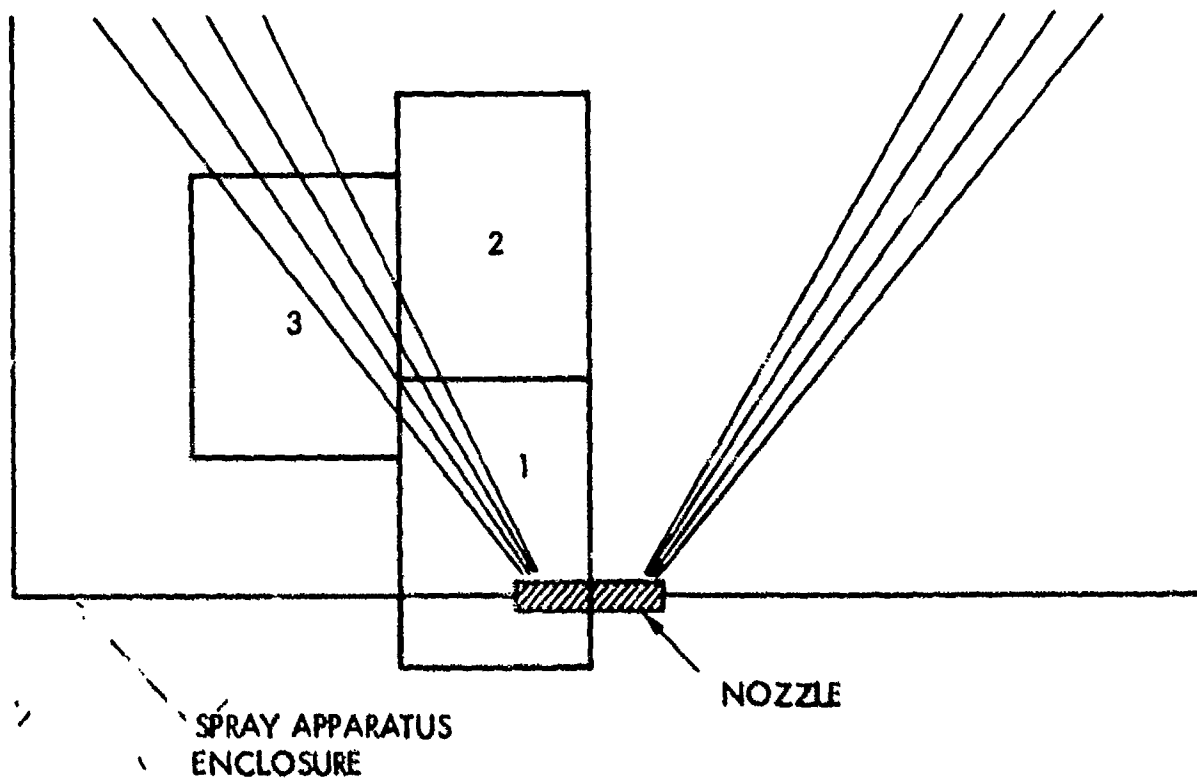


Figure 14. Mosaic construction of nozzle spray images.

Microdensitometer digitization is the initial hardware interface of the recorded fuel droplet data. Under program control, optical density values of the film negative as recorded from a light source passing through the film and aperture are stored in a PDP/8 computer and read on a line-by-line basis onto a magnetic tape. As each tape is generated (containing several separate image files), it is transported to the mainframe computer of the IPL system, an IBM 370/158. There the tape is mounted on a tape drive and the image file is copied onto an allocated data set on one of the CDC 33501-B2 disks. A specialized collection of image processing software and I/O subroutines that was originally developed at the IPL and is currently in operation not only there but at several other educational and research institutions is called VICAR (Video Image Communication and Retrieval)³⁸ [VICAR will be discussed more fully in Section 5.6, but is of consequence here in the hardware interface discussion]. When outside data is first brought to the IPL computer, the software used to copy the data to disk also serves to add a VICAR label to the data set. The first label line within the VICAR label contains image format and size information that is used by subsequent VICAR software programs to interpret the image, while succeeding lines can optionally add verbal image description labels. Image processing tasks typically read and write data very frequently as the input is collected, computed, and output on a line-by-line or block-by-block basis. Therefore, while the actual image processing is being performed, it is almost essential that the data be stored on a direct access storage device such as a magnetic disk. After the image computing has been completed, the data is copied to a magnetic tape file. In addition to the image data itself, annotation information is appended which describes the processing steps and uniquely identifies the particular image. Tick marks are added at the image edges to compute the relative pixel size in the final hard-

copy image, and gray scales are displayed at the top and bottom of the images to control photographic processings. The enhanced, labeled image tape file is then transported to a playback device to create photographic negatives from digital tape data. Most of the fuel droplet images were played back as black-and-white negatives. A DICOMED image analyzer ³⁹ reads the tape file via a PDP 11/40 and then assigns a voltage to the digital readings. The image is reconstructed on a CRT which is then scanned at a pre-selected resolution, the image 'spot' exposing a photographic film negative in raster form. Color playback of digital images at JPL is accomplished using a specialized laser device originally developed for the Viking lander images of the Martian surface. Given the name GRE (Ground Reconstruction Equipment), this machine accepts 9 track, 800 bpi magnetic tapes from the IPL. These digital tapes are converted from their 8-bit format to an analog signal. Acousto-optic modulators are driven by these analog signals to vary red, green and blue laser light levels during the color negative generation. Finally, the color or black-and-white film negatives are sent to the JPL photo lab for standard photographic printing.

5.6 Image Processing Software Development and Methodology

Just as the hardware components of the image processing system must satisfy certain essential requirements, the software design and processing sequence must lend themselves to efficient image manipulation. At the post-image recording stage of the experiment, image processing options and the ordering of each step become critical to the successful detection of fuel droplets. Several different objectives may require individual procedures that will connect in an overall systematic technique. Ultimately, automation of the fuel droplet detection process will reduce human interpretation bias and allow

an expedient characterization of the jet fuel sprays with repeatable accurate results.

Microdensitometer digitization produced the preliminary imagery for examining the nature of laser-illuminated droplets. For the first set of jet fuel nozzle spray negatives, a series of digitizations of the same negative subsection was made to compare the effects of different digitizer aperture/-spacing combinations. Fig. 15 shows an entire Jet A fuel nozzle spray image that covers a 2000 x 2000 element pixel matrix made with the microdensitometer set to a square aperture of $(50\mu\text{m})^2$ and a spacing of $50\mu\text{m}$ between adjacent pixel measurements. A first priority of the digitization tests was to achieve a maximum resolution with which to detect as small a droplet as possible given the existing optical constraints (approximately a 1:1 magnification) and film resolution capability. For a subscene of the fuel spray, a set of higher resolution images was produced (figs. 16 thru 21), relocating the upper left hand corner of each new image to within 5 microns of the same position on the previous scan. While figure 15 encompasses an area of 100 cm^2 on the photograph image, the subsequent figures contain 1 cm^2 (fig. 16), 0.26 cm^2 (figs. 17 and 18), 6.6 mm^2 (figs. 19 and 20), and 2.40 mm^2 (fig. 21). Thus the digitization process allows area magnification factors of over 4000x if film resolution and image sharpness allow. Table 1 lists the aperture sizes and spacing used to form each of these images. The total number of pixels forming an image may be found by multiplication of the number of lines in an image by the number of samples per line. While the spacing increment sets the image scale, the aperture width (in conjunction with the spacing) controls the quality of the A/D conversion through the degree of pixel sampling overlap. The lower the spacing-to-aperture ratio, the higher the degree of overlap. A consequence of undersampling (little or no overlap) the continuous film signal



Figure 15. Jet A fuel spray images resolved digitally with a 2000 x 2000 pixel array.

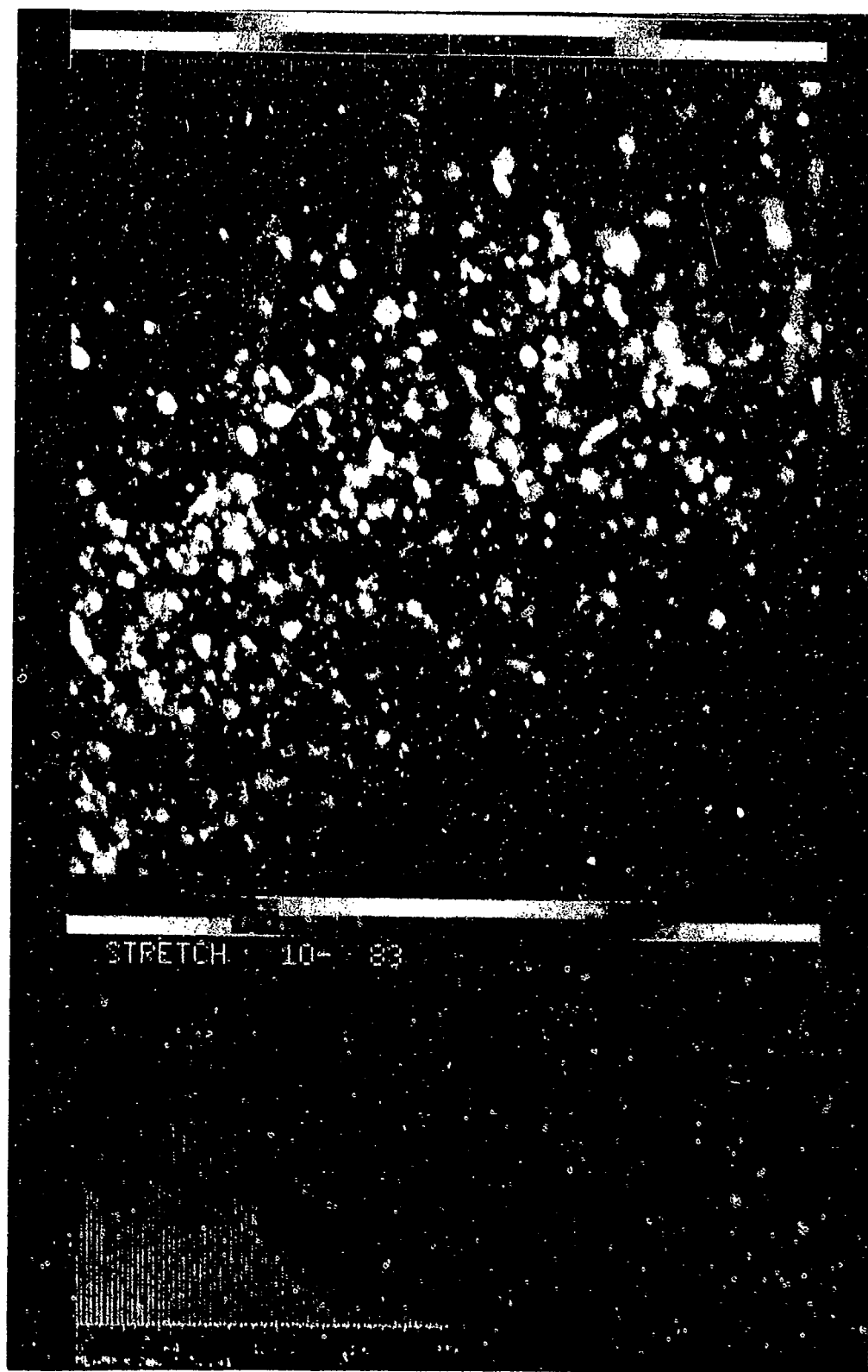


Figure 16. Portion of the Jet A fuel spray corresponding to 1 cm^2 on the negative, 512×512 pixel array, $20 \text{ }\mu\text{m}$ microdensitometer aperture and spacing.

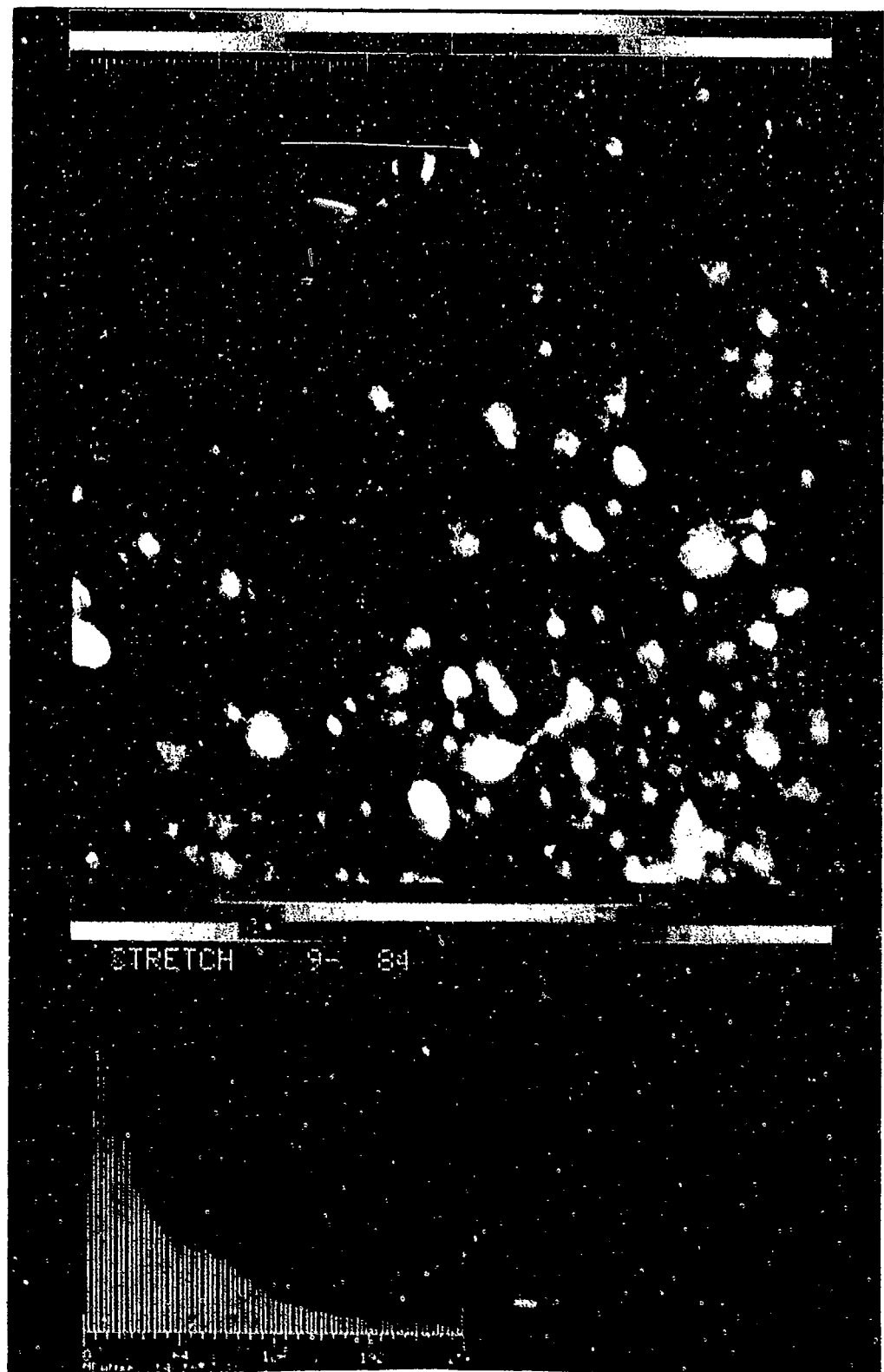


Figure 17. Portion of the Jet A fuel spray corresponding to 0.26 cm^2 on the negative 512×512 pixel array, $20 \text{ }\mu\text{m}$ microdensitometer aperture with $10 \text{ }\mu\text{m}$ spacing (50% oversampling).

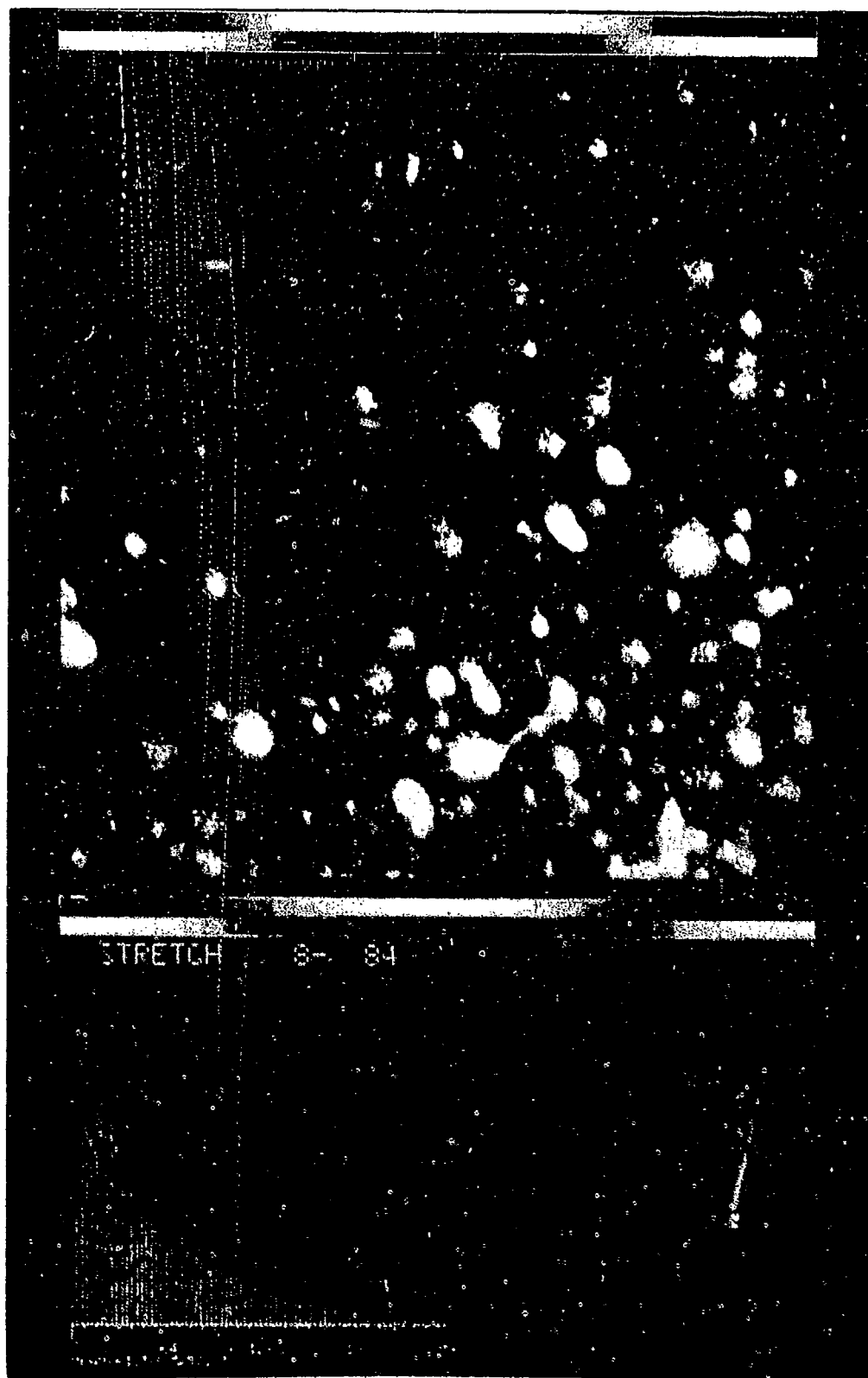


Figure 18. Portion of the Jet A fuel spray corresponding to 0.26 cm^2 on the negative 512 x 512 pixel array, 10 μm microdensitometer aperture and 10 μm spacing (no oversampling).

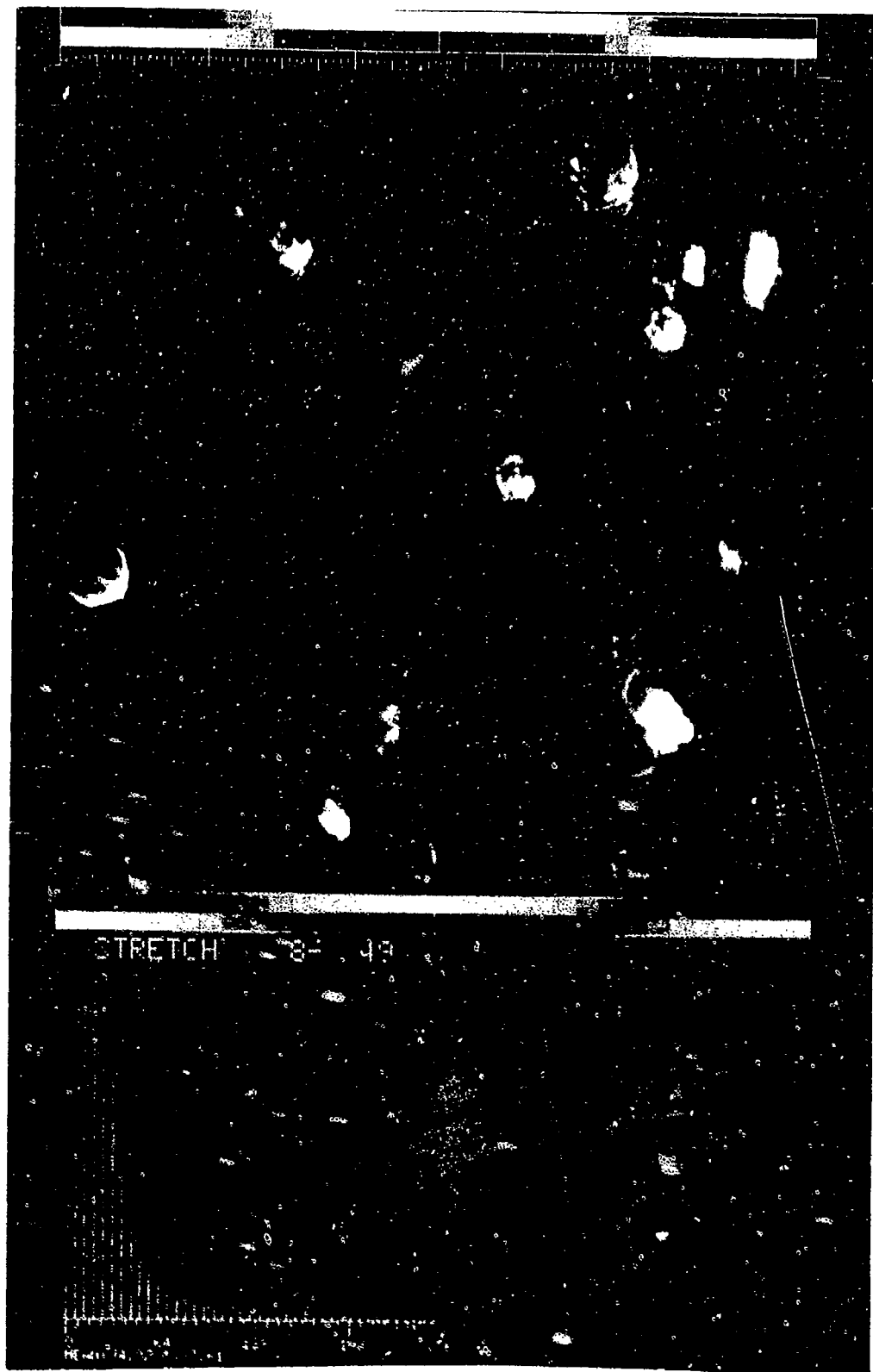


Figure 19. Portion of the Jet A fuel spray corresponding to 6.6 mm^2 on the negative, 512×512 pixel array, $10 \text{ }\mu\text{m}$ microdensitometer aperture and $5 \text{ }\mu\text{m}$ spacing (50% oversampling).

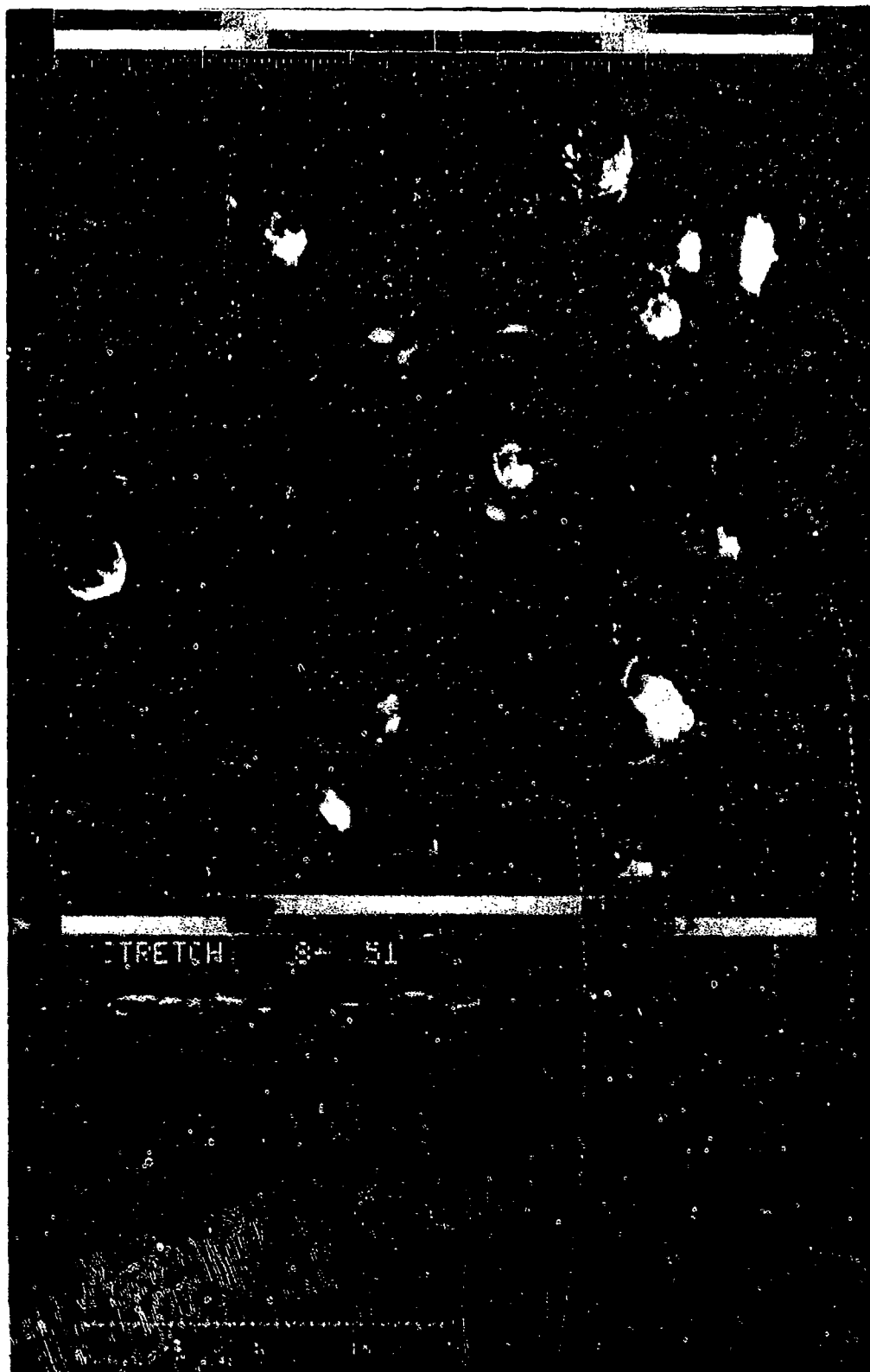


Figure 20. Portion of the Jet A fuel spray corresponding to 6.6 mm^2 on the negative, 512×512 pixel array, $5 \text{ }\mu\text{m}$ microdensitometer aperture and $5 \text{ }\mu\text{m}$ spacing (no oversampling).

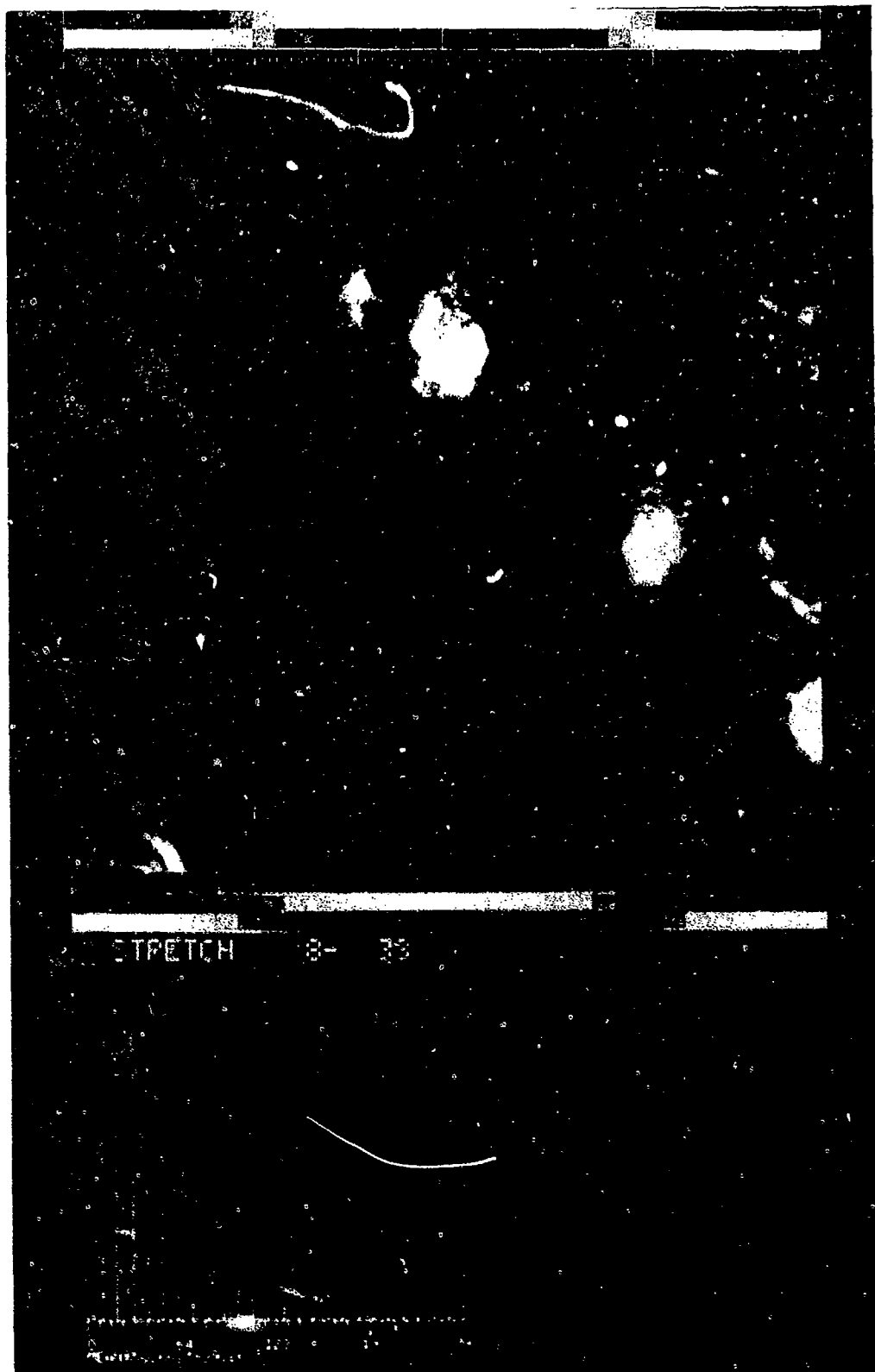


Figure 21. Portion of the Jet A fuel spray corresponding to 2.4 mm^2 on the negative, 512×512 pixel array, $5 \mu\text{m}$ microdensitometer aperture, 3 m spacing (40% oversampling).

is that a folding back of spectral energy produces an aliasing error^{26, 40}. This is because of possible undersampling of high frequency image components. They may then appear as lower frequency artifacts superimposed on the digitized image. Subsequent filtering cannot entirely remove the aliasing artifacts, thereby justifying an overlapped sample spacing during digitization. Because a 50% smaller spacing doubles the image scale, visual comparison between differently spaced images is difficult.

Microdensitometer aperture and spacing were chosen for this experiment with the goals of resolving 10 μ m drop images while reducing aliasing effects as much as possible. A 5 μ m aperture was felt adequate to resolve the droplet. Current densitometer practice is to choose a spacing approximately 20% smaller than the aperture for aliasing elimination, so a 4 μ m spacing is used. Because of concern that such small apertures might resolve film grain, DN values were plotted for an image using various apertures and spacing. No significant increase in the high frequency component of the data, indicating grain resolution, was noted.

When forming images for human viewing it is often necessary to enhance the contrast of the final image before printing. This is partly because of the tendency of the digitizer to compress brightness levels, decreasing contrast, when operated in some modes. Variations in saturation of negatives resulting from fuel density variations in the spray may be reduced through enhancement. Stretching is the most often used form of contrast enhancement. A histogram is created which lists the number of pixels having each of the available DN levels. The pixel DN assignments are then shifted away from center so that the dimmest pixels are forced to black, while the brightest pixels are forced to white. The upper and lower 2% of the pixels are saturated in this way for "quick look" processing so that the remaining pixels span the dynamic range more fully.

Table 1

MICRODENSITOMETER SETTINGS FOR IMAGE DIGITIZATION

Image Figure Number	Aperture	Spacing	Number Of Lines	Number of Samples/Line
17	(50 μ m) ²	50 μ m	2000	2000
18	(20 μ m) ²	20 μ m	512	512
19	(20 μ m) ²	10 μ m	512	512
20	(10 μ m) ²	10 μ m	512	512
21	(10 μ m) ²	5 μ m	512	512
22	(5 μ m) ²	5 μ m	512	512
23	(5 μ m) ²	3 μ m	512	512

Figure 22 shows a digital "quick look" image of one of the fuel spray images that have been analyzed in depth for this study as discussed more fully in section 6.1. The data digitized for these analyses are examples from the nozzle spray, mini wing shear and FCTA apparatuses. For the nozzle spray tests, cruise flow rates were considered for neat Jet A and Jet A + 0.30% FM-9. Considerable noise created during microdensitometer digitization is apparent, particularly in figure 22a.

Before digitization it is necessary to choose the region of interest on the negative. Using the nozzle spray experiment as an example, the drop size distribution is to be determined at discrete downstream distances. Areas on the negative (windows) are chosen for each of these axial locations as shown by figure 23. An enormous amount of data is present in a high resolution image of 129 cm^2 area (i.e. each of the 4 x 5 inch technical pan negatives produced). Using the $5 \mu\text{m}$ diameter aperture and $4 \mu\text{m}$ spacing of the microdensitometer to ensure resolution of the smallest droplets of interest, complete digitization of the negative would result in over 5×10^8 data points of 8 bits each. Reduction of this quantity of data is an important reason for the use of smaller windows. In the case of the nozzle spray, existence of axial symmetry allows the use of windows spanning only 1/2 the spray width. But because of the possibility that the spray is not homogeneous in size across its half-width, a window of sufficient height must be chosen to span the entire half-width. Typical windows were of 2 mm width and up to 14 mm height for the nozzle spray representation of such a long range with hardware devices designed mainly for square images requires mosaicing of images into as many as 4 discrete subimages. As an example figure 22 is divided into 3 parts which fit together end to end (the right side of 22a joins the left side of figure 22b). The automatic contrast enhancing stretch discussed earlier has

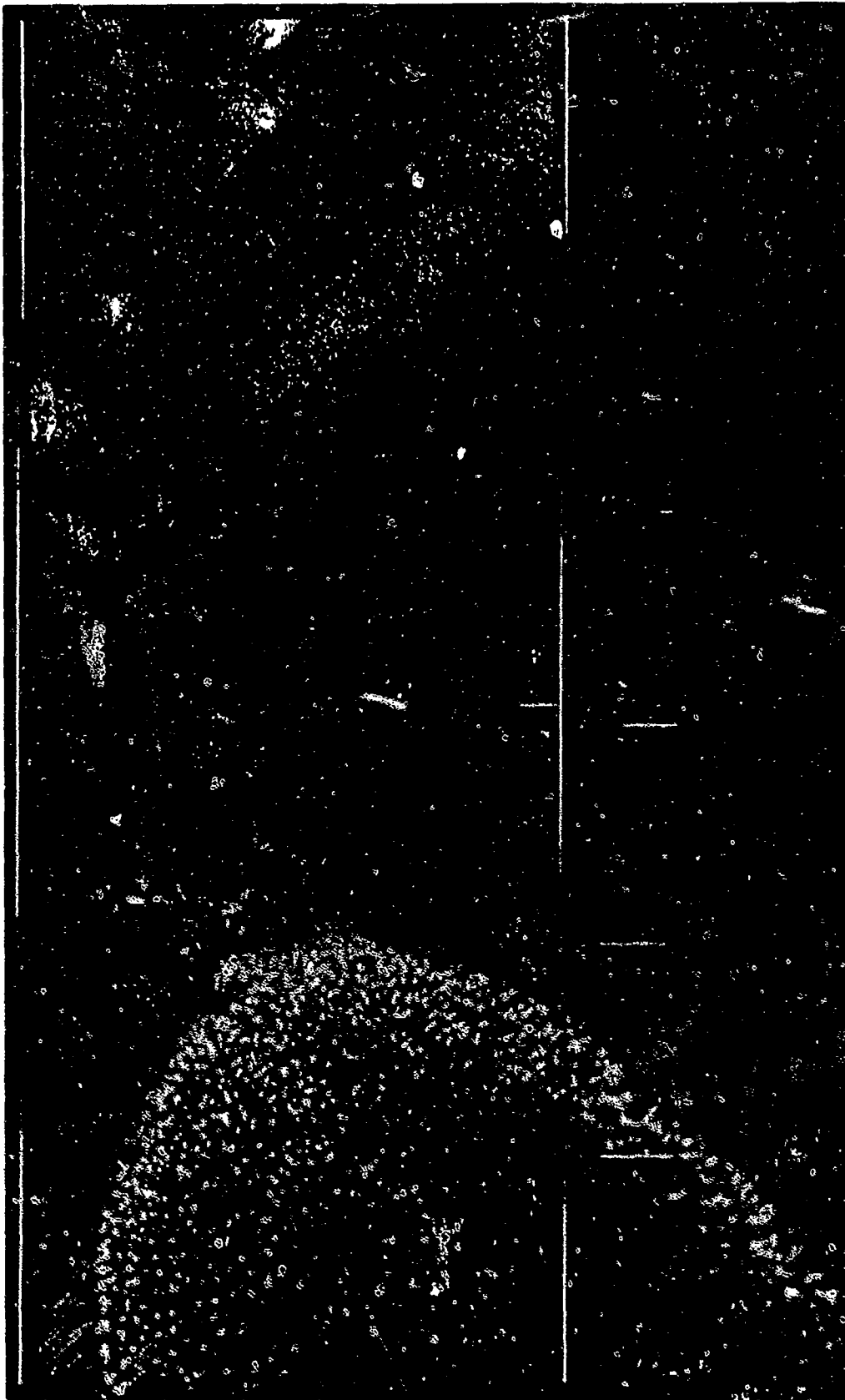


Figure 22. Three subimages composing the Jet A sea level takeoff spray image window, 2 cm axially from the nozzle. Stretching has been performed individually to optimize resolution within each subimage (a) first third, (b) second third, and (c) final third. (1 of 3 pages)

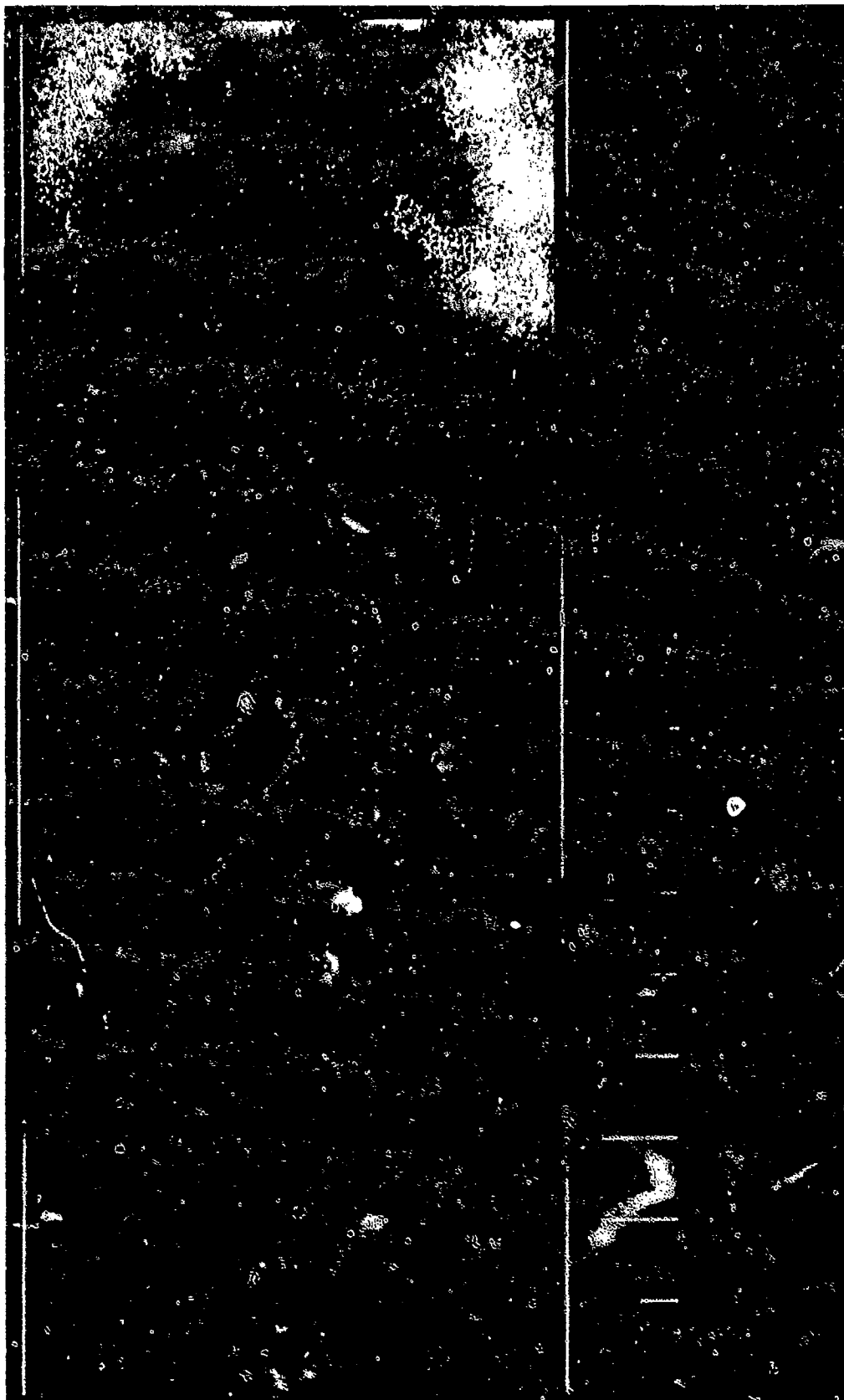


Figure 22. Three subimages composing the Jet A sea level takeoff spray image window, 2 cm axially from the nozzle. Stretching has been performed individually to optimize resolution within each subimage (a) first third, (b) second third, and (c) final third. (2 of 3 pages)

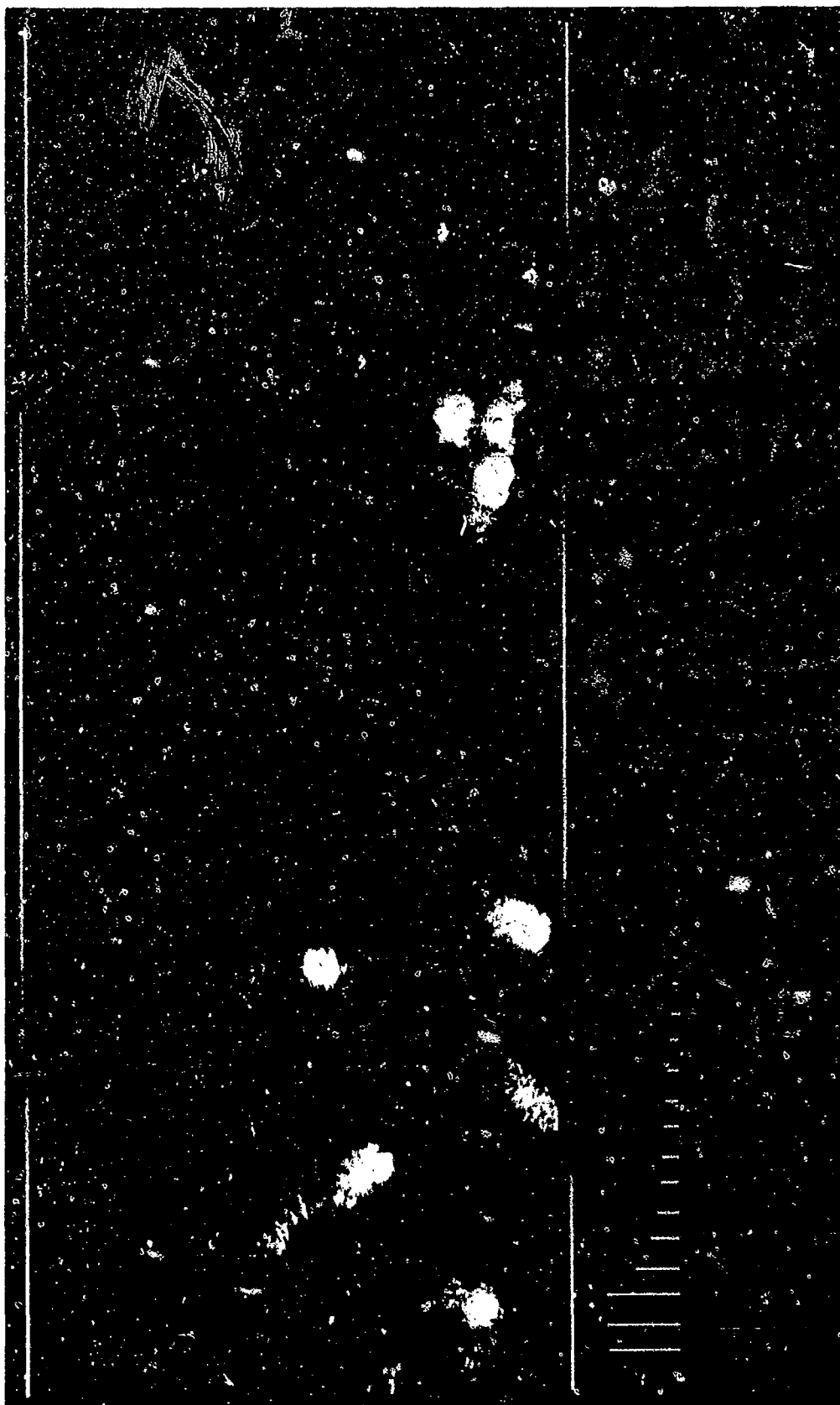


Figure 22. Three subimages composing the Jet A sea level takeoff spray image window, 2 cm axially from the nozzle. Stretching has been performed individually to optimize resolution within each subimage (a) first third, (b) second third, and (c) final third. (3 of 3 pages)

WINDOW EXTENSIONS USED IF
NECESSARY TO COVER THE
ENTIRE FUEL SPRAY. VARIABLE
HEIGHTS WERE SELECTED FOR
EACH NEGATIVE.

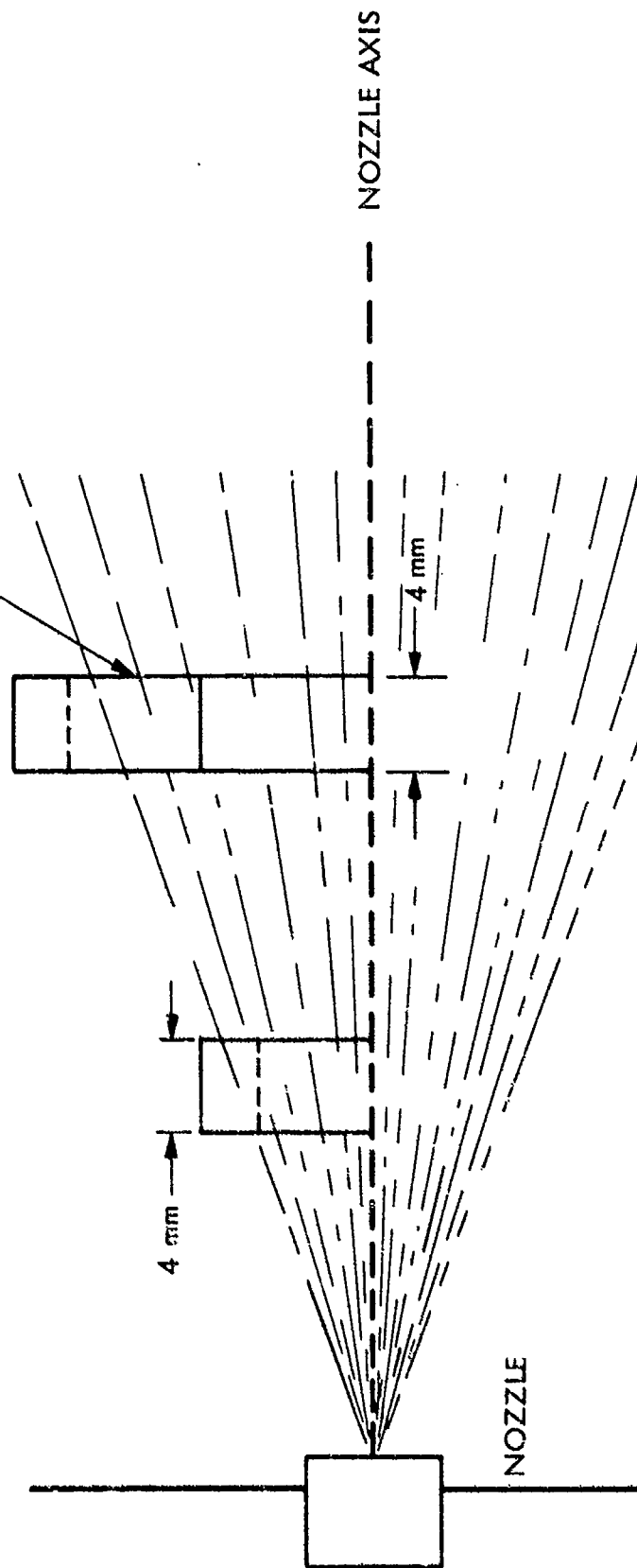


Figure 23. Window configuration for fuel spray image processing.

been applied to these images to render them suitable for viewing. This unfortunately has a different effect on each subimage depending upon the relative amount of bright and dark areas it contains. A different pixel stretch is therefore applied to e.g. figure 22a than to figure 22b. This stretched version of the subimage is produced only for viewing. It is not used in droplet counting because it would cause uneven weighting of droplets in subimages from different radial spray locations. It also gives an uneven appearance to the mosaic when viewed as a whole. To illustrate a mosaic whose subimages are treated uniformly, figure 24 (a, b and c) was produced. This is identical to figure 22 except that one stretch has been applied to all of the subimages instead of applying individually determined stretches to each subimage. The mosaic now appears more internally consistent. This viewing method is inadequate because window sections of denser fuel mist regions have many more high DN pixels owing to the larger amount of scattered light. Thus, by applying the same contrast stretch to these images as to those with lower mean DN values, the effect of the correspondingly lower upper stretch limit is to saturate the image at the high end, producing the large white (255 DN saturation) regions as seen on subimages 24b and c.

At this stage identifying and counting the fuel droplets on each image and compiling overall statistics for each window is the fundamental image processing objective. Pre-processing the images to remove unwanted information is the initial step in such a detection process. An algorithm then searches the image to detect droplet pixels based on an intensity threshold and accumulates droplet statistics. Output takes the form of line printer listings and graphic plots describing critical droplet parameters that relate to the potential for mist flammability.

The 3 x 3 pixel low pass filter may be represented diagrammatically as

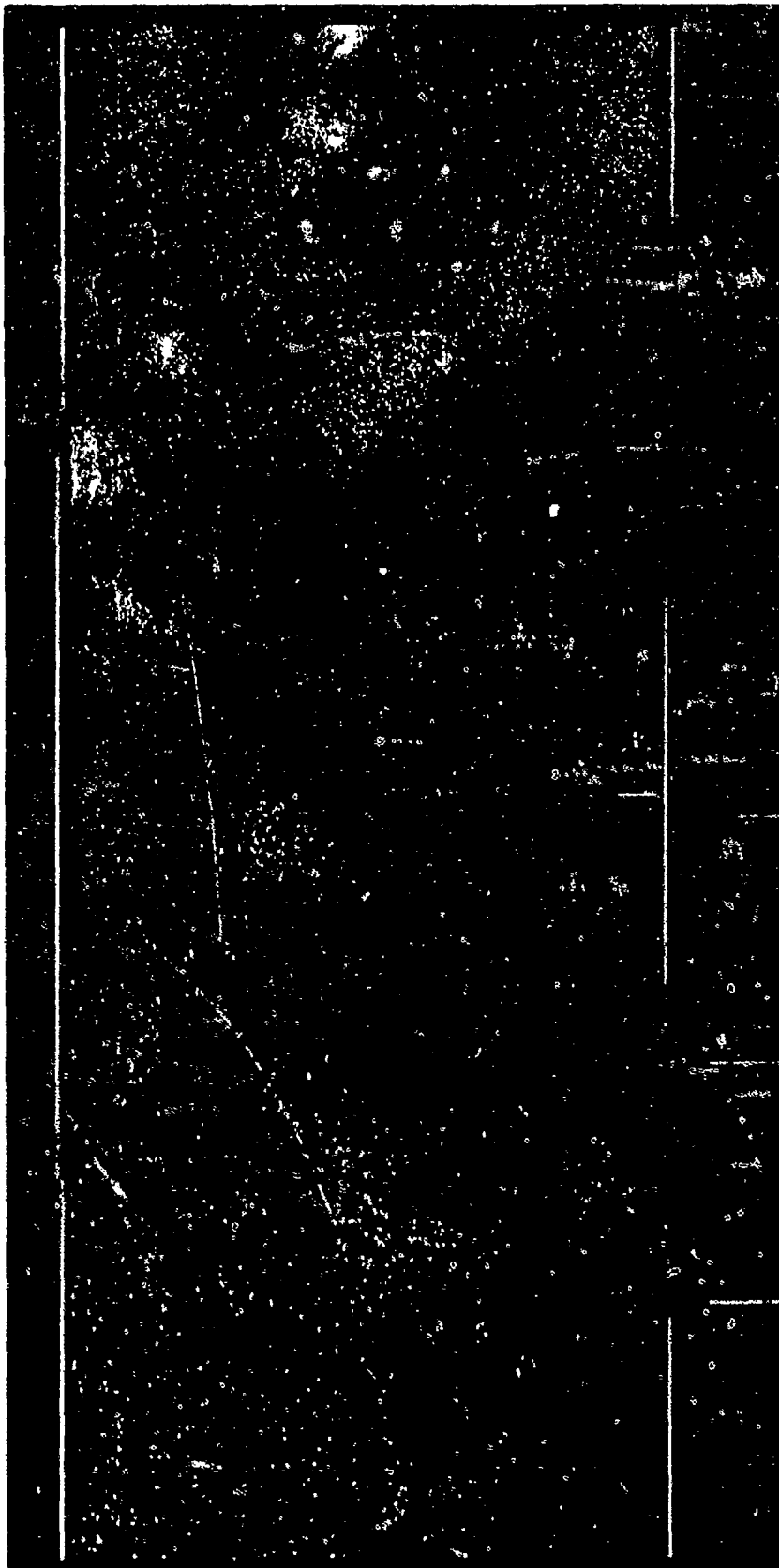


Figure 24. Three subimages composing the Jet A sea level takeoff spray image window, 2 cm axially from the nozzle. A single stretching technique has been applied uniformly to all subimages to allow visual mosaicing. (a) first third, (b) second third, and (c) final third. (1 of 3 pages)



Figure 24. Three subimages composing the Jet A sea level takeoff spray image window, 2 cm axially from the nozzle. A single stretching technique has been applied uniformly to all subimages to allow visual mosaicing. (a) first third, (b) second third, and (c) final third. (2 of 3 pages)



Figure 24. Three subimages composing the Jet A sea level takeoff spray image window, 2 cm axially from the nozzle. A single stretching technique has been applied uniformly to all subimages to allow visual mosaicing. (a) first third, (b) second third, and (c) final third. (3 of 3 pages)

$$\begin{array}{ccccc}
 P_{i-1, j-1} & P_{i-1, j} & P_{i-1, j+1} \\
 P_{i, j-1} & P_{i, j} & P_{i, j+1} \\
 P_{i+1, j-1} & P_{i+1, j} & P_{i+1, j+1}
 \end{array}$$

where

$P_{i,j}$ = pixel at row i , column j . If W_{ij} is the filter weight associated with the pixel p_{ij} , the filtering algorithm is

$$P_{ij} = \frac{\sum_{x=i-1}^{i+1} \sum_{y=j-1}^{j+1} P_{x,y} W_{x,y}}{\sum_{x=i-1}^{i+1} \sum_{y=j-1}^{j+1} W_{x,y}}$$

Thus if the pixel weight is 1 for all pixels (unweighted filter) the center pixel in a box is assigned the value of the average pixel value of all nine pixels within the box. Thus 3 x 3 filters were generated by assigning W_{ij} the value of 1, 2, or 3 while all $W_{i\pm 1, j\pm 1}$ values were left at 1. These correspond to unweighted, double and triple centerweighted filters. This type of low pass filter achieves the effect of smoothing amplitude spikes in data appearing within the box. Higher center pixel weighting results in less smoothing. If noise caused by small grain disturbances or very small drops on the order of 1 pixel diameter were present in the picture the filter would lower their DN values. In practice a particular threshold level is chosen either by operator choice or a suitable algorithm. Pixels with DN levels below the threshold are assigned 0 DN (black) while pixels above the threshold are assigned a DN of 255 (bright white). Upon filtering, a light pixel surrounded by darker pixels will also become darker and may fall below the threshold. This is the way in which high frequency noise is eliminated by a low-pass filter.

Following the filter operation, the images were counted by a computer algorithm currently operating in a VICAR program originally designed to count

and catalog stars. The key principle of the algorithm is the application of an intensity threshold assigned by a parameter input. As each line is processed, continuous segments whose pixel DN values equal or exceed the given threshold are assigned a unique identification value. Droplet parameters, being compiled line-by-line, are updated for each concatenation or generated for each new initial segment. These parameters include summation of individual pixel intensities, the total pixel count per particle, the image coordinates of the extent of each droplet, the droplet centroid coordinate and the droplet characteristic length (the square root of the imaged drop area divided by π). All of this information is written on a disk data set as a catalog whose information can be retrieved by other VICAR programs. Besides providing a listing of the parameters for each counted droplet, the program can generate plots describing the frequency distributions and cumulative distributions of the area, perimeter, and characteristic length values. The output image from the program is identical to the input image except that all particle segment endpoint pixels throughout the image are assigned a DN value of 255. By applying a linear stretch to this output image such that all DN values below and including 254 are forced to zero, the resulting image displays only the particle boundaries, line-by-line, as the algorithm recognized them. A minimum droplet size can be input to act as a type of pseudo-lowpass filter, rejecting those droplets composed of less than a certain number of pixels. Scaling is also incorporated so that a pixel width is interpreted as a linear scale value in microns.

In generating images of particle outlines used in drop counting and measurement, two parameters may be varied, the center weight of the filter and the threshold DN value. Figures 25 through 29 show the particle boundary images for four filter conditions unfiltered and center weights of 1, 2 and 3,



Figure 25. Threshold derived outline; image DN cutoff 22.



Figure 26. Threshold derived outline; image DN cutoff 18.

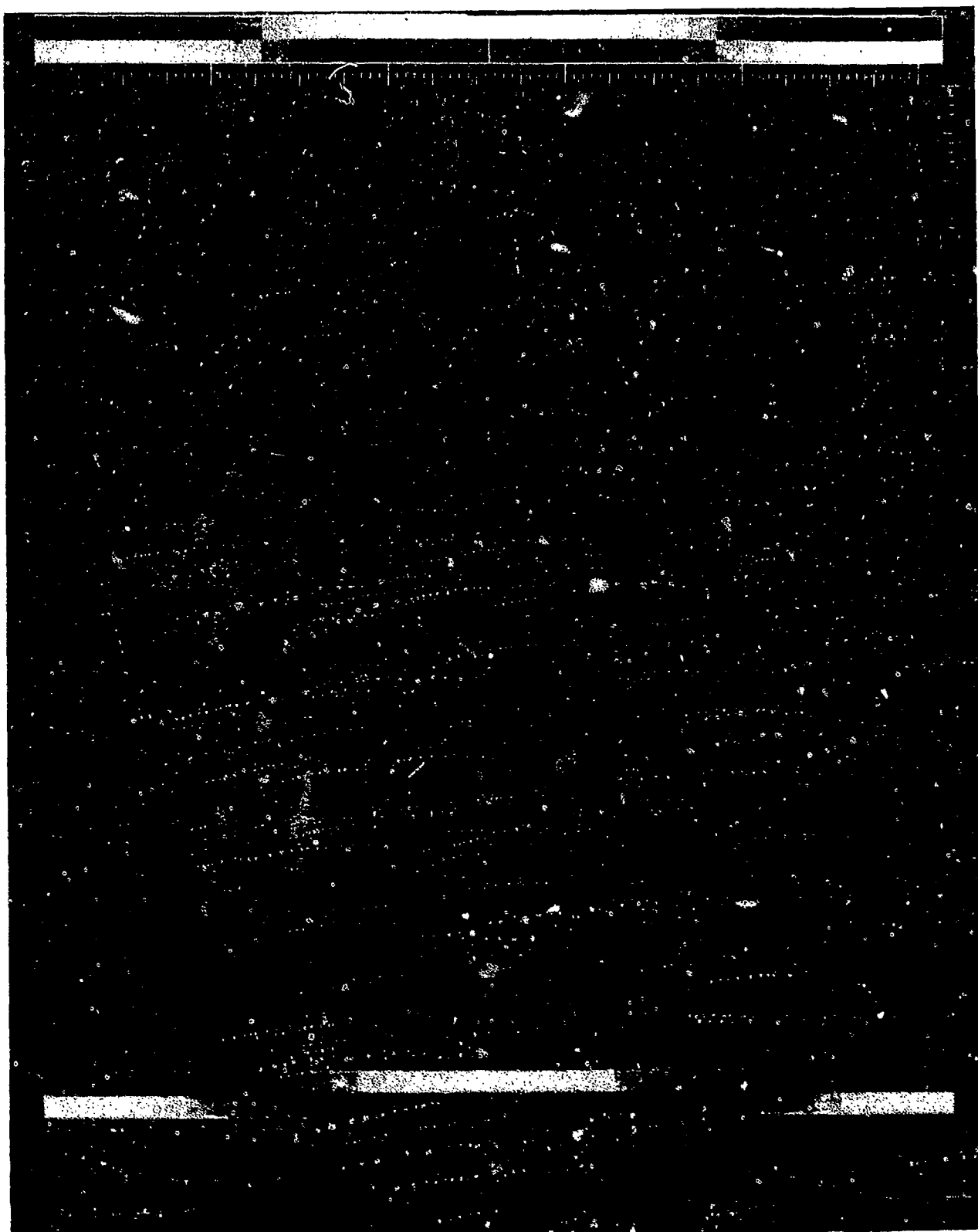


Figure 27. Filtered outline image; DN cutoff 18, 3 x 3 filter, center triple weighted.

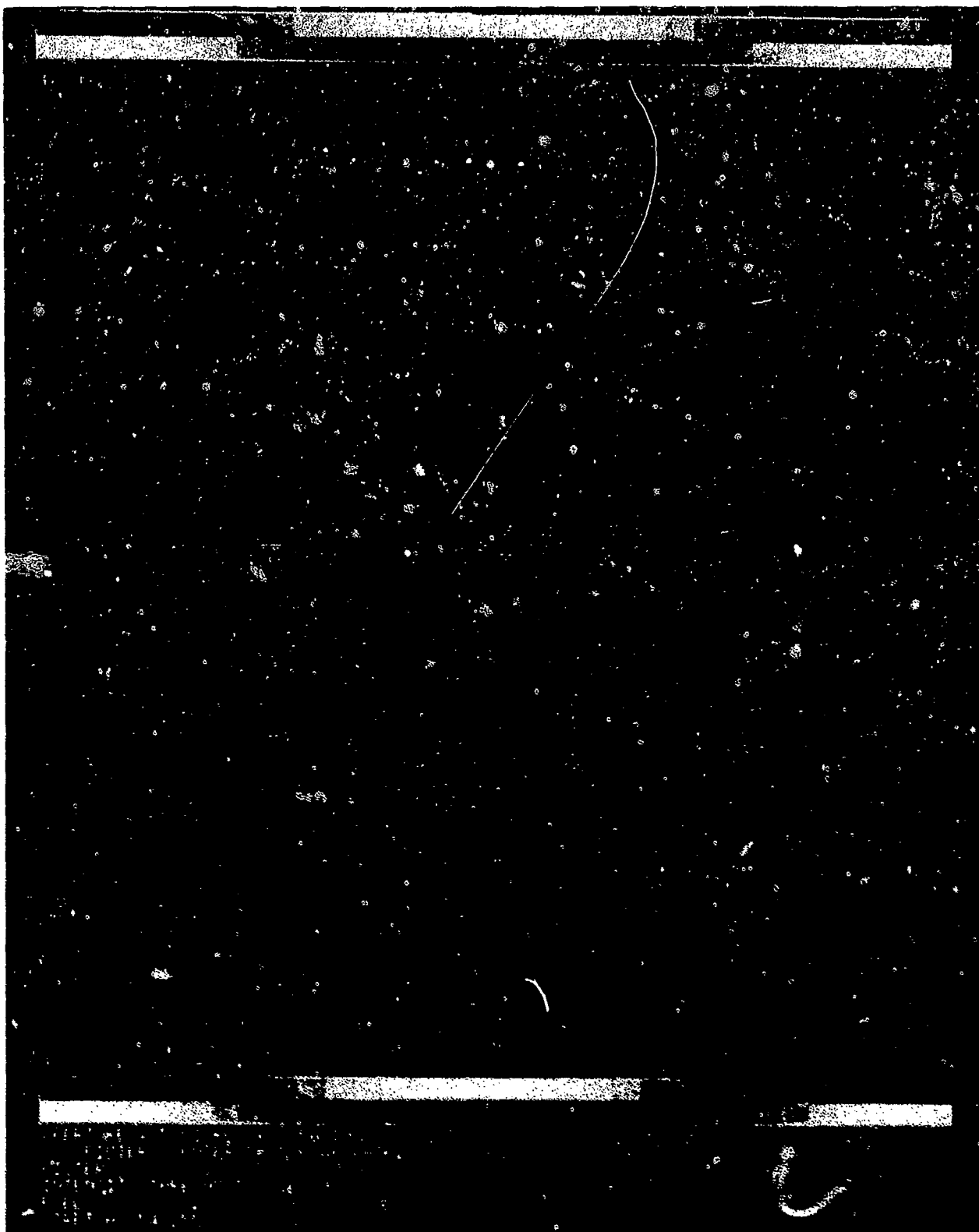


Figure 28. Filtered outline image. DN cutoff 18, 3 x 3 filter, center double weighted.

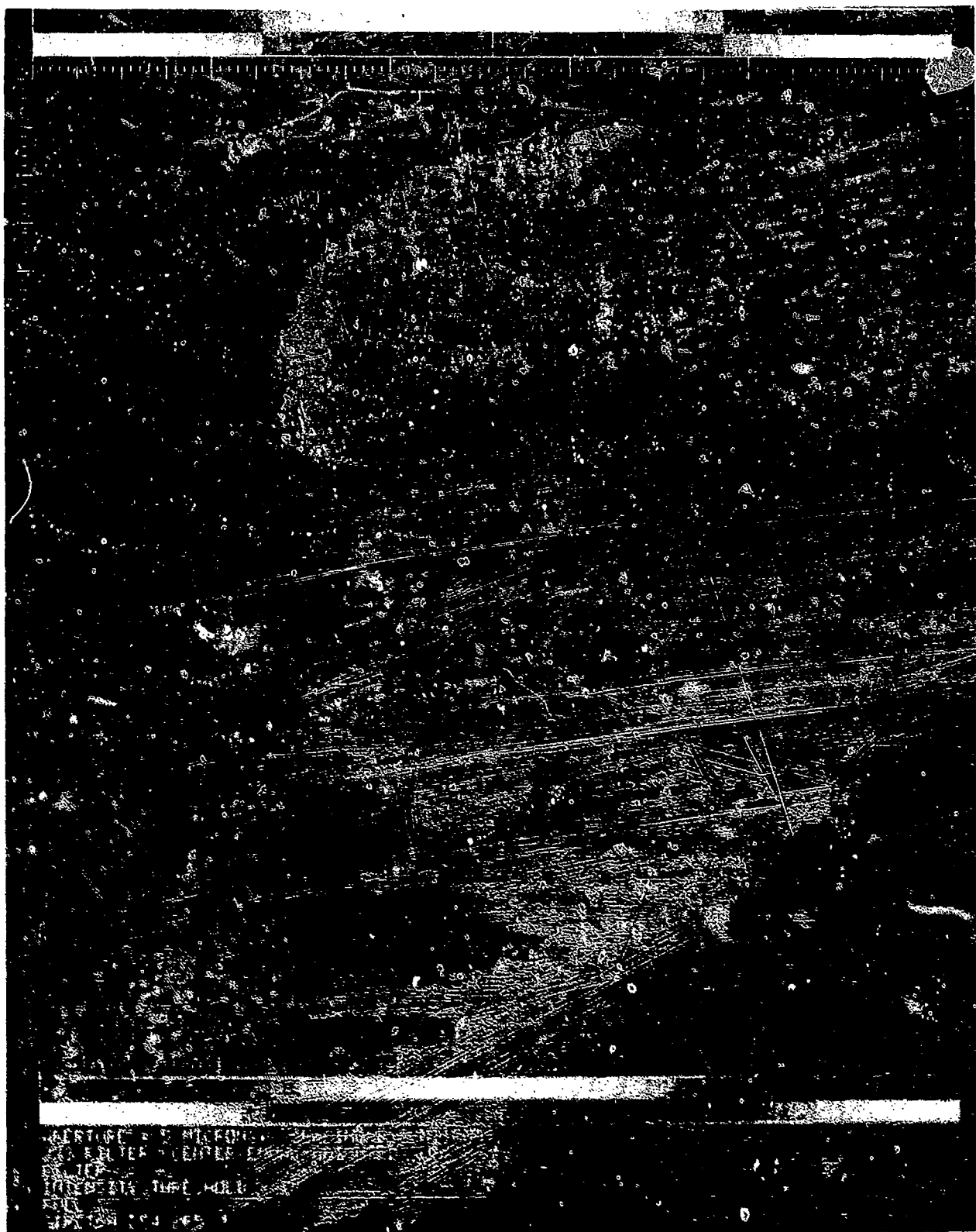


Figure 29. Filtered outline image. DN cutoff 18, 3 x 3 filter, center single weighted (uniform weighting).

and three intensity thresholds. Just as a larger filter box may further reduce individual bright pixel DN values, a higher intensity threshold will selectively remove dimmer pixels from the counting process. As the experimental data were counted, the need arose for an iterative adjustment of the filter box size, the minimum particle area, and the threshold value. Different experimental conditions produced wide variations in particle statistics.

Particle sizes do not depend strongly on the threshold value chosen since edge gradients are very steep. However the total number of droplets counted changes considerably with threshold DN. This is because at low threshold values the effect of the filter is diminished. Also, droplets lying just out of the laser plane are bright enough due to refraction of scattered light to be included in counting at low threshold levels. Experimentation and comparison with original images led to an automated scheme. It was found that the closest agreement with perceived droplet densities was achieved by setting the threshold value 1 standard deviation in DN above the mean DN of the unprocessed digital image. For window subimages, a mean, μ , and standard deviation σ , were computed for the combined images so that the same processing treatment was applied to an entire window.

The effect of threshold level alone is shown by figures 25 and 26 resolved at threshold DN of 22, 20, and 18, respectively. As the threshold DN is lowered, the number of droplets present increases. Figures 26 through 29 show the progressive effect of the low pass filtering. All are formed at DN thresholds of 18, but fig. 26 is unfiltered while fig. 29 is filtered with an equal filter weighting. Again the tendency with increasing filtering is to reduce the number of droplets in the image. Filtering does not eliminate more dimly illuminated drops as selectively as thresholding but affects smaller drops much more than larger ones. After final parameter adjustments were

made, a 5 x 5 lowpass filter was used. This resulted in a minimum droplet size resolution of 4 μm diameter.

Conclusions from the image processing effort:

- 1) Raw digitized images produced from film imaging contain artifactual information as a result of the random noise introduced from both the film grain structure and the digitization process. Two-dimensional lowpass filtering, a standard image processing enhancement technique, is successful at removing this extraneous data from the fuel particle counting process.
- 2) In order to obtain a comprehensive flammability determination based upon droplet size characteristics, two prerequisites must be met: a) a large field of view to measure the droplet parameters and their variations across the flow field of the experiment, and b) an unusually high digital image resolution capable of measuring droplet images with diameters on the order of ten microns. This unique combination of requirements necessitates the accumulation of massive amounts of data which must be optimally processed to maximize processing speed. From an image processing standpoint, the computer system design and algorithm development are both impacted to accommodate the data load and achieve a high processing efficiency. An example of an optimization technique is the use of the digital video processor in the De Anza Image Display System, which is capable of performing lowpass convolutional filters on the image data directly in the machine hardware, enabling time savings of several orders magnitude.
- 3) Film digitization via a microdensitometer is costly in terms of the bulk of data requiring analysis and the corresponding time expended in physically scanning each film negative. Direct imaging and digitization or

film digitization alone with a vidicon camera will achieve a real-time process for digitizing the fuel data and storing the resultant digital image.

- 4) The mode of film digitization used to create the images studied in this report yielded DN histograms with comparatively low standard deviations. Furthermore, the separation of the droplet and background intensities was not well defined. Subsequent selection of an intensity threshold level for droplet counting became an interactive procedure subject to a high level of DN sensitivity.
- 5) Large-scale intensity gradients did not appear in the digital images. Such gradients may arise from vidicon sensor characteristics or the nature of the object illumination. In these experiments, the attenuation of the laser light by particle scattering close to the illumination source could potentially lower the average intensity of light reaching the more distant droplets and thereby produce an image gradient. A gradient effect was not apparent in each individual image and therefore a removal technique was not applied. Such a removal would involve a high-pass filter applied to every column in the image oriented normal to the gradient, thus removing any low frequency gradient occurring across the image columns.
- 6) The intensity threshold counting algorithm was successful in outlining droplet edges as they were recorded on film. For larger droplets containing twenty or more pixels, a visual inspection comparing the 8-bit digitized images with their particle outline counterparts revealed a close correlation of computer-recognized droplets with human-recognized droplets.
- 7) Droplet shape statistics are highly dependent on the range of droplet sizes included in the counting operation. While lowpass filtering serves

to remove those droplets at the low end of the size distribution, very large droplets strongly affect the overall SMD of the images. Manual inspection of the images is necessary to verify the existence of larger droplets and a restriction of upper size limits is needed to confine the droplet size range.

- 8) Fuel droplet signatures vary widely in the current library of digital fuel spray imagery. Generally, all droplets exhibit an internal intensity gradient which grows inward from the edge and then declines at the center. This gradient may prove to be helpful in the detection of droplet edges. The magnitude of the gradient and of the central density plateau is affected by the droplet size and the irregularity of the droplet perimeter. Those drops which lie at or beyond the edges of the laser-illuminated sheet of light contain optically "hollow" interiors; i.e., the gradient function falls off sharply toward the droplet center. This phenomenon is associated with the diffraction properties of the droplets.

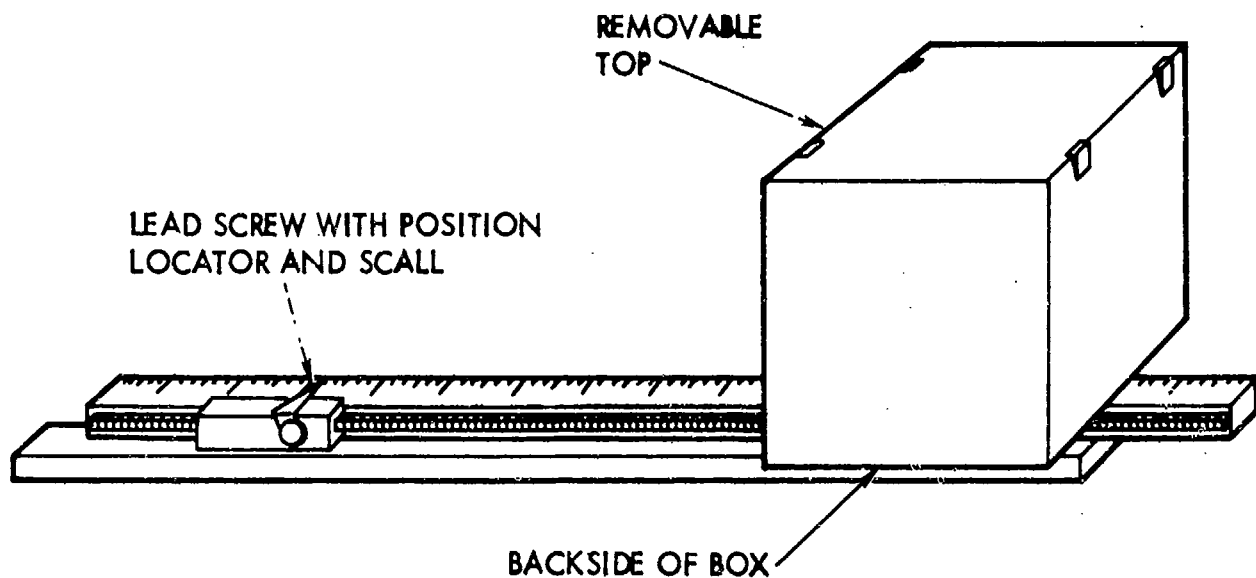
5.7 Control Experiment

As a check on drop measurements derived via the image processing system and to gain experience with the capabilities of alternative counting techniques, an independent drop size measurement system was sought. Because of its widespread acceptance and use and its basic simplicity, the slide impact technique was adopted. This method uses a coated slide on which drops impact, leaving an impression proportional in size to the droplet diameter. These impressions are then measured and counted manually with a microscope. There are, however, several disadvantages associated with this method.⁸ The primary one is obtaining a statistically valid representation of the spray. Smaller, slower drops tend to follow the airstream around the slide, reducing

the number of smaller droplets which impact it. In addition, larger drops with Weber numbers greater than a certain critical value tend to split on impact. There are also problems in obtaining an accurate drop size distribution. Not only do a great number of drops and hence slides need to be analyzed, but operator biases also affect the count. Another drawback is in the determination of a reasonable impression coefficient, that is, determining the relationship between the actual droplet and the impression diameter. Most of these problems can be addressed to some degree; however, the biases caused by smaller drops being carried by the airstream create uncompensated errors indigenous to this method.

For this study, 5 cm square glass slides are coated until nearly opaque⁹ with soot from a kerosene lamp. These slides are placed in a metal container with a removable lid as shown in figure 30. A shutter with speeds ranging from 1 second to 0.002 seconds is mounted on the container and is triggered by a cable release. The device is mounted on a lead screw to provide lateral movement across a spray cone.

The entire device is placed inside the nozzle spray testing apparatus with the shutter opening level with the nozzle. Samples are taken by triggering the shutter, allowing a volume of droplets to pass into the container and impact on the slide, forming impressions. After several settings of the nozzle spray testing apparatus were tried, the idle fuel flow setting of 23 atm on the primary nozzle and 0 atm on the secondary nozzle was chosen as giving acceptable slides while still providing results comparable to the image processing studies. An acceptable slide has little or no droplet impression overlap. The higher fuel flow rate settings of cruise and sea level takeoff have too high a droplet density, completely covering the slide in 0.002 secs. This difficulty in capturing high density liquid spray particles is one of the fundamental drawbacks to the slide impaction technique.



IMPACTOR SLIDE APPARATUS

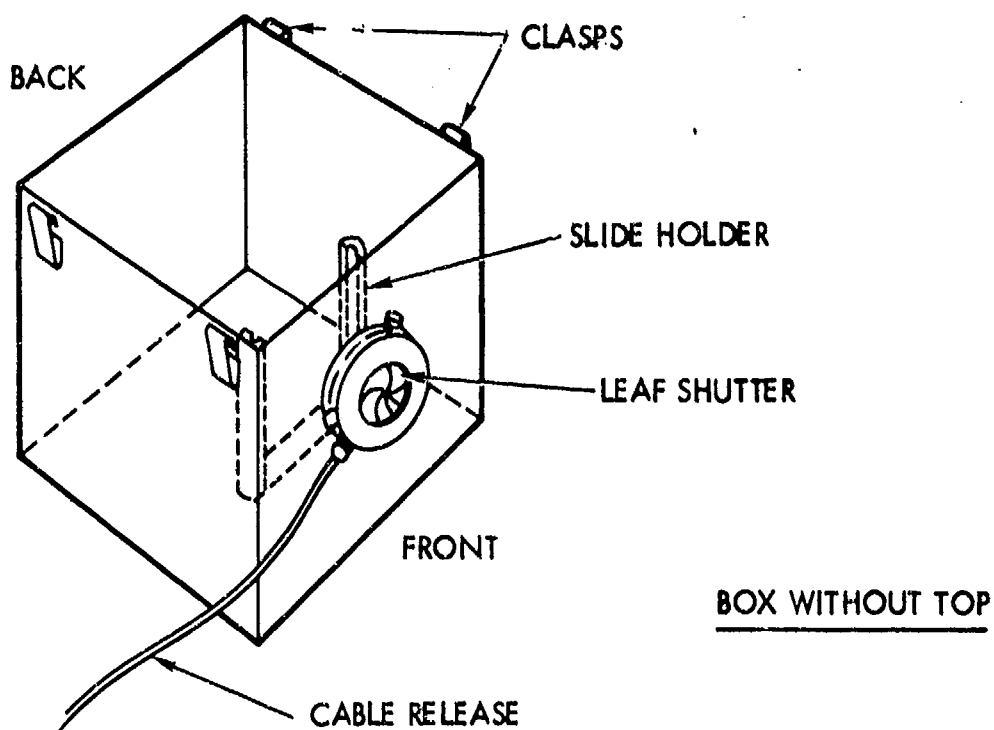


Figure 30. Droplet collection apparatus.

To obtain a droplet size distribution measurement of the entire nozzle spray cone, samples need to be taken across one side of the spray cone. For a preliminary test, 4 samples were taken at a distance of 7.5 cm from the nozzle, starting at the centerline and moving 3 cm outward perpendicular to the spray centerline for each different slide. Four photographs were made of different portions of each slide using a microscope. An example of one photograph is given in figure 31. The inner sides of the darkened crater are measured and compared with a scale photographed at the same magnification (figure 32). This crater is formed upon initial impact of the drop and has no significant change in size for droplets of the same size impacting at different velocities¹⁴. The grainy circular area surrounding the black crater edge differs in diameter with the impact velocity and is caused by the droplet splashing over the crater edge. Once the photographs have been counted, the impression coefficient (ratio of droplet diameter to impression diameter) must be determined. Stoker¹⁴ suggests that this coefficient is a function of the Weber number and is of the form $I = .77(We)^2$. To use this equation, an estimate of the droplet velocity must be known. As an alternative, May¹⁵ suggests that multiplying factors of 0.75 for impressions in the 10-15 μm range, 0.8 for the 15 to 20 μm range and 0.86 for the 20 to 250 μm range are good approximations. For the present results the latter method was used.

Some estimate of the accuracy of the final count versus the number of droplets counted must be included in the results. Azzopardi⁷ reports that within the 95% confidence limits, for a sample of 500 drops the accuracy is $\pm 17\%$. For the preliminary study 194 droplets were actually counted. Some of these droplets were then counted two or four times (double or quadruple counting weight) to account for different exposure time. For example, while drops on slides exposed for 0.008 second receive a weighting of 1, those exposed for 0.002 seconds receive a quadruple weight. This allows variation in exposure

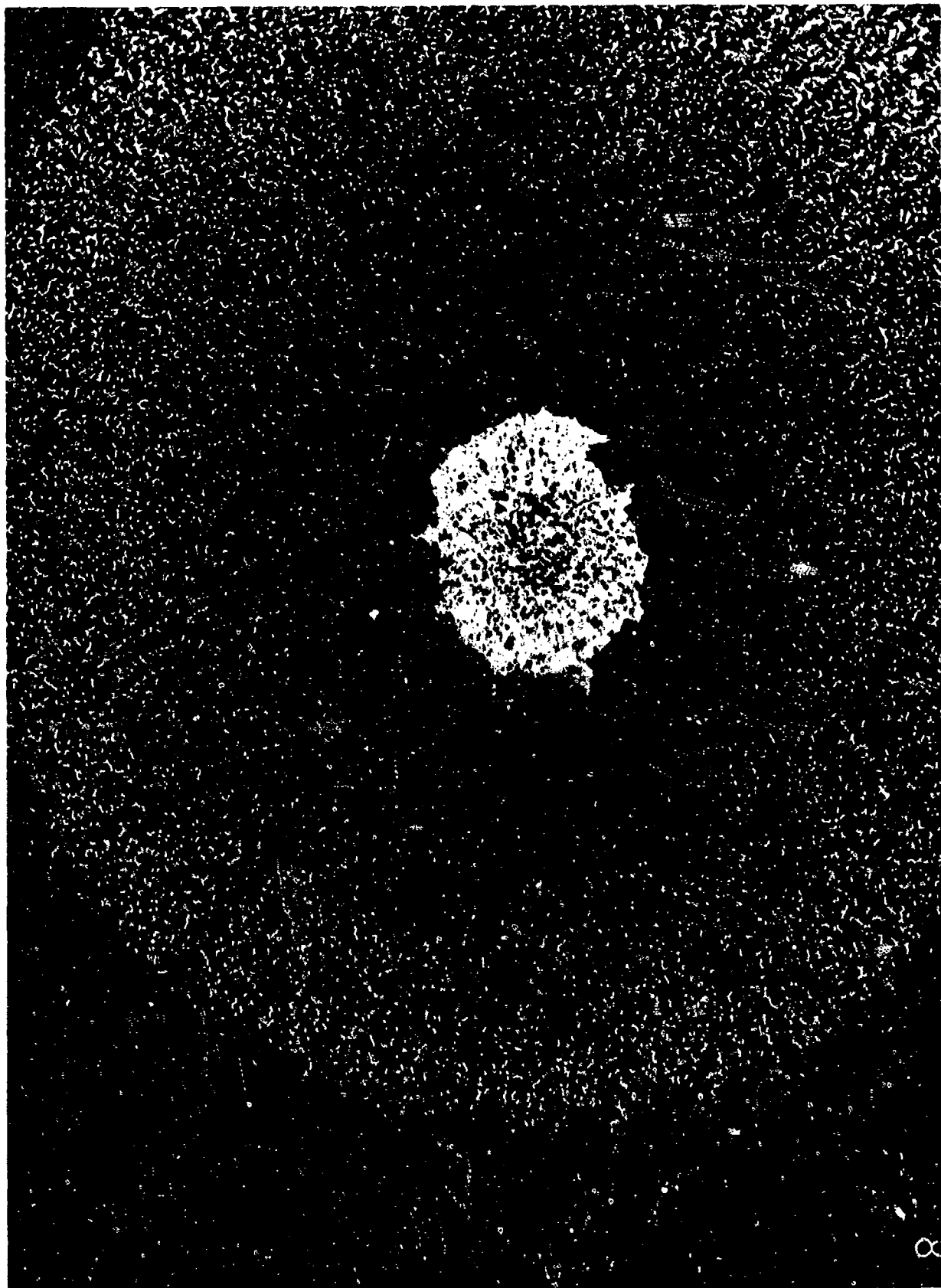


Figure 31. Photograph of droplet impression on coated glass slide (see fig. 44 for scale).

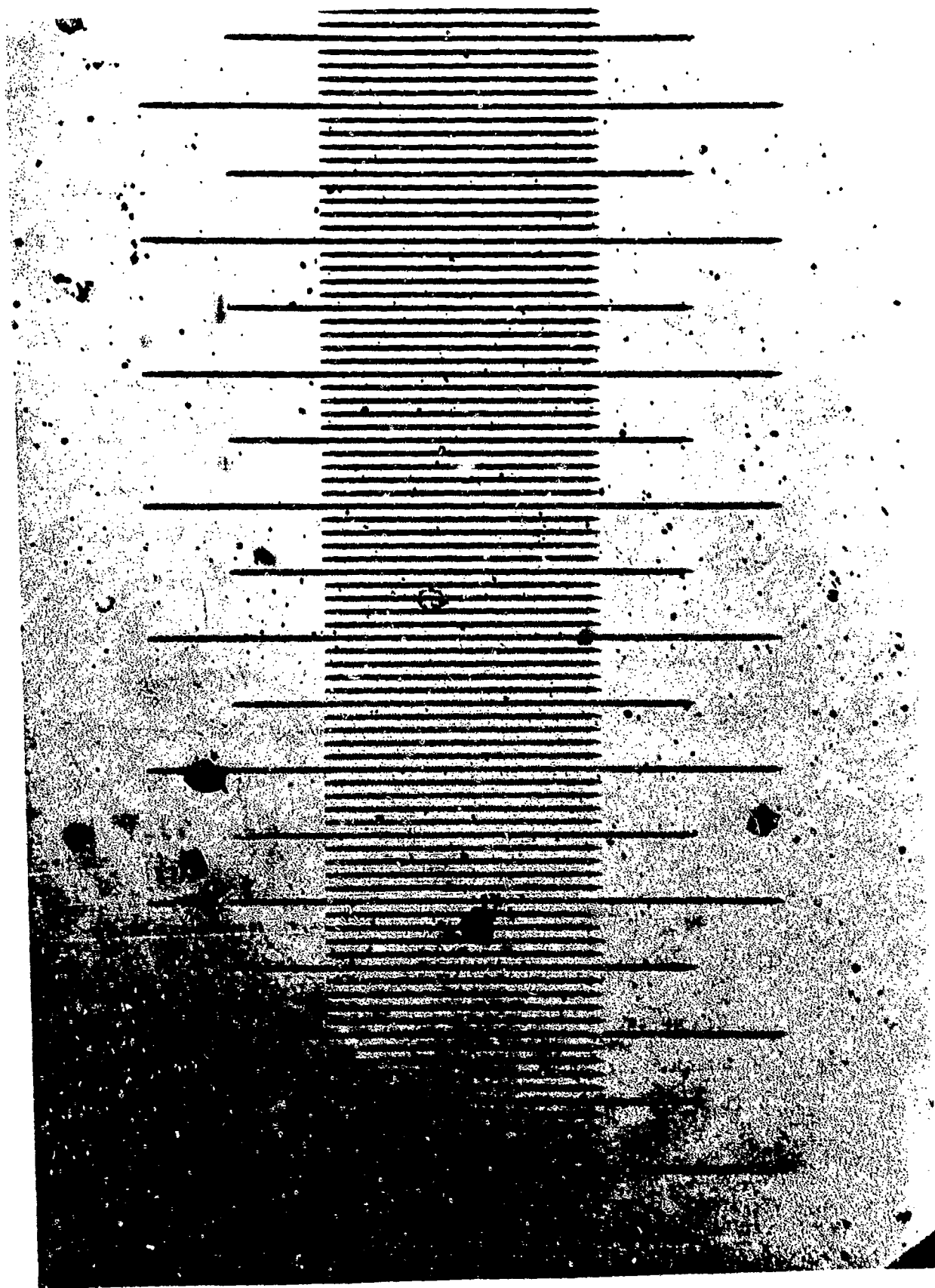


Figure 32. Photograph of rule used to scale impression photos (smallest division spacing is 10 μ m).

time to accommodate sprays of varying density without skewing results in favor of low density areas which were sampled over longer intervals. Thus, 310 droplets were available for analysis. One droplet was discarded as it was far larger than the distribution range of 0 to 200 μm , leaving 306 droplets.

Preliminary results show that the Sauter mean diameter is 83 μm and the mean is 28 μm . The distribution is shown in figure 33. This curve is typical of droplet size distributions observed with this type of fuel nozzle⁶. Also shown is the size distribution obtained using the techniques of section 5.6 with Jet A for the same location downstream of the nozzle and flow conditions.

In comparing the results from the two different counting techniques one should note that the image processing technique has 1078 droplets while the impactor slide technique has 306. The two graphs are normalized to the total count in each experiment. While both have similar shapes, the two plots differ in exact location of the peak and in the mean and Sauter mean diameters. For the image processing results the peak is located in the range of 10-15 μm , with a mean value of 17.3 μm and a Sauter mean diameter of 32.4 μm . These calculations and the graph of characteristic diameters use the same type of data as the graphs in section 5.6 and, thus, have similar uncertainties. The impactor slide graph has a peak at 25-30 μm , a mean of 28.2 μm and a Sauter mean diameter of 83.6 μm . The larger values of these parameters probably are due to the smaller total count of droplets with a disproportionate count of larger droplets. Notice that in the 1078 droplets used in the image processing study, no droplets were observed in the 100-150 μm range, while in the impactor slide study approximately 10% of the droplets were counted in this range. With further studies, counting more droplets and eliminating droplet selection biases in the counting should reduce differences in the quantitative comparison of results from the two methods. Measurements by

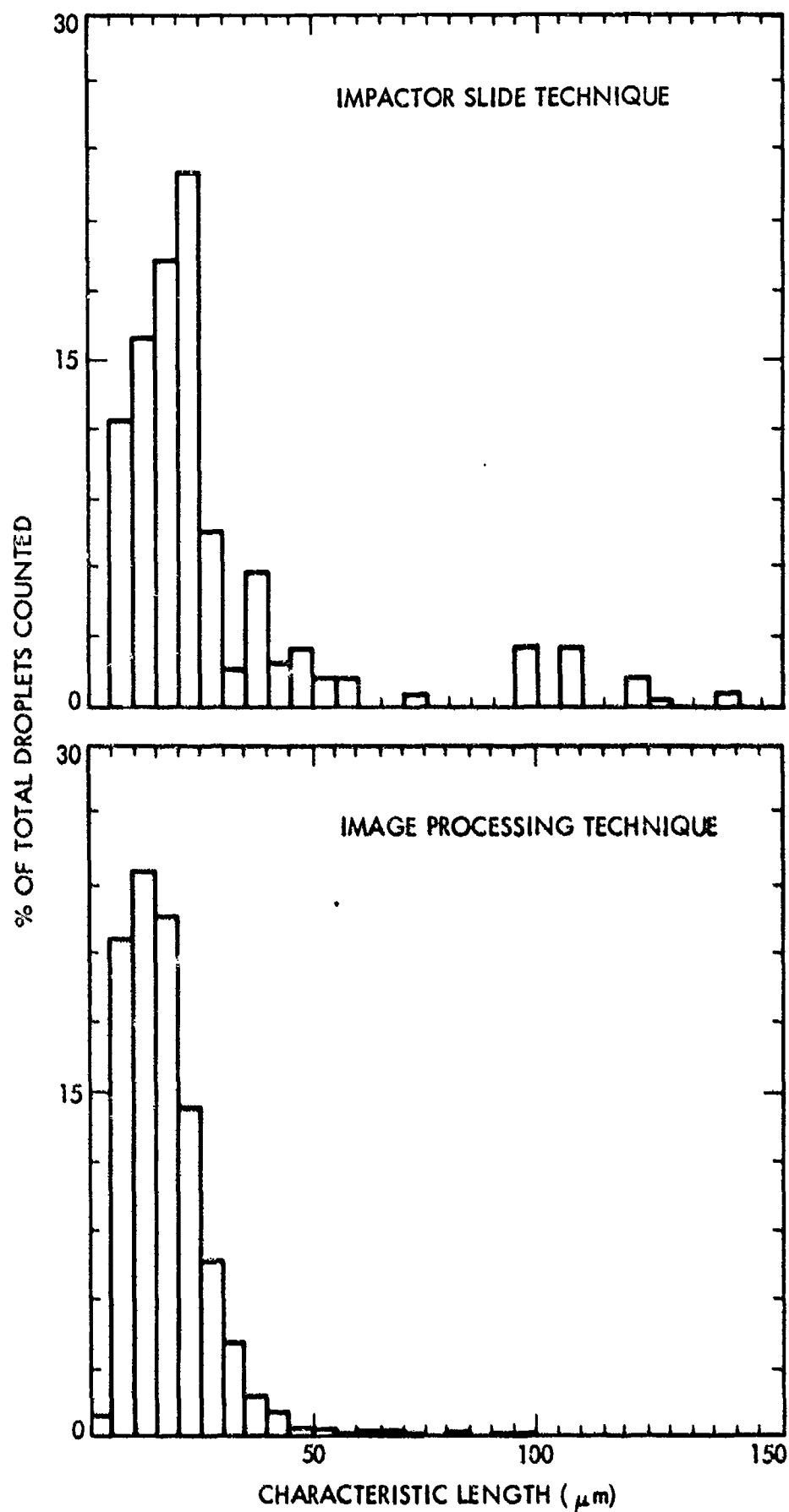


Figure 33. Results of slide impaction and imaging measurement of fuel spray droplets.

Fiorentino et al³ were carried out with the same type of nozzle and the same flow conditions (idle flow rate) using Jet A fuel. Using a Malvern particle sizing device based on scattering of a laser light, they could not obtain a drop size histogram. However, they obtained an SMD value of 33 μm , in agreement with our results from automated photograph analysis within $\pm 2\%$.

VI. EXPERIMENTAL RESULTS

6.1 Flammability Measurements

The experimental parameters that are likely to be important to the aerodynamics of fuel atomization and droplet vaporization in the wing shear experiments include:

- Airspeed
- Fuel mass flow rate
- Fuel orifice size and shape
- Fuel temperature
- Polymer concentration
- Free stream turbulence
- Fuel preshearing

The aerodynamic forces are a direct function of airspeed. The relative fuel/air mass flow ratio ultimately affects the vapor concentration. The orifice size in combination with the fuel mass flow allows the speed and shearing rate of the liquid jet to be varied independently. Besides increasing the fuel vapor pressure, increased fuel temperature decreases the critical shearing rate necessary for gellations⁴¹. Both effects increase flammability. Polymer concentration, of course, determines the non-Newtonian characteristics of the fuel. Free stream turbulence is important to droplet vaporization and heat transfer.

Of these parameters, polymer concentration, airspeed, and fuel temperature, in that order, seem to determine the fire protection of the modified fuel in large scale wing shear experiments⁵. One eventual aim of the program is the comparison and correlation of flammability results with those of the Lakehurst aircraft crash tests and the FAA large scale wing shear facility. Since tests were performed with the larger facilities over a range of FM-9

concentrations, a similar approach was taken for the present work. Additionally the goal of addressing the size scaling issue requires parametric variation of several parameters in order to attempt to preserve similarity. For example, the Reynolds number, $LU\rho/\eta$, where L is the length scale, U the velocity, ρ the fluid density, and η the viscosity, may be held constant while L and U decrease, by substituting fluids of lower η or higher density. Similarly, it may be necessary to alter the characteristic shearing rate of the fluid for rapid onset of shear thickening. The most reliable way to vary this parameter is through FM-9 concentration variation. Since the present study is concerned with determining the range of validity of those observations, secondary parameters such as fuel mass flow and shearing rate have also been emphasized. The objective has been to make precise enough flammability measurements that the effects of many of these parameters can be observed, and to determine under what circumstances they become important.

Most of these parameters affect combustion directly through effects on e.g. spray density and convective heat transfer, as well as the antimisting performance of the fuel. In order to distinguish between the two, the flammability measurements were combined with image processing. Analysis of spray photographs was undertaken to measure only the antimisting performance. The matrix of wing shear operating conditions is shown in figure 34. The nominal airspeeds were 60, 80, and 100 m/s; the nominal fuel flow rates were 0.4, 0.6, and 0.8 kg/s; and the FM-9 polymer concentrations were 0.20, 0.25, and 0.30 %. The operating matrix was intended to bracket pass/fail conditions at all three polymer concentrations. The jet breakup and fuel spray were photographed at each point in the matrix. The flammability measurements excluded operating conditions where fuel adhering to the walls of the test cell caught fire within the first 3 or 4 seconds. The nominal operating conditions could not be

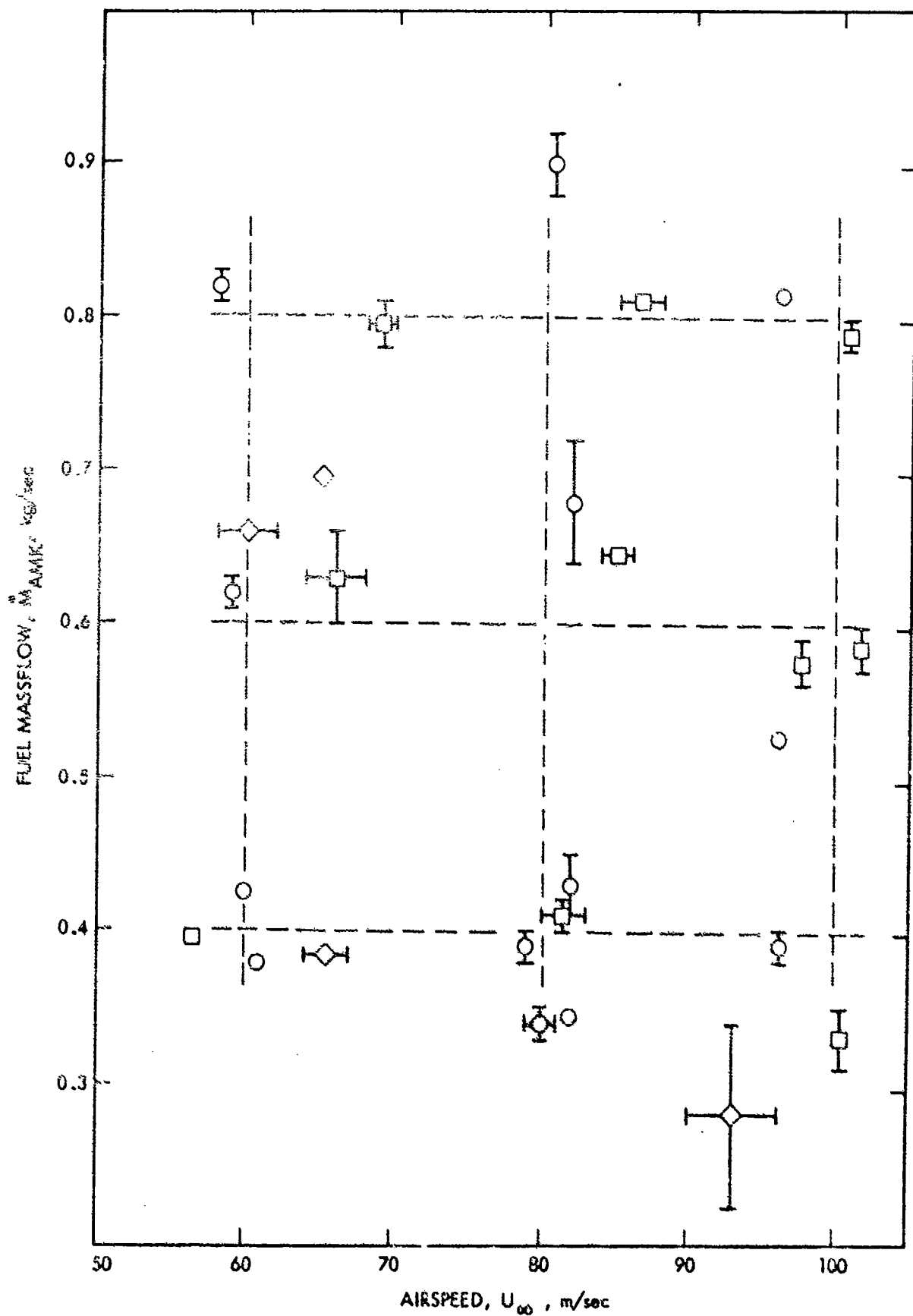


Figure 34. Matrix of wing shear operating conditions. \circ 0.30% FM-9, .25% FM-9; \square .20% FM-9; --- nominal matrix.

achieved with very great accuracy (fig. 34). Although the performance of the wing shear facility was disappointing in this regard, there was enough redundancy that any trends should be apparent. Spray photographs and flammability measurements were also combined with the FCTA, which was operated at an air pressure of 6.1 atm (75 m/s peak airspeed), a speed control setting of 900 (21 g/s fuel flow rate), and polymer concentrations of 0, 0.20%, 0.25%, and 0.30%.

The image processing results are discussed in Section 6.2. The wing shear flammability measurements are summarized in figures 35 through 37. In each case, flammability was measured with an array of 4 thermocouples distributed along the blower centerline. In all of these wing shear apparatuses, including the FCTA, combustion takes place in the mixing layer of an air jet. In jet flows the distribution of mean turbulence quantities generally scales with the jet diameter⁴². For that reason, probe positions have been scaled with the exit diameter (or side dimension for square cross-sections) of the contraction section.

Flammability of 0.3% FM-9 is depicted in figure 35. Flammability increased with airspeed, but appeared to be relatively insensitive to fuel flow rate. Pass/fail is indicated by a P or F for each temperature distribution. In these cases a pass is defined as a test where the combustion temperatures stabilize and there is no wall fire. A fail is a test where the temperatures increased with time until the walls caught fire. In such cases temperatures represent peak values before the fuel flow was interrupted. At polymer concentrations of 0.25% and 0.20% FM-9 (figures 36 and 37) flammability increased with both airspeed and fuel flow rate.

In figures 35-37 failures were generally characterized by temperatures that increased with downstream distance. The average temperature slopes are

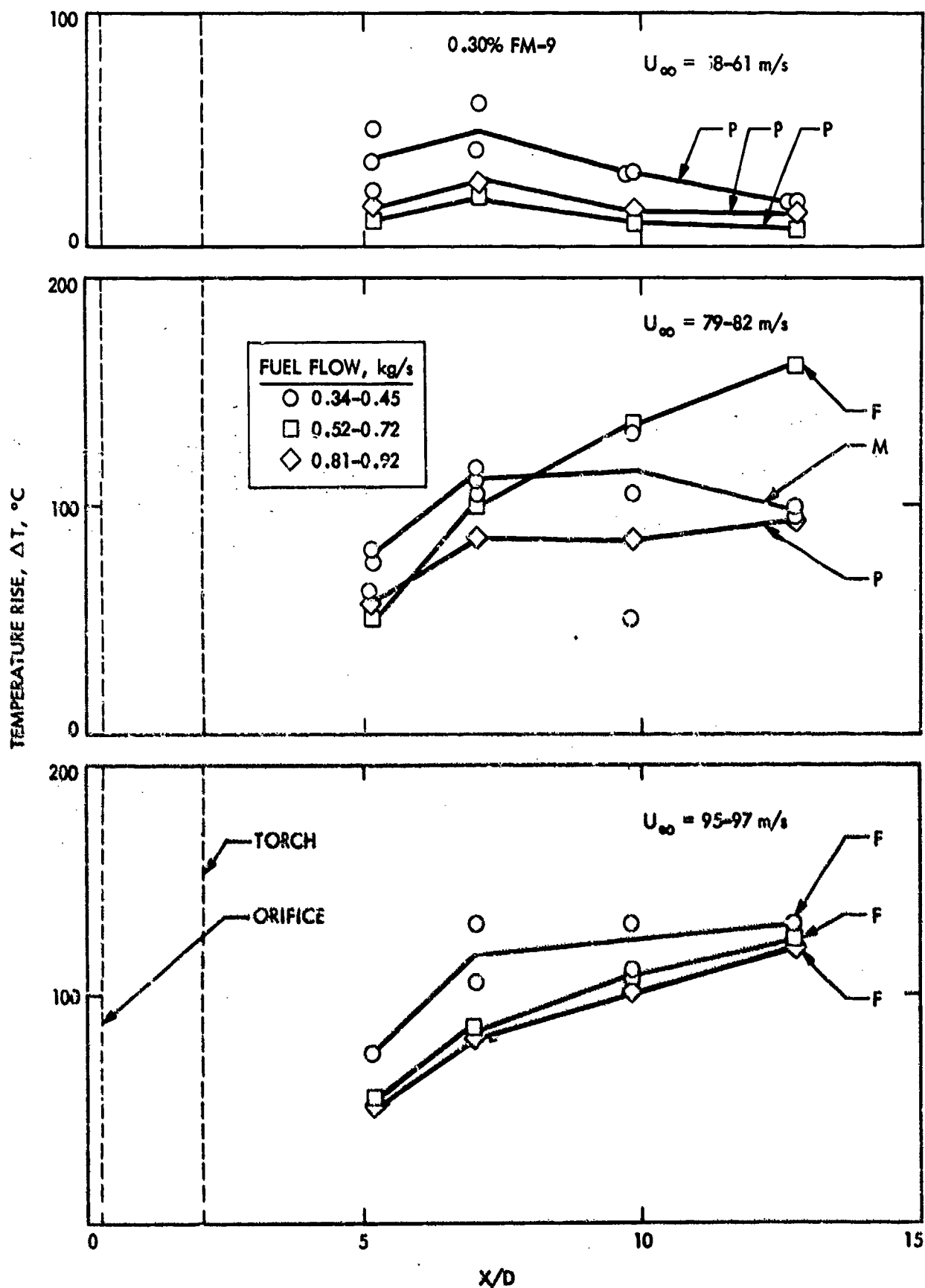


Figure 35. Wing shear combustion temperature vs. downstream distance for 0.30% FM-9. Distance is normalized by exit dimension of contraction section. Letters F, M, P refer to fail, marginal, and pass (see text for details of pass/fail criterion).

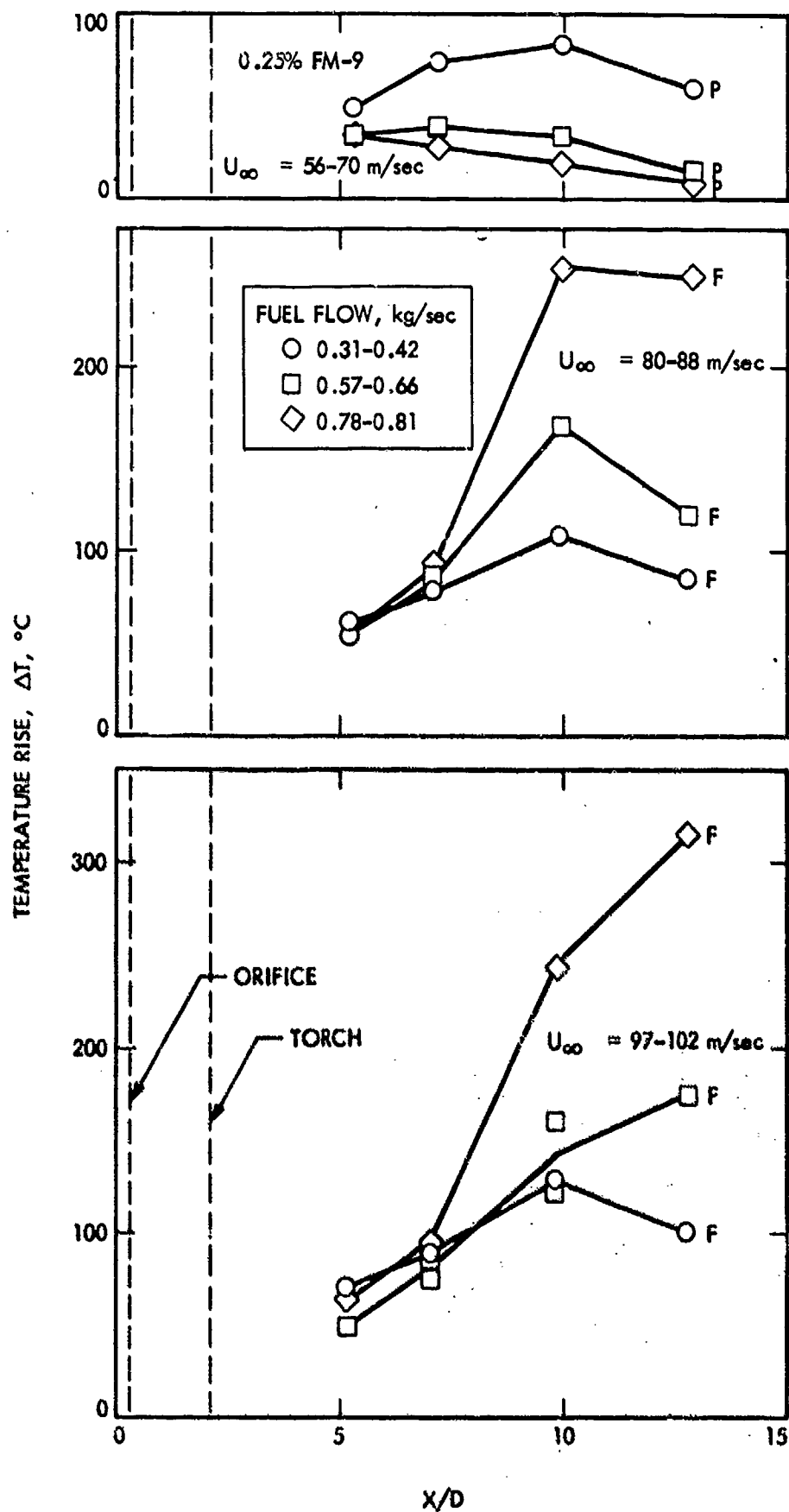


Figure 36. Wing shear combustion temperature vs. downstream distance for 0.25% FM-9.

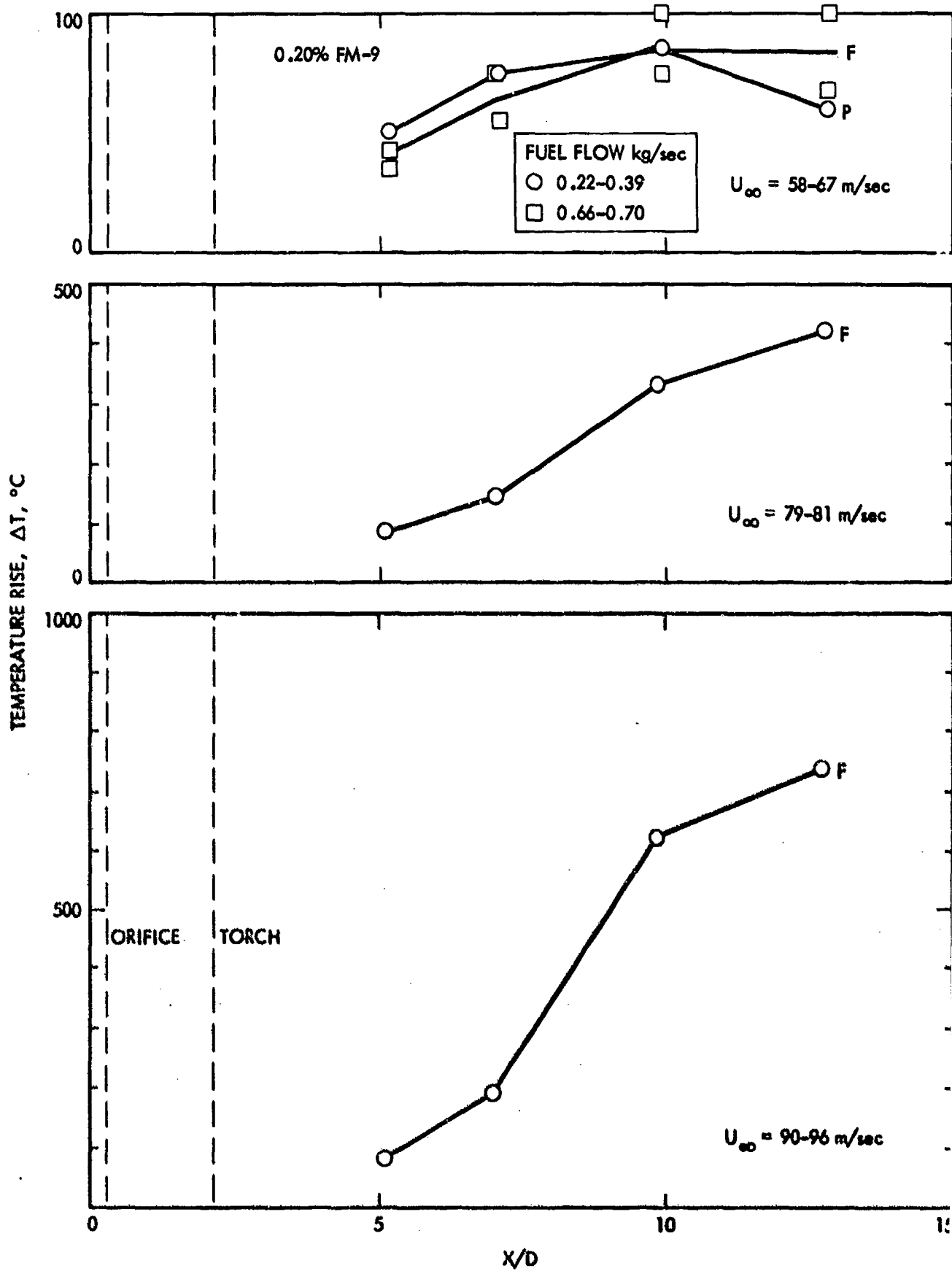


Figure 37. Wing shear combustion temperatures vs. downstream distance for 0.20% FM-9.

shown in figure 38 as a function of airspeed for all three polymer concentrations and for the various fuel flow rates. The pass/fail notations shown are those determined by wall ignition observations as described earlier. The failures are generally associated with large positive temperature slopes; the temperature slopes generally increase with airspeed and fuel flow rate.

Temperature measurements with the FCTA are shown in figure 39. A single thermocouple was located 10 mixing tube diameters downstream of the torch, on the centerline. The polymer concentration was 0.3% FM-9, and three different fuel mass flows were tested. The combustion temperatures increased with both airspeed and fuel mass flow. Peak airspeeds are used as they depend solely on plenum initial conditions and hence are more easily determined. They are intended only to allow comparison among other FCTA tests performed identically.

6.1.1 Fuel and Air Mass Flow Effects

In order to express the measured temperature rise in the combustion region as a measure of the extent of combustion a reduced temperature, θ , is introduced (see Appendix 1 for a more complete discussion):

$$\theta = \frac{\dot{M}_{air} c_p T}{\dot{M}_{fuel} q_c} \quad (6.1-1)$$

where \dot{M}_{air} = mass flow rate of air

\dot{M}_{fuel} = mass flow rate of fuel

c_p = specific heat of air ($\approx 10^3$ joule/kgvK)

q_c = enthalpy of combustion of fuel ($\approx 4.32 \times 10^7$ joule/kg for Jet A) in air

T = Measured temperature rise in the combustion region

In effect, θ is the fraction of the enthalpy of combustion of the entire fuel mass in air that is actually released to the gases. If the fuel is completely burned then $\theta=1$. In practice, θ is a lower bound estimate of the ex-

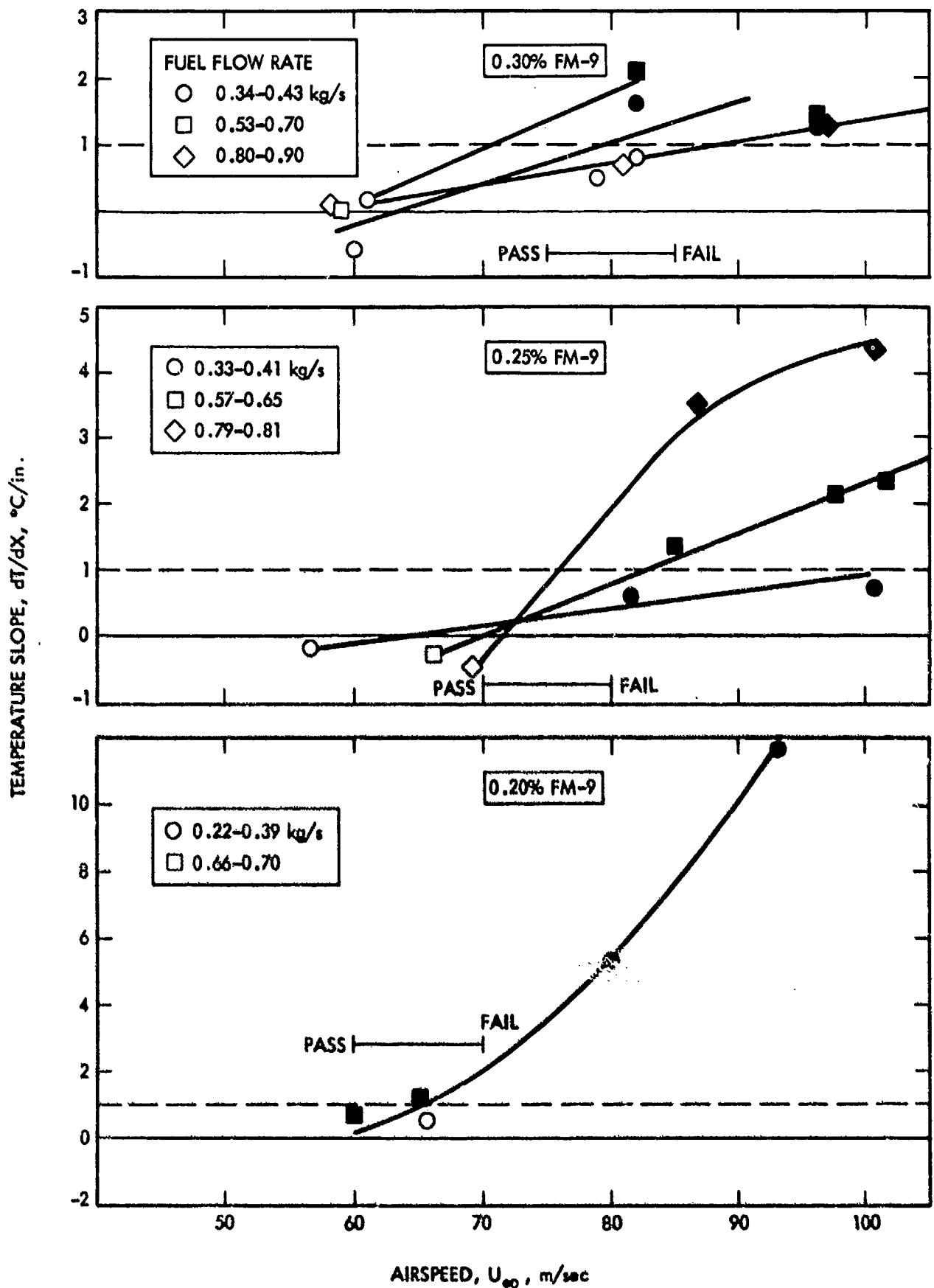


Figure 38. Average rates of change of temperatures with downstream distance as a function of airspeed. Solid symbols denote fails (a) 0.30% FM-9, (b) 0.25% FM-9 (c) 0.20% FM-9 (see text for discussion of pass/fail criterion).

tent of combustion because of radiation heat losses and because of entrainment of cooler air. This concept is tested in figure 40 by applying it to a set of the Jet A measurements where the apparent flammability was high. The fuel/air massflow ratio was 0.04, which is below the stoichiometric ratio. The reduced temperature reached a peak value of about 0.6, which is consistent with good combustion efficiency. At lower fuel/air ratios, reduced temperatures as high as 0.7 were measured with Jet A.

The FCTA data of figure 39 are replotted in figure 41 as reduced temperatures. The data collapse suggests that the combustion efficiency (and fire protection) was independent of fuel mass flow rate and was mainly sensitive to airspeed. The magnitudes of the reduced temperature indicate that the efficiency was quite low, i.e., good fire protection.

The wing shear data for AMK do not collapse as well. Temperatures measured at $x/D = 12.7$, figures 35-37, are replotted in figure 42 as reduced temperatures against fuel massflow at various polymer concentrations and at fixed airspeeds. The variation of θ with fuel mass flow suggests that the mass flow, as well as the airspeed, influenced flammability. At high FM-9 concentrations θ decreased with fuel flow, and at lower concentrations the trend seems to depend on airspeed.

The reduced temperatures measured with the wing shear apparatus are consistent in magnitude with those measured with the FCTA, as demonstrated in figure 43. The range of fuel/air massflow ratios, 0.1-0.6, is reasonably large, and although the data scatter is large, the two facilities give comparable results. Based on this measure of combustion efficiency the two facilities yield comparable measures of fuel flammability.

6.1.2 Orifice Effects

The effect of orifice dimension on fire protection was investigated.

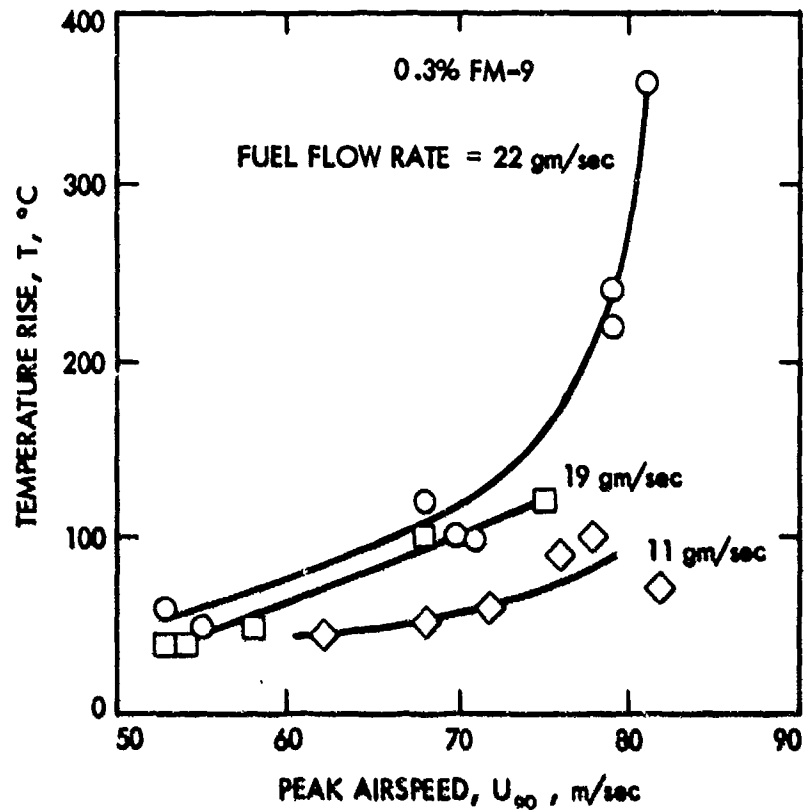


Figure 39. Combustion temperatures for 0.30% FM-9 vs. peak airspeed measured with FCTA. Thermocouple located 25 cm downstream from torch ($x/D = 10$).

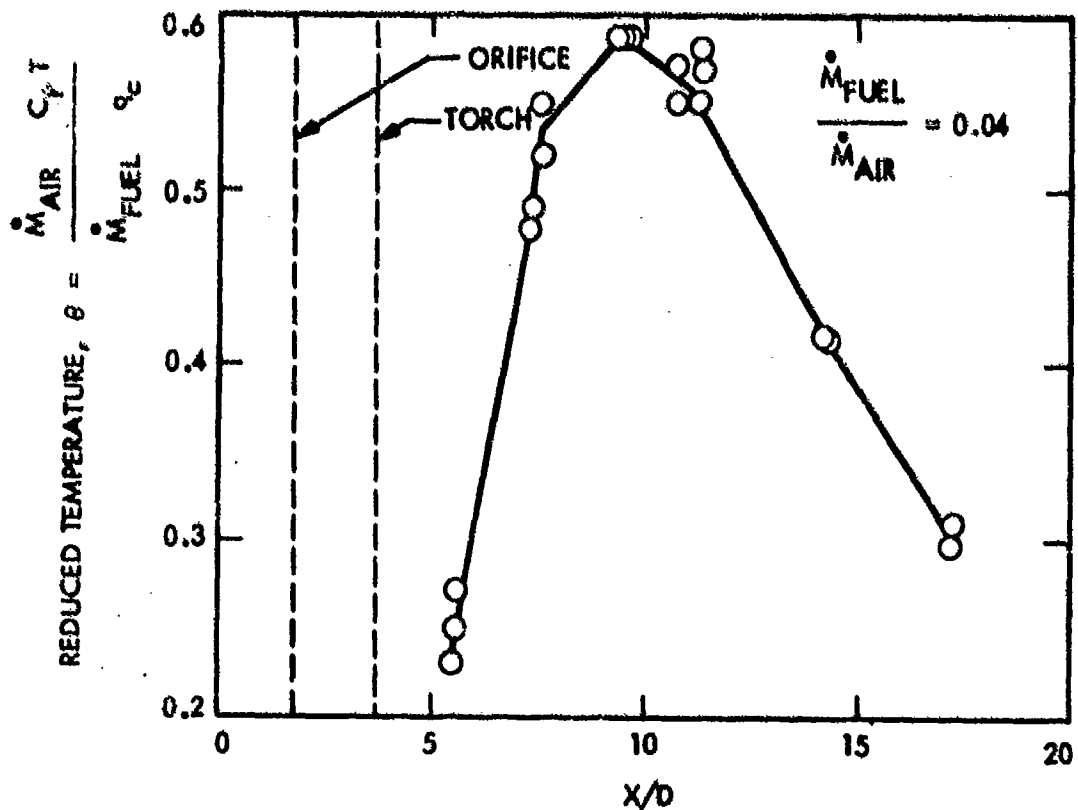


Figure 40. Reduced wing shear temperature vs. downstream distance for Jet A.

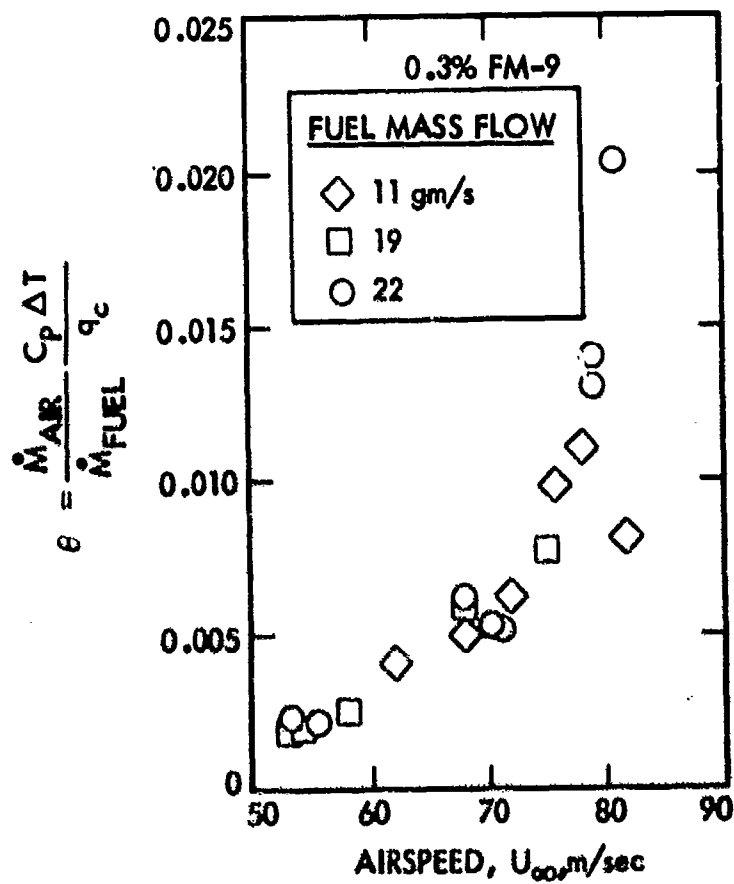


Figure 41. Reduced FCTA temperature vs. airspeed for 0.30% FM-9.

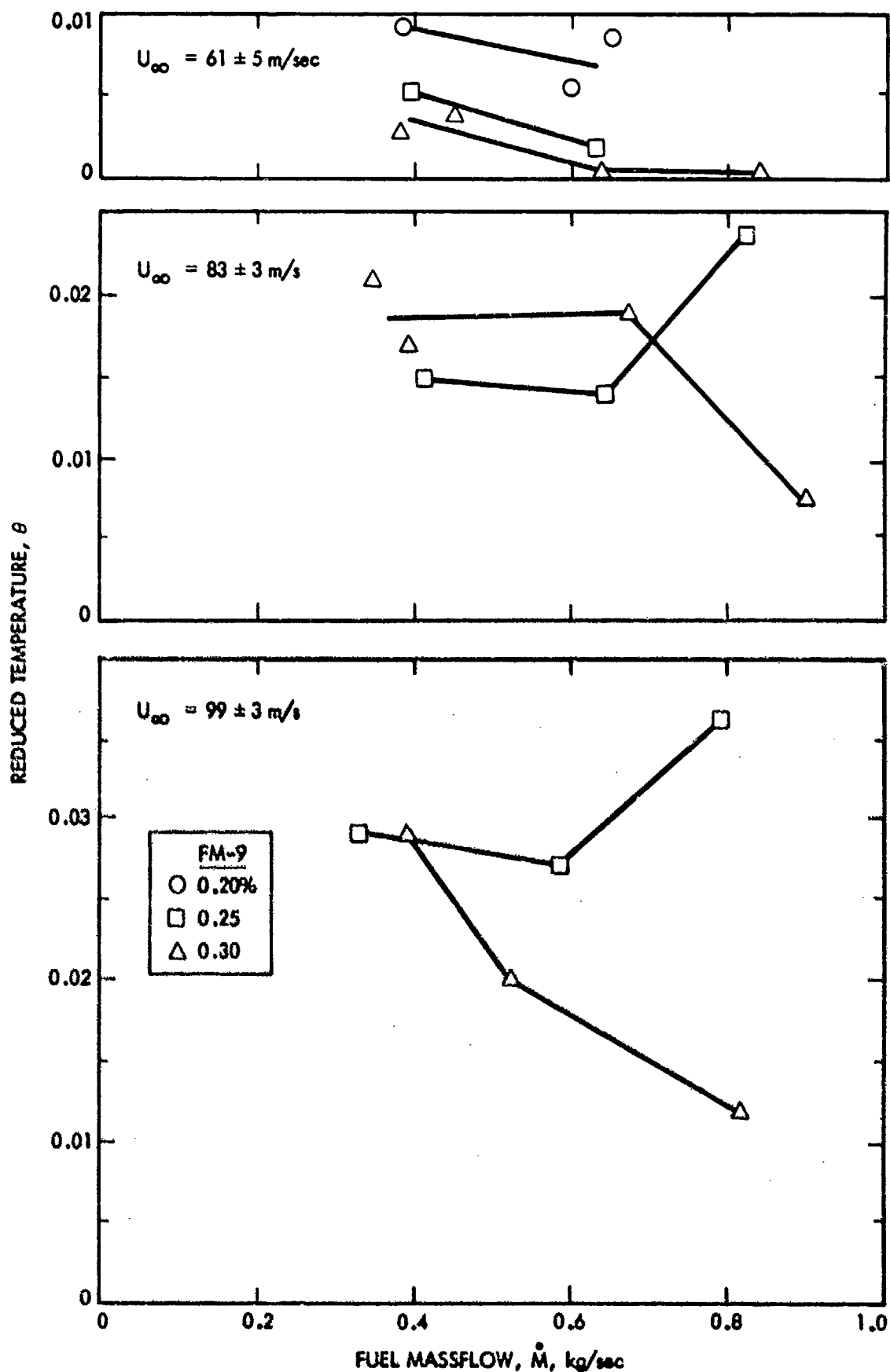


Figure 42. Reduced wing shear temperature vs. fuel massflow. Thermocouple located at $x/d = 12.7$. (a) Airspeed 61 ± 5 m/s (b) Airspeed 83 m/s (c) Airspeed 99 ± 3 m/s.

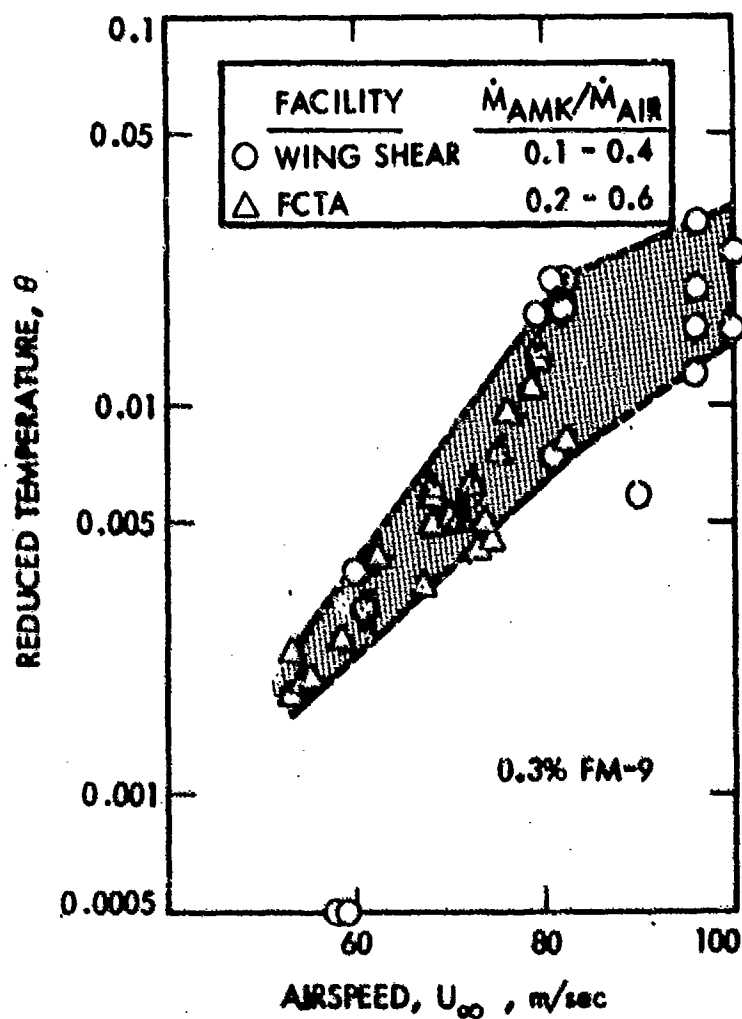


Figure 43. Envelope of reduced temperatures vs. airspeed for wing shear and FCTA, using 0.30% FM-9. Thermocouple locations were 10 mixing tube diameters behind torch (FCTA) and 10.6 blower diameters behind torch (wing shear).

Specifically, the effects of orifice shearing rate and jet Reynolds number were examined.

When the modified fuel is subjected to large shearing stresses shear thickening occurs. The shear thickening is a time-dependent phenomenon and the rate of gelation depends on the shearing rate. Typical shear thickening histories for 0.30% FM-9 at different shearing rates are shown in figure 44 (from ref. 41). For any flow configuration there is a critical shearing rate beyond which gelation occurs rapidly with respect to the characteristic time scale of the flow. In general, the critical shear rate depends on the polymer concentration and the temperature.

For a given geometry, the aerodynamic shearing of the fuel by the airstream is mainly a function of airspeed. Shearing of the fuel by the orifice is independent of the airspeed, and for viscous flows the shearing rate through the orifice is roughly

$$\dot{\gamma} = 8 U/d \quad (6.1-2)$$

where $U = \dot{M}/\rho_s =$ area average velocity, and $d =$ orifice diameter. The effect of orifice shearing rate on combustion efficiency is shown in figure 45. Reduced temperatures are plotted against shearing rate for fixed airspeeds for a polymer concentration of 0.3%. Three different orifice sizes were tested. They were selected to provide shearing rates that encompass the critical rate, $\dot{\gamma}_c$. According to Peng and Landel⁴¹, the critical shearing rate in well defined flows for FM-9 at 24°C is $3.1 \times 10^5 \text{ s}^{-1}$ and for a polymer concentration of 0.3%. These rates are indicated in figure 45 by dashed lines. The combustion efficiency may have a slight minimum near the critical shearing rate. In any case, orifice shear did not have a significant effect on flammability in these experiments. This is not very surprising because the aerodynamic shearing rates caused by the airstream are always much larger.

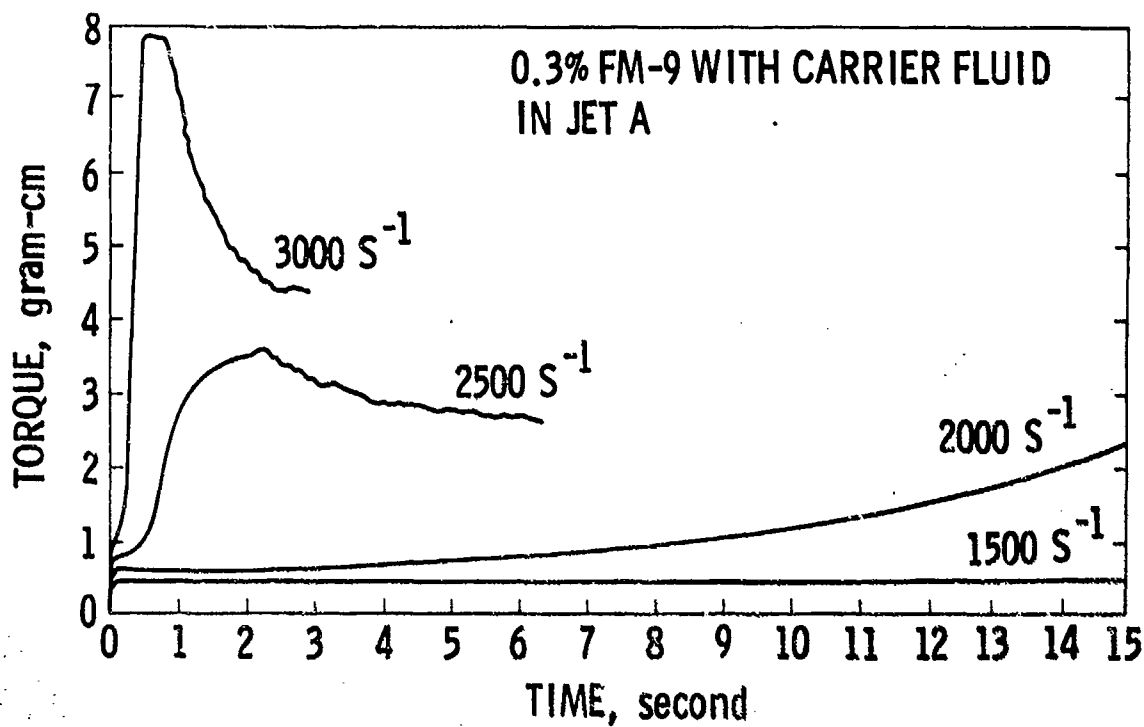


Figure 44. Time dependent behavior of modified fuel at various shearing rates, 23.9°C (from ref. 41).

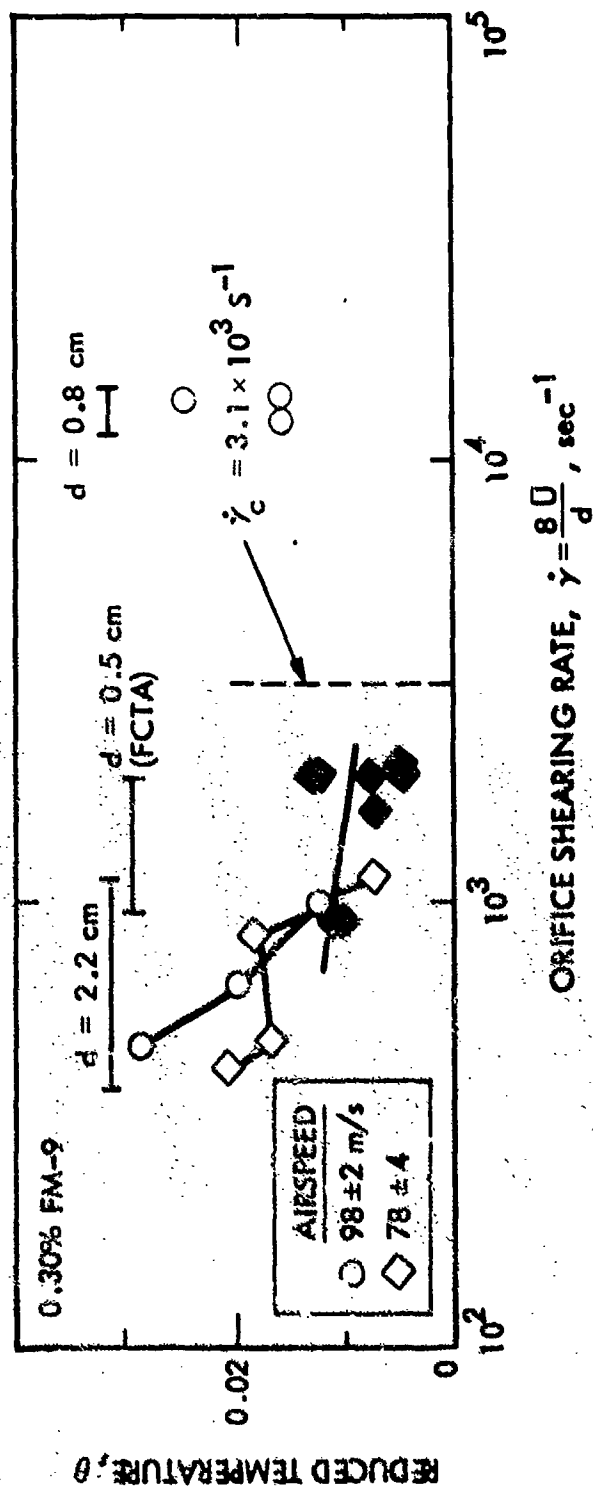


Figure 45. Reduced temperature vs. shearing rates for various orifice diameters. The critical shearing rate is shown by dashed line. Open figures are mini wing shear data. Closed figures are FCTA data.

The effect of jet Reynolds number is examined in figure 46. The Reynolds number, based on orifice exit area and apparent viscosity, is defined by:

$$R_L = \frac{\dot{M}}{\mu_L S} \quad (6.1-3)$$

where μ_L is the zero shear rate apparent viscosity as measured by a Brookfield viscometer. As shown in figure 46, there was no apparent Reynolds number effect up to a jet Reynolds number of 2.5×10^4 .

6.1.3 Polymer Concentration Effects

Fire protection clearly increases with polymer concentration. Figure 47 is a plot of temperature rise vs. polymer concentration for five experiments involving different FM-9 batches, operating conditions, facilities, and thermocouple locations. In each experiment the temperature rise decreased more or less as a power of polymer concentration.

The polymer concentration was varied by addition of base fuel to the modified fuel (0.3% FM-9). The two components were blended by slow tumbling for at least 15 minutes before testing.

6.1.4 Radiometer Measurements

A major reason for undertaking an experimental program using the JPL mini wing shear facility was that more reliable instrumentation could be installed in it than was possible in the FAA large scale facility. The choice of what specific measurements were to be made remained a subject for investigation. The FCTA used a radiometer and so devices of this type were considered for the JPL wing shear. Thermocouples were also considered and tests were performed to assess the relative merits of the various probes. Two types of radiometers were tested: a narrow angle optical system and an omnidirectional calorimeter similar to that used in the FCTA.

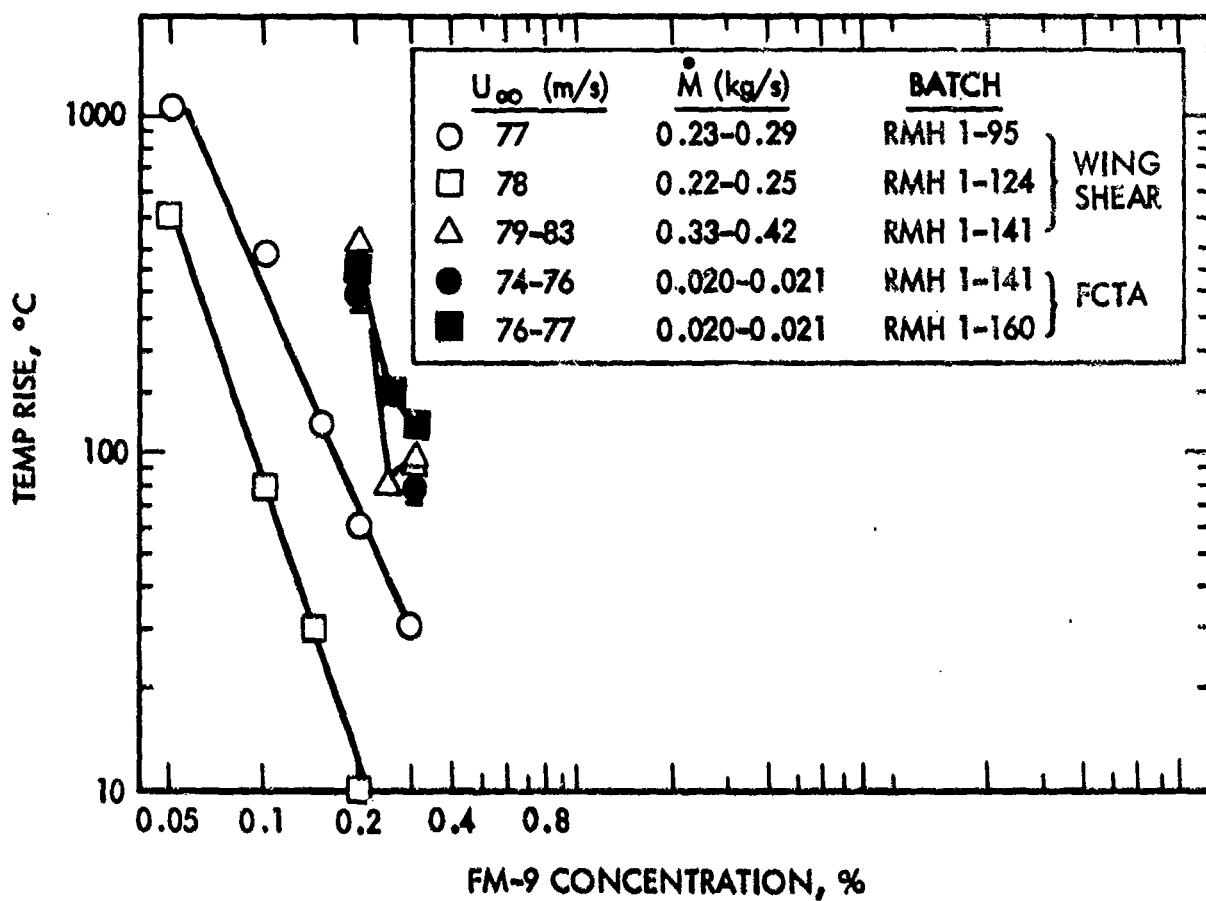


Figure 47. Wing shear and FCTA temperature vs. polymer concentration for various fuel flow rates, airspeeds, and batch numbers. Straight line represents a power law relationship.

In order to insure that the same spatial position was being sampled, the optical radiometer was focused on the thermocouple which was located 7.5 diameters downstream from the blower exit. The field of view of the radiometer was about 3 cm square, whereas the thermocouple junction was 0.8 mm in diameter. Radiation from the thermocouple surface should thus not affect the measurement very much. The fuel orifice and torch were located 1.8 and 3.7 diameters downstream respectively. The radiometer was located approximately 3 meters off-axis. Modified fuels with various polymer concentrations were tested, and radiometer measurements were made simultaneously with temperature measurements. The results appear in figure 48. The radiometer measurements are expressed as equivalent black body temperatures. Although the two sets of measurements show similar trends, the black body temperatures deviate considerably from the thermocouple temperatures. At the highest temperatures the deviations are several hundred degrees, and at the lowest temperatures the relative deviation is large. Since the emissivity of the gas is not constant, it is impossible to calibrate the radiometer.

The calorimeter measures radiant heat from the entire combustion region. It was tested with the array of thermocouples. Unlike the optical radiometer, the calorimeter measurement is a function of distance from the source because the radiant flux obeys the inverse square law. The calorimeter was located 3 meters off-axis, opposite the torch. Calorimeter measurements were taken during the flammability test, using modified fuel with 0.25% FM-9. The calorimeter readings are plotted in figure 49(b) against airspeed for a family of fuel flow rates. The corresponding temperature slopes, replotted from figure 38, are shown for comparison. The trends are consistent between the two sets of data. Operating conditions that produce a large rate of increase of temperature with downstream distance also produce considerable heat radiation.

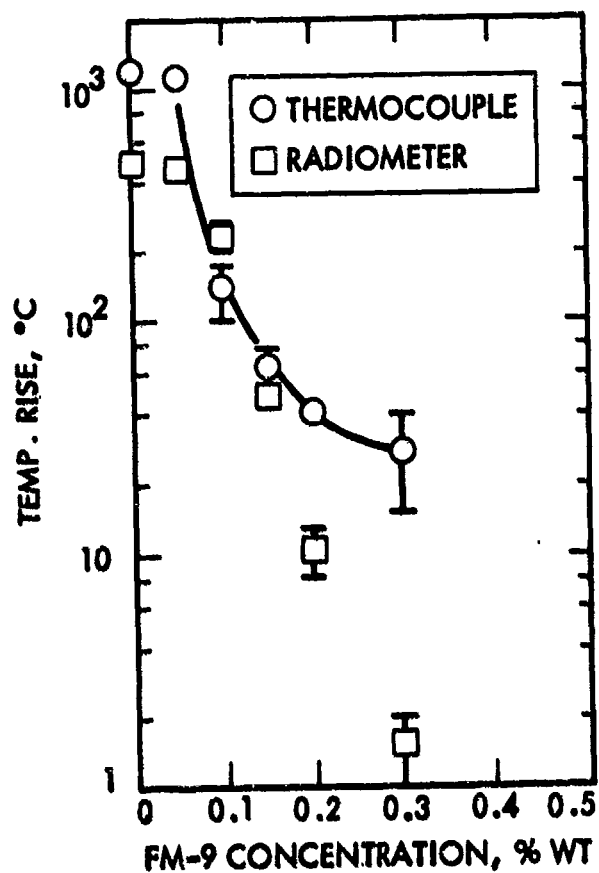


Figure 48. Comparison between thermocouple and radiometer measurements of flammability vs. polymer concentration. The radiometer was focused on the thermocouple and measured equivalent black body temperatures. Airspeed = 77 m s^{-1} .

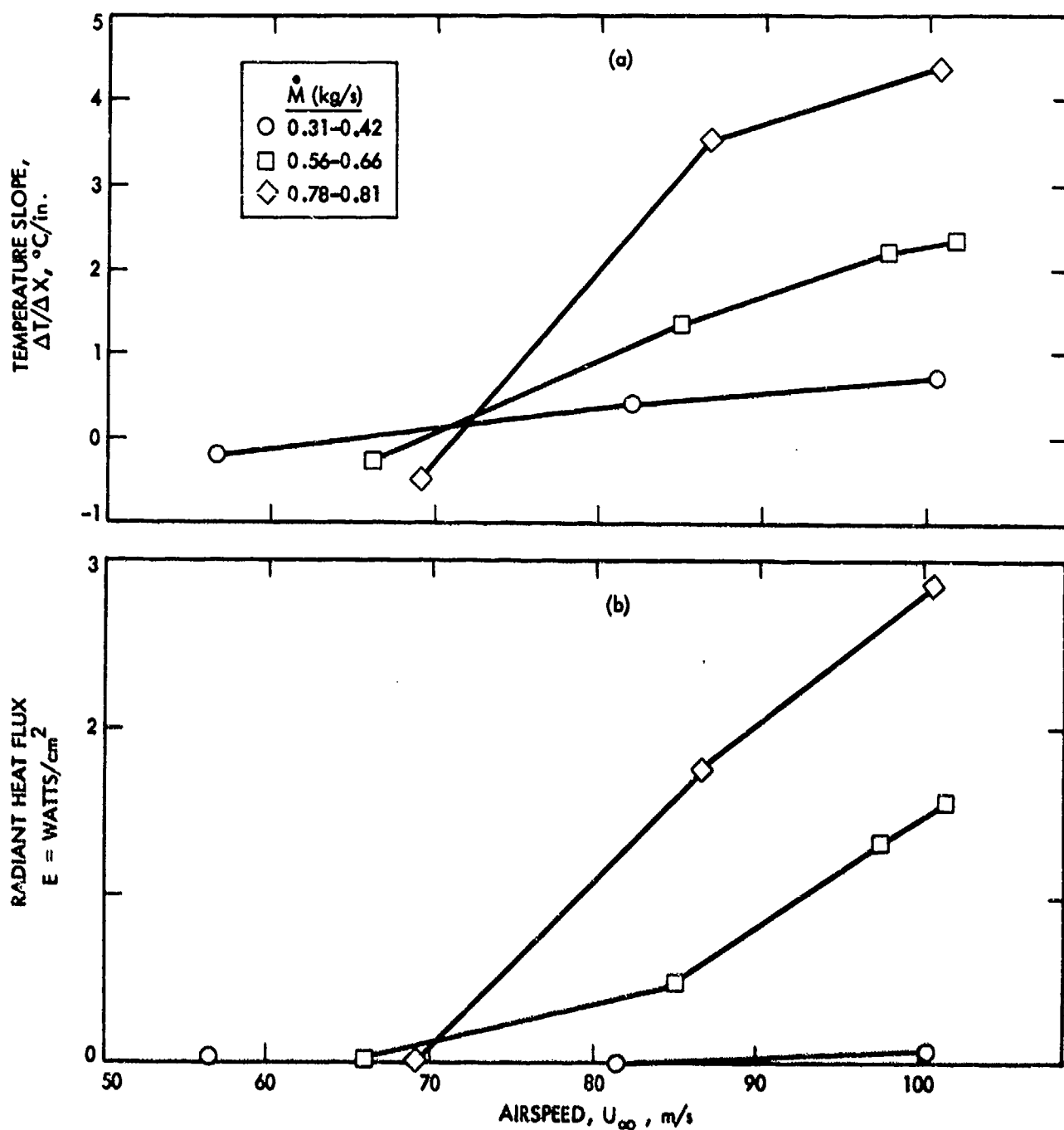


Figure 49. Comparison between thermocouple and radiometric calorimeter, measurements of flammability of 0.25% FM-9 with airspeed and fuel flow rate. (a) Rate of change of temperature with distance, replotted from figure 50; (b) radiant heat flux measured with the calorimeter located 3.0 m off-axis opposite the torch.

Thus the calorimeter should be useful at providing pass/fail information.

The radiant heat flux decreases with distance from the source. If the geometry is assumed to be axisymmetric, then the radiant heating rate, \dot{Q}_R , could in principle be measured by a line array of calorimeters:

$$\dot{Q}_R = 2\pi R \int_{-\infty}^{\infty} E(x,R) dx, \quad (6.1-4)$$

where $E(x,R)$ is the radiant flux measured by a calorimeter located a radial distance, R , from the centerline and a distance x from the blower exit. For a single calorimeter, and if the combustion region is spatially compact, the total heating rate is approximately

$$\dot{Q}_R \approx 4\pi R^2 E(R).$$

Since latent heat is being introduced at the rate $q_c \dot{m}_f$, where q_c is the specific heat content of the fuel, a measure of radiation efficiency, e_R , can be defined

$$e_R = \frac{4\pi R^2 E(R)}{q_c \dot{m}_f} \quad (6.1-5)$$

In effect, e_R is the fraction of the fuel combustion enthalpy that is converted to radiant heat.

In figure 50 calorimeter and thermocouple data are compared in terms of "efficiencies", e_R and θ , which were measured simultaneously. The thermocouple was located at $x/D = 12.7$, and the data are from figure 48. Pass/fail, indicated by a P or F, is based on whether fuel adhering to the walls caught fire. The calorimeter is especially effective in registering pass/fail because it is sensitive to radiation from the walls.

In summary, the imaging radiometer cannot be used for quantitative measurements. The calorimeter is useful when there is radiative heating, and

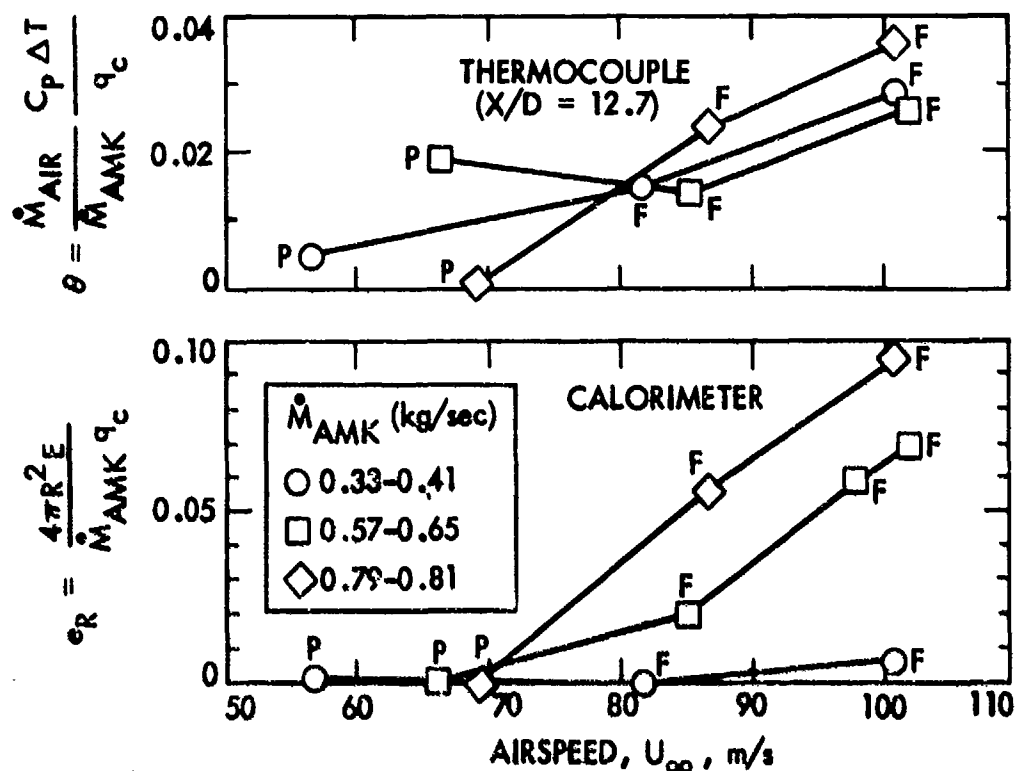


Figure 50. Comparison between estimates of combustion efficiency based on reduced temperatures and reduced radiant flux for 0.25% FM-9. (a) Reduced temperatures measured at $x/d = 12.7$, radiation efficiency defined by eqn (6.1-5). (See text for discussion of pass/fail criterion).

is good as a pass/fail device in a particular environment. Its sensitivity to the details of the radiating surfaces makes it difficult to generalize the measurements, however.

6.1.5 Quality Control and Deterioration Effects

As the program proceeded, problems of flammability test reproducibility became evident. Even though different AMK batches appeared uniform when subjected to cup and filter tests, their flammability was variable to the extent that the parametric variations under investigation were obscured. To determine the extent of this problem, a simple quality control flammability test was devised. The test was to be performed on a routine basis and hence could not practically be carried out in great detail. A simple, single datum figure of merit was required. To achieve this, a simplified, standardized quality control test was devised which could be rapidly carried out using the FCTA. The test procedure used only for these quality control tests is described in Appendix 2.

Results of these quality control tests for February through June of 1981 are shown in figure 51. While the batch to batch repeatability of the cup test was high, the filter ratio changed by 100% between March and May. Similarly, temperature rises measured in the standardized flammability test varied by approximately the same amount.

6.2 Drop Formation and Measurement

As emphasized in Section 5.1, suppression of small droplet formation is believed to be fundamental to AMK's flammability resistance. The physical forces leading to disintegration of liquid drops and jets include unbalanced and fluctuating pressure, inertial and viscous forces on the jet or drop surface⁴³. These are resisted by the jet or drop surface tension, viscous

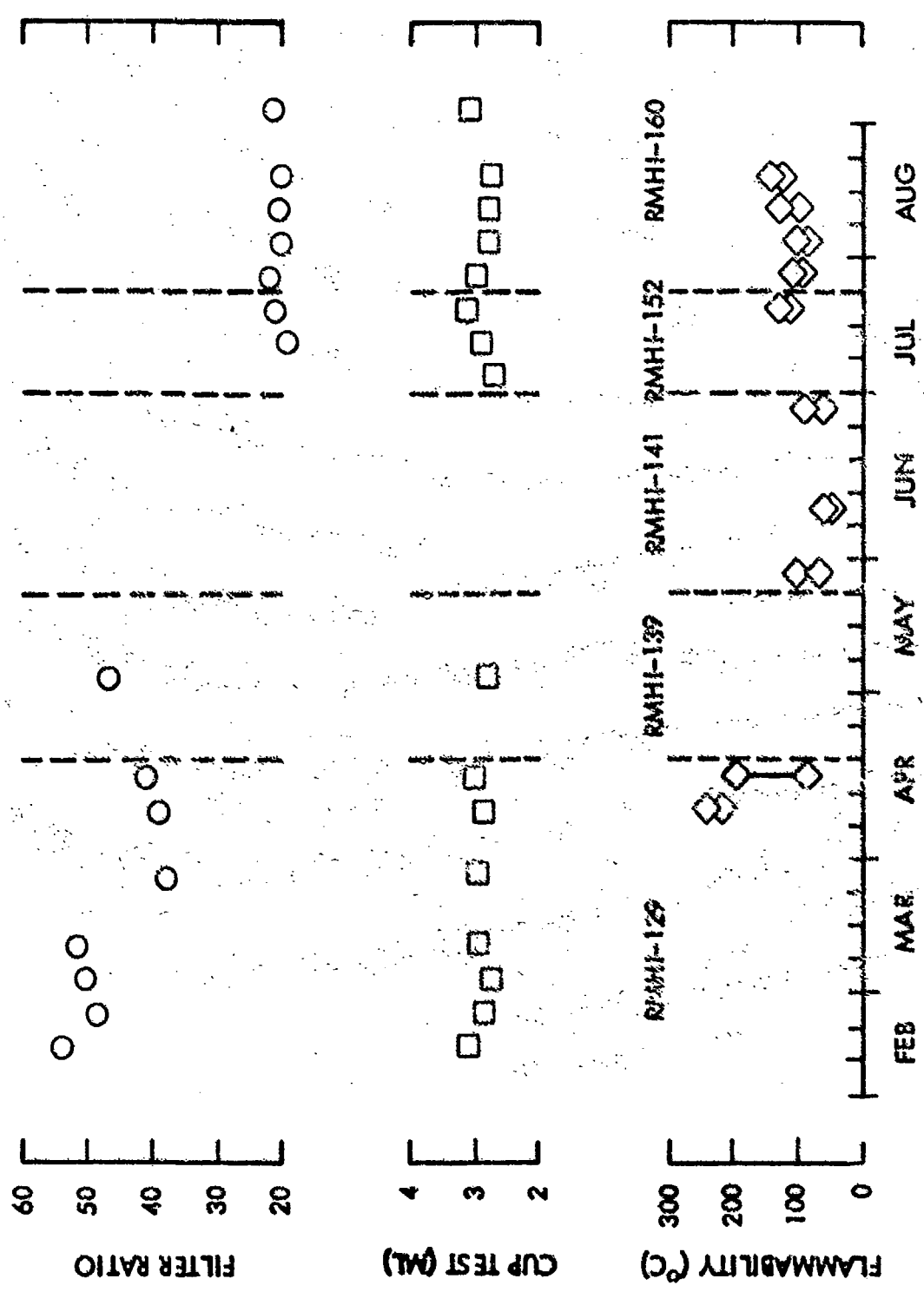


Figure 51. Summary of quality control test results. Batch numbers are supplied by Imperial Chemical Industries, Ltd. Flammability was measured with the FCIA using procedures summarized in Appendix II.

and elastic forces. Depending on the nature of the breakup configuration, nondimensional parameters which influence the processes are (see Wang, ref. 43.)

$$\text{Reynolds number} = \frac{\text{Inertial Force}}{\text{Viscous Force}}$$

$$\text{Weber Number} = \frac{\text{Inertial Force}}{\text{Surface Force}}$$

$$\text{Elastic Force Parameter} = \frac{\text{Inertial Force}}{\text{Elastic Force}}$$

Results are presented here for four experimental arrangements. Drop shattering and jet breakup were specifically studied in earlier NASA-sponsored work¹³ at JPL. To more closely relate observation to flammability tests, breakup of a fuel jet was also studied using the mini wing shear experiment. Drop sizes were also measured in the mini wing shear experiment to seek a relationship between them and observed flammability behavior. Similarly, drop sizes were measured in the flammability comparison test apparatus (FCTA)^{1,2} for comparison with flammability behavior observed in this experimental apparatus. Performance of an engine fuel nozzle in atomizing both neat Jet A and modified fuel was studied with the ultimate goal of determining necessary levels of degradation for recovery of proper nozzle behavior and to study the effects of the polymer additive on pressure nozzle atomization (sec. 6.2.2).

6.2.1 Mini Wing Shear

Simulating fuel ejection from a moving aircraft, the mini wing shear apparatus operates by ejecting fuel through an orifice into an oncoming airstream. Observations were made of the mode of jet disintegration for water, Jet A and Jet A with 0.30 % FM-9 (AMK) at 57, 73 and 96 m s⁻¹ oncoming air velocities. Jet velocities obtained through the 21 mm diameter fuel orifice

ranged from 0.45 to 3.51 m s^{-1} . Photographs were taken using the pulsed laser described in section 5.3 and the photographic arrangement described in section 5.4.

Figure 52 shows the fuel nozzle with no fuel flow and an inch-scale ruler for scaling. The behavior of Jet fuel injected into an air stream can be seen in figures 53 and 54. In the former, the air velocity is 96 m s^{-1} and the jet velocity at exit is 1.5 m s^{-1} . Figure 54 shows the breakup of AMK by an air-stream of 96 m s^{-1} . Figure 53 shows the rapid disintegration of the unmodified fuel into a cloud of small droplets. Jet penetration upstream of the exit nozzle is very limited because of the large amount of surface area of the many small drops exposed to the shearing flow. In contrast figure 54 shows the behavior of AMK at 96 m s^{-1} shearing air flow velocities and a jet speed of 0.5 m s^{-1} . In marked contrast to the other jets, these break up via a different mode. Rather than shearing immediately into drops, a sheet appears roughly perpendicular to the oncoming flow. Ligaments are then extruded from this sheet resulting in a ligament tearing atomization behavior characteristic of many viscoelastic fluids ⁴⁷. Even several centimeters downstream very few individual drops are apparent.

6.2.2 Drop Size Measurements

Image processing techniques have been applied to images of fuel sprays formed by the mini wing shear (sec. 4.1.1), F.C.T.A. (sec. 4.1.2) and nozzle spray (sec. 4.1.3) facilities. The first two of these experiments were developed as flammability tests. Fuel spray diagnosis was carried out at the location of the ignition source in each case to correlate spray parameters with flammability behavior. Atomization performance of the antimisting fuel and neat Jet A was measured with the nozzle spray facility.

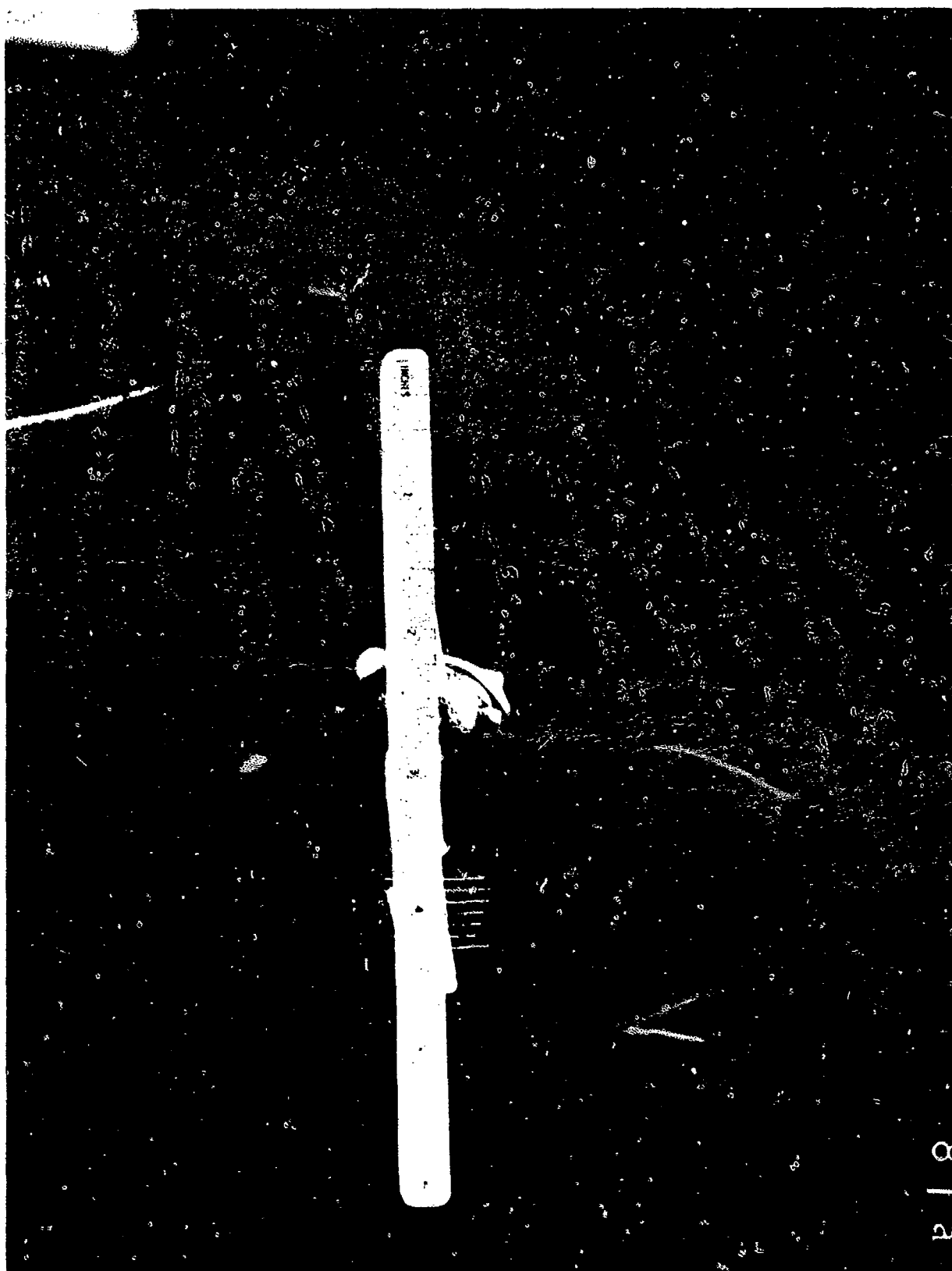


Figure 52. Mini wing shear jet breakup photographic perspective. An inch scale ruler is attached to the 1 inch orifice. The ignitor torch flange is visible at the extreme left.

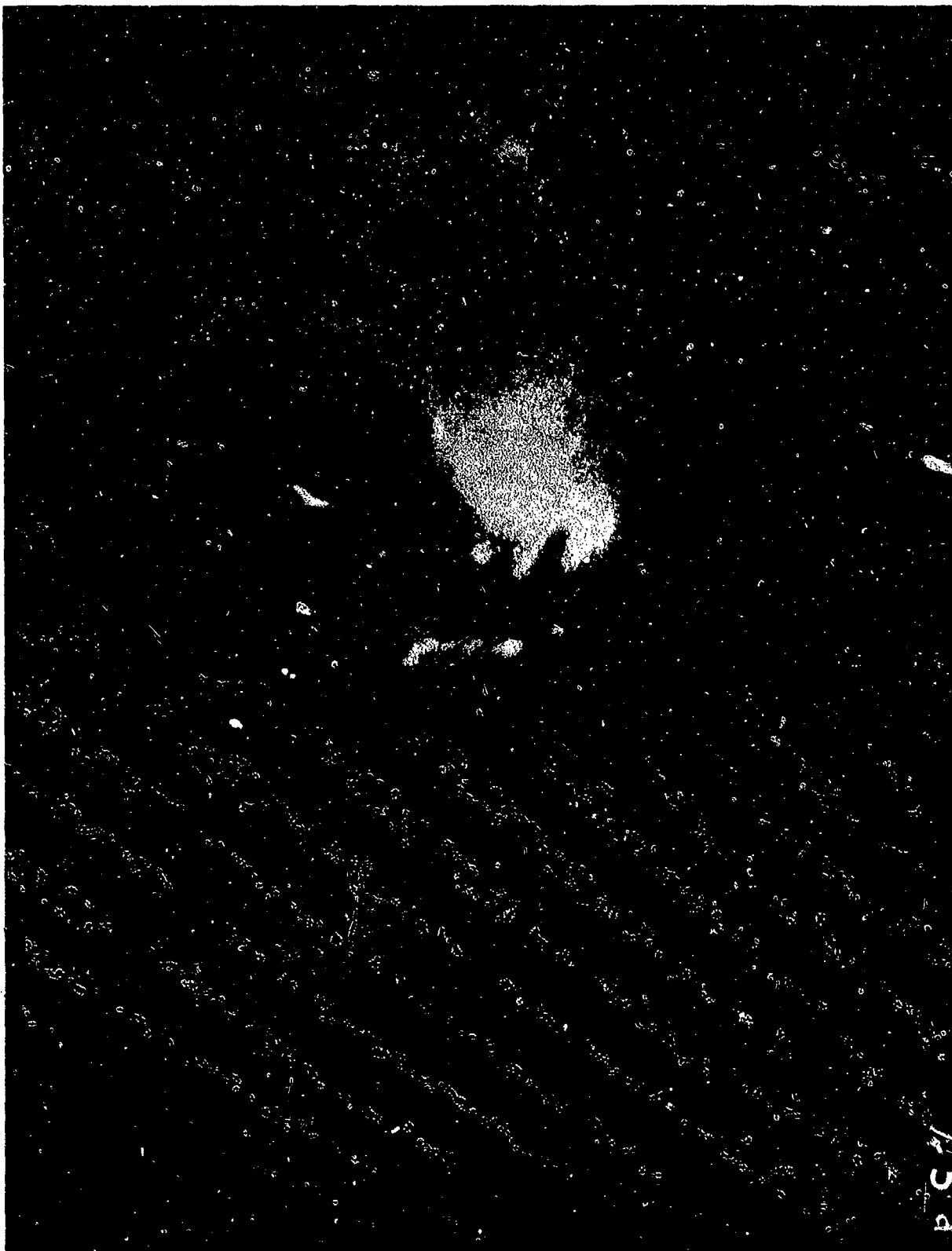


Figure 53. Breakup of a Jet A by a counterflowing airstream; liquid velocity 1.5 m s^{-1} , air velocity 96 m s^{-1} .



Figure 54. Breakup of AMK by a counterflowing airstream; liquid velocity 0.5 m s^{-1} , air velocity 96 m s^{-1} .

The importance of the short laser pulse duration to droplet imaging is shown by figures 55-57. They are images of Jet A sprays taken using photo-flash illumination (~ 1 ms duration), laser sheet illumination without the Pockels cell (~ 1 μ s duration) and laser sheet illumination with the Pockels cell (~ 25 ns duration). During the development of the improved illumination system, better photographic optics were also installed. Thus somewhat greater subject magnification is apparent in figure 57 than in figures 56 and 55. The major difference due to shorter duration illumination is in the elimination of streaking. In figure 55, no individual spray particles are visible and the spray appears as a smooth cloud. In figure 56, individual fuel elements are distinguishable though they still appear as streaks. With the 25 ns flash individual drops are visible (figure 57) without streaking or blurring. By illuminating only a narrow (~ 1 cm) slice of the spray, the opaque appearance of figure 55 is also eliminated.

Photographs of fuel sprays similar to fig. 57 were made for Jet A and antimisting fuel (Jet A + 0.3% FM-9) at 4 levels of degradation. Degradation was accomplished through blending for 0 (no degradation), 10, 30, and 90 seconds in a Waring kitchen blender⁴. Sample cup tests were 2.71, 7.05, 7.33 and 7.55 ml respectively. Jet A cup test results were 7.87 ml. Each fuel sample was photographed at flow rates corresponding to ignition, idle, cruise, and sea level takeoff conditions for the JT8-D engine fuel nozzle. All but the Jet A images were formed through mosaicing of three images (sec. 5.4). Analysis of photographs was accomplished using image processing methodologies described in section 5.5 and 5.6.

Comparison of atomization behavior may be made among figures 57 through 61. They show cruise flow rate conditions for Jet A and AMK at 0%, 84%, 90% and 93% restoration of Jet A cup test results. While the Jet A photo shows

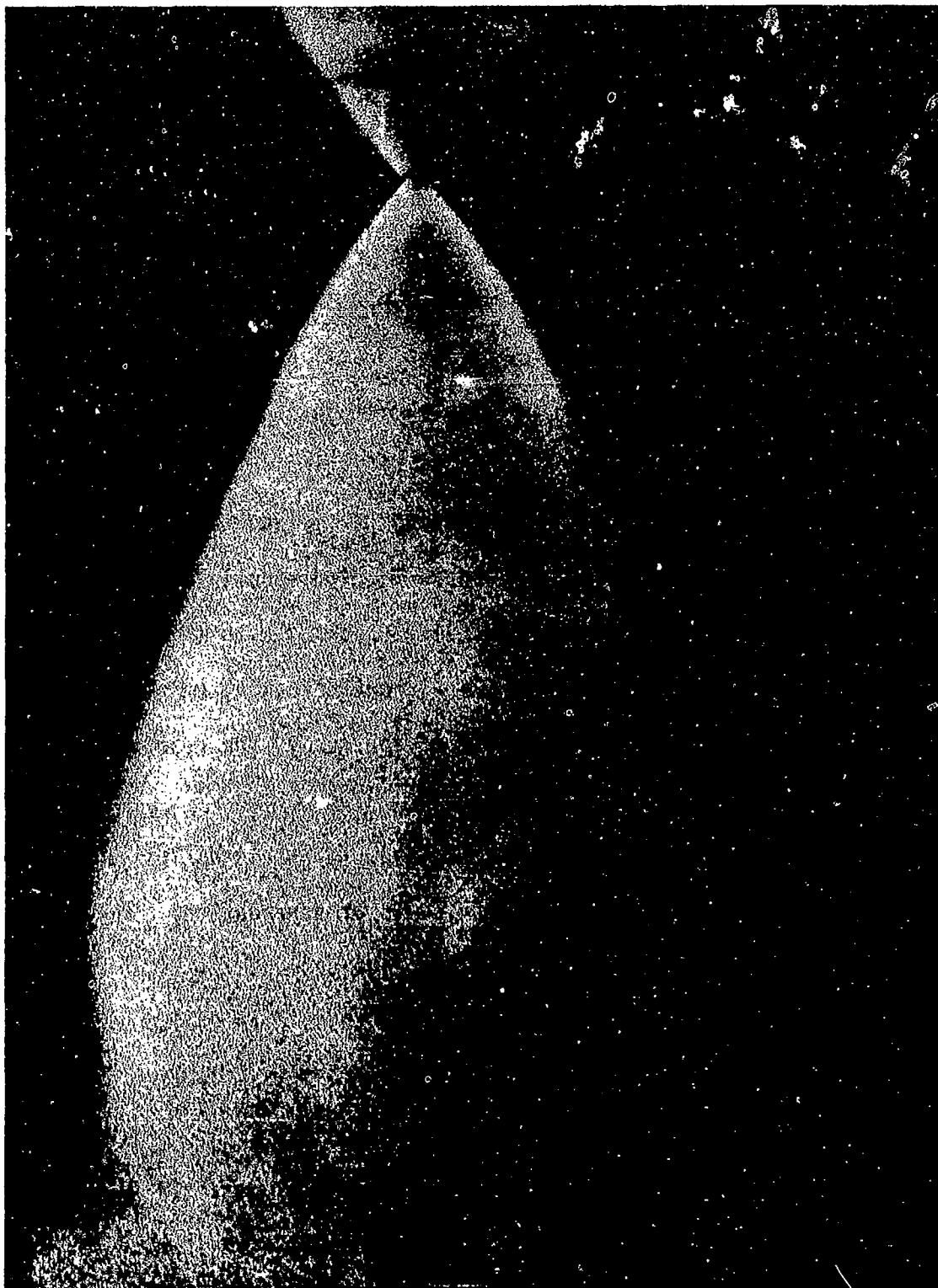


Figure 55. Jet A fuel spray photographed under photo-strobe illumination of ~1 ms duration.

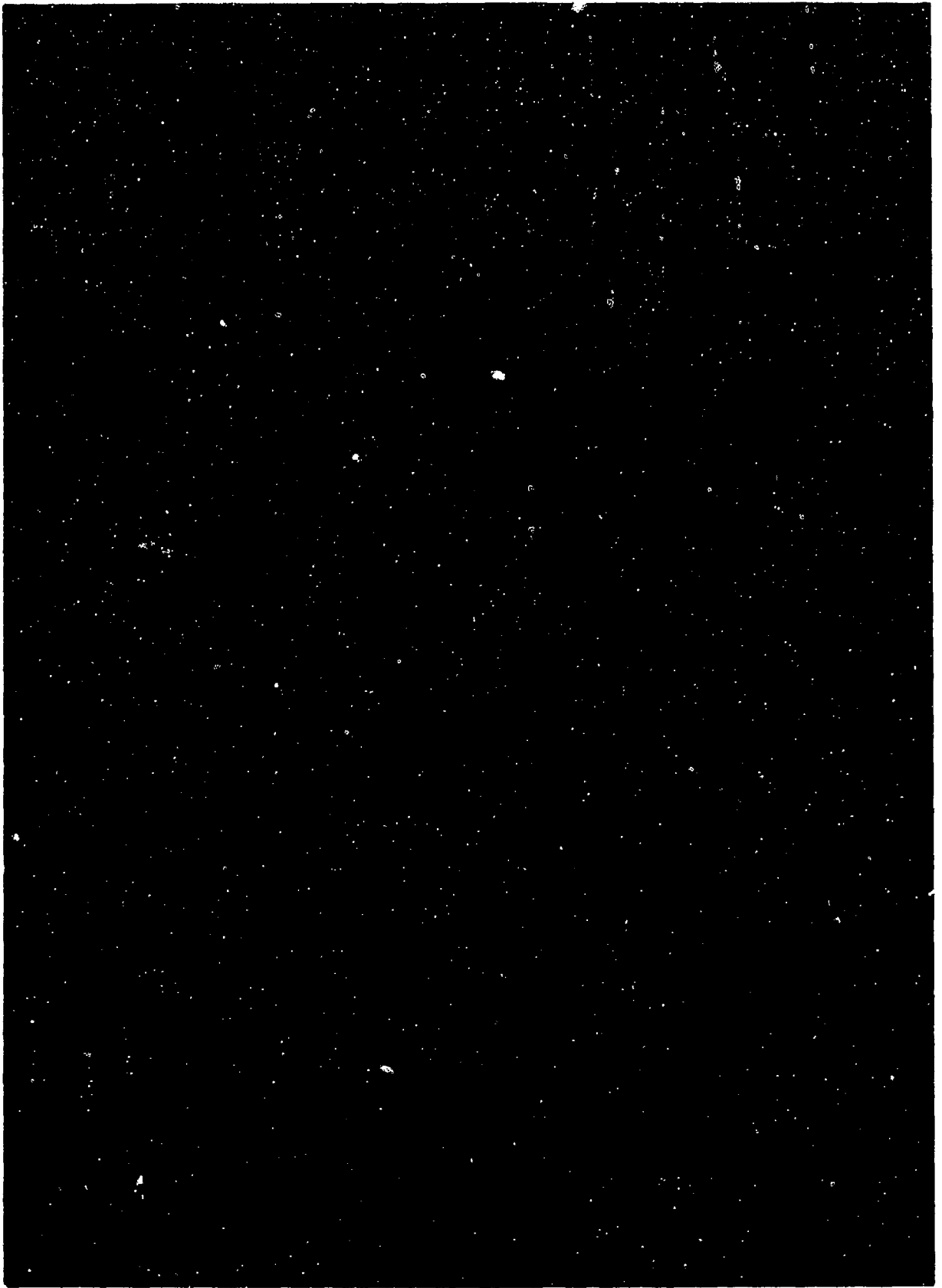


Figure 56. Jet A fuel spray photographed under pulsed laser sheet lighting of $\sim 1 \mu\text{s}$ duration.



Figure 57. Jet A fuel spray photographed under pulsed laser sheet lighting of ~25 ns duration.

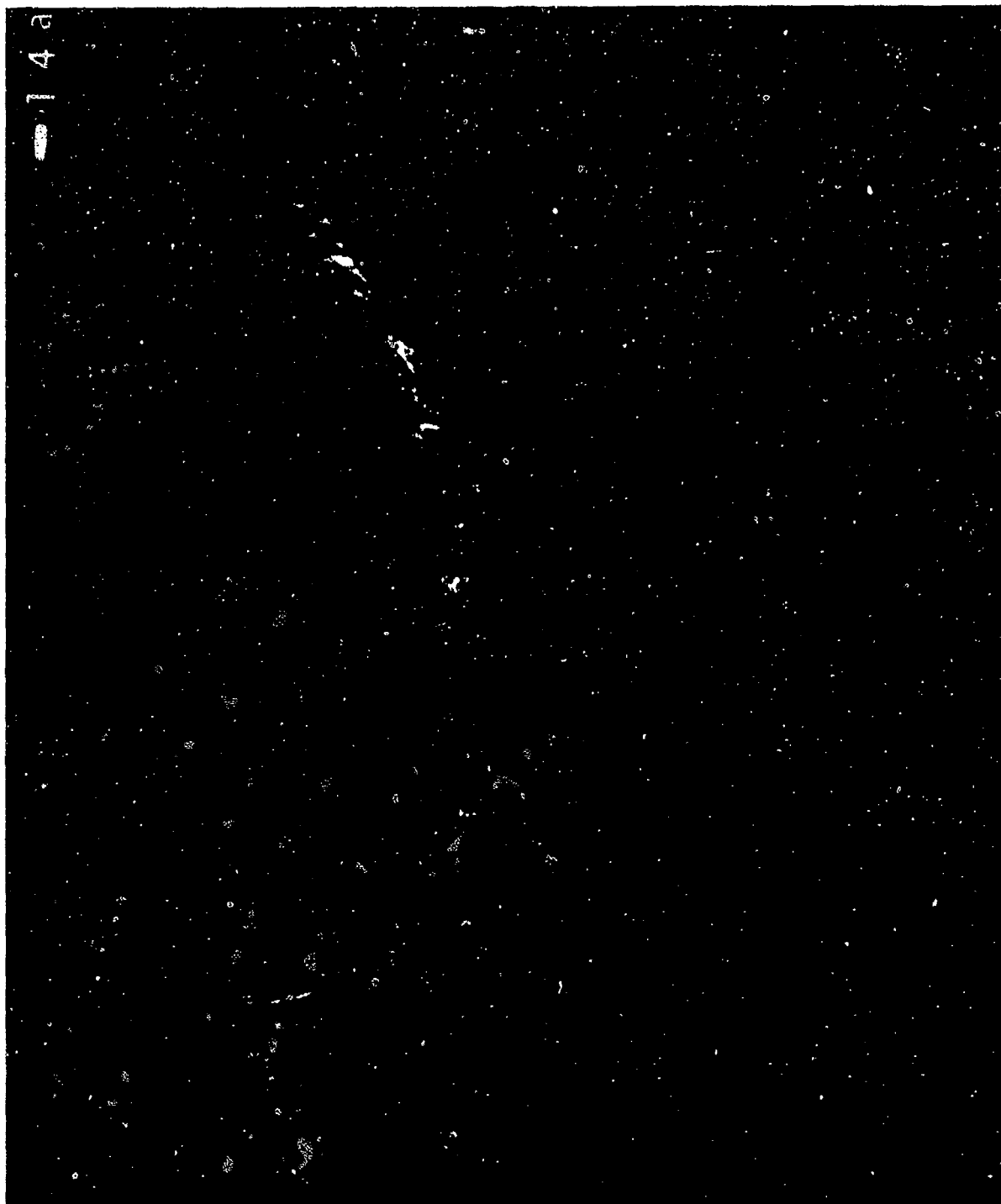


Figure 58. Spray of undegraded AMK at cruise flow rate.

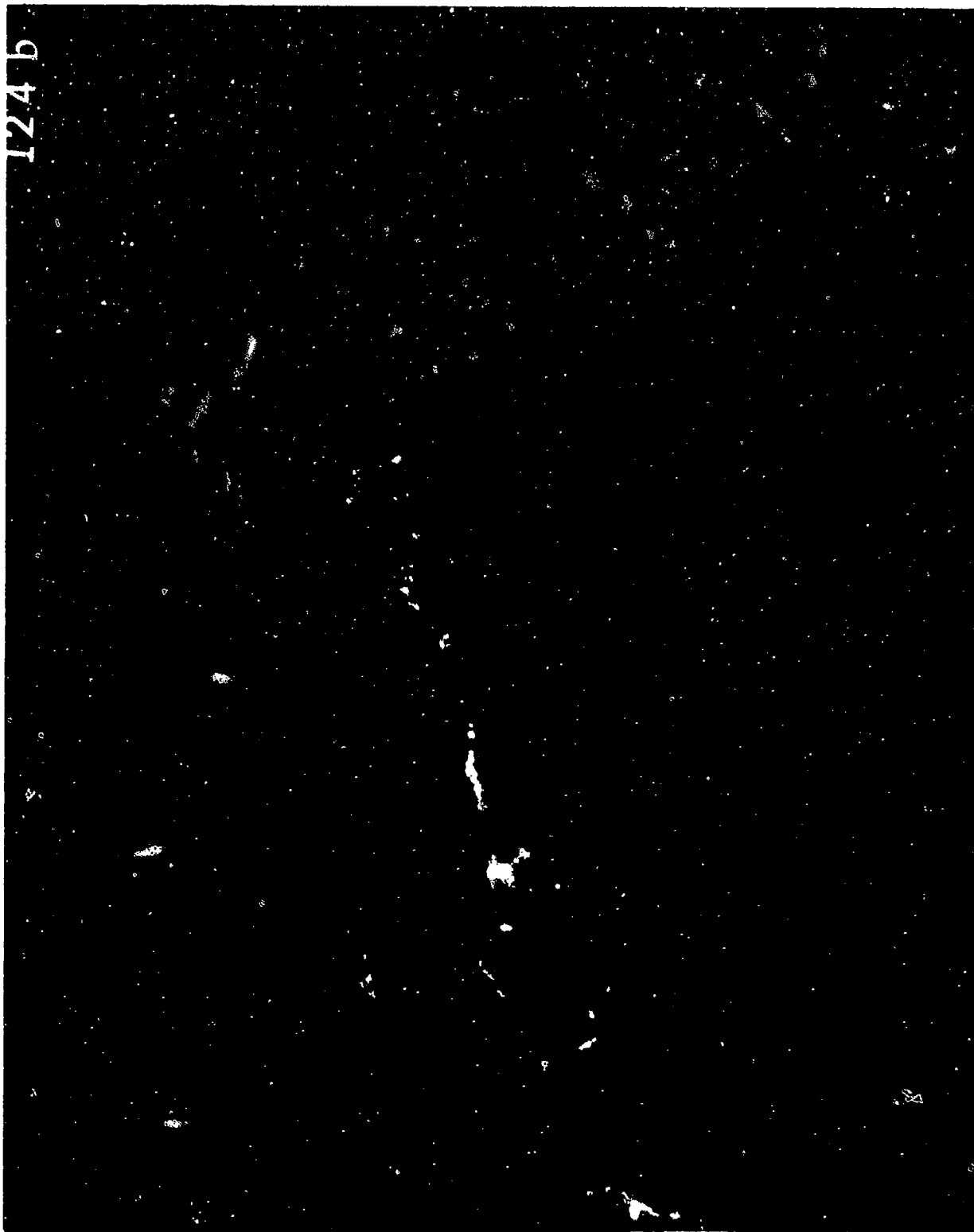


Figure 59. Spray of 84% degraded AMK at cruise flow rate.

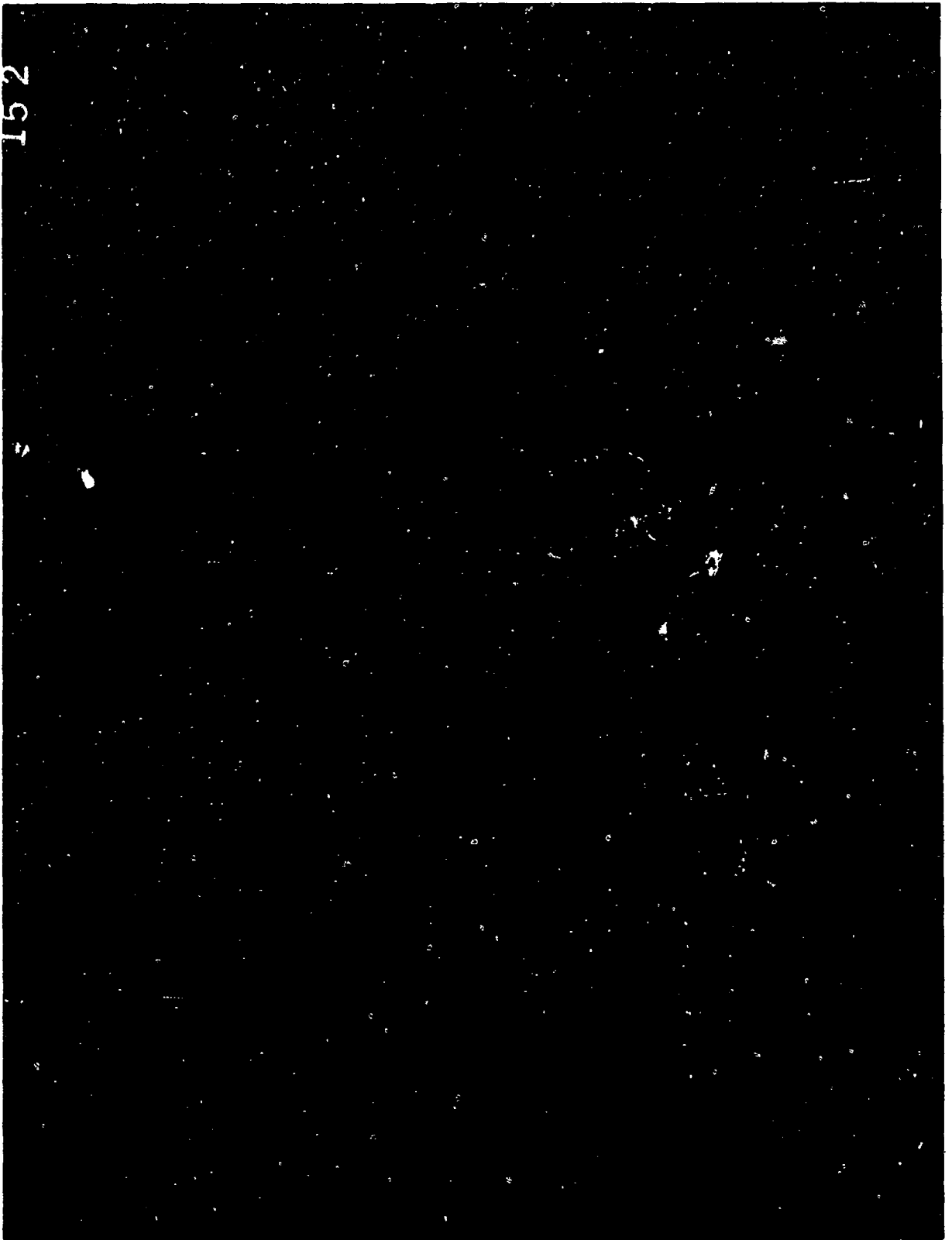


Figure 60. Spray of 90% degraded AMK at cruise flow rate.



Figure 61. Spray of 93% degraded AMK at cruise flow rate.

rapid atomization, jet breakup is delayed for all AMK samples. Even at 93% degradation, many relatively large (> 1 mm diameter) droplets remain.

The resistance of AMK to separation is clearly demonstrated by figures 62 (93% degraded AMK, ignition flow rate) and 63 (Jet A ignition flow rate). At this relatively low flow rate the AMK jet remains intact despite the development of waves with heights much larger than the jet thickness. No conical spray pattern appears and the only spreading is due to growth of the waves. Similar behavior is exhibited at cruise flow rate for 90% degraded AMK (figure 87). While a definite conical shape is apparent, the sheet is smooth indicating suppression of high frequency instabilities. The thin fuel sheet again resists fracturing for a great distance downstream. In comparison, figures 63 (Jet A, ignition flow rate) and 57 (Jet A, cruise flow rate) show very rapid growth of instabilities, sheet breakup and formation of a broad cone angle.

Image analysis was undertaken of fuel spray images in the mini wing and FCTA ignition regions. The goal of these analyses was to measure spray qualities including Sauter mean diameter and drop number density and correlate these measures with flammability. Additionally they should demonstrate the ability of the system to make local measurements, e.g., for comparison of fuel atomization at different axial distances from a nozzle.

At the time of writing, the results were generated from microdensitometer data generated from our laser-illuminated images. This is primarily because of delays in the delivery of the DeAnza imaging system. These data are unfortunately of low quality because of the way in which the microdensitometer was operated which resulted in compression of the brightness levels to only about 10 values. This makes threshold level selection very critical. It is probably not possible to extract meaningful data from these microdensitometer-generated digital images on this account. The data compression super-

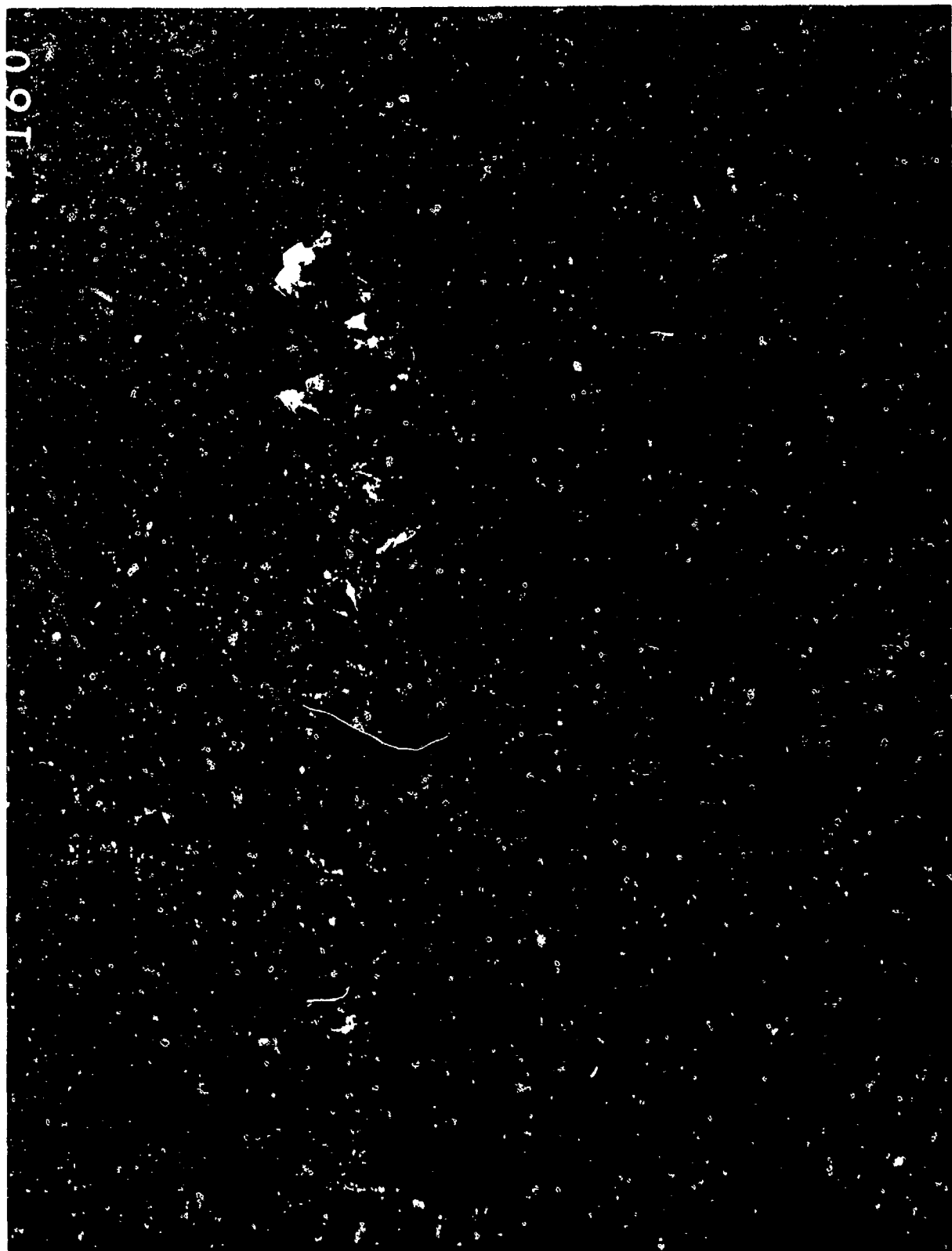


Figure 62. Atomization of 93% degraded AMK at ignition fuel flow rate.

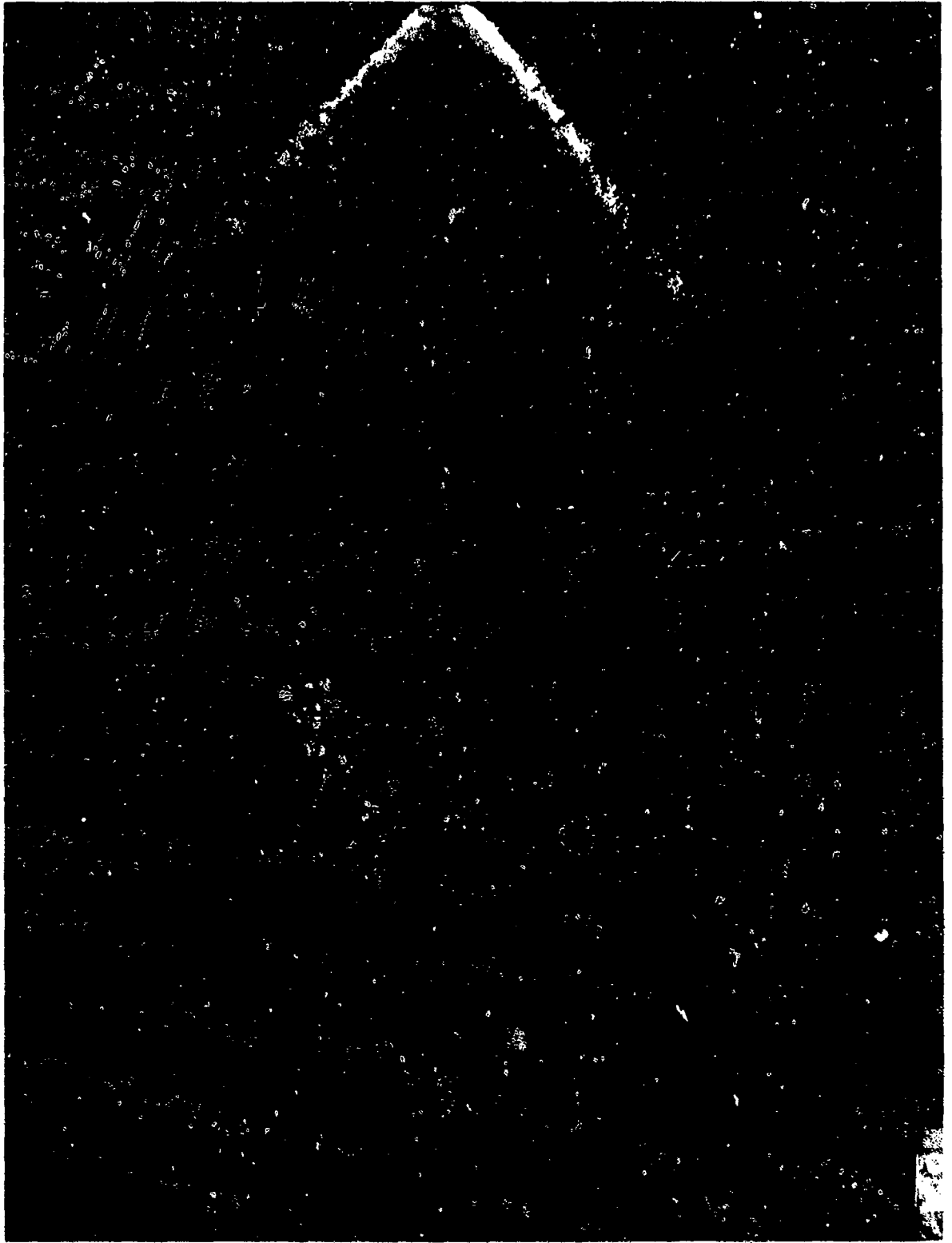


Figure 63. Atomization of Jet A at ignition fuel flow rate.

imposes both analogue noise (film grain and illumination gradient) and digital noise (from sampling operations) on the signal of interest, the drop images.

Final selection of drop recognition algorithms has also not been made, mainly because of problems with the digitization scheme.

For these reasons, the discussion of these results should be considered as a report on the state of affairs at the end of the first year effort. Generally, no conclusions on the relationship between flammability and spray characteristics may be drawn from the results at this stage.

Image analysis was undertaken for Jet A and AMK fuel sprays at cruise flow rate using the algorithm of section 5.6. From the initial images (e.g. figure 57) a window was chosen 5 cm downstream of the nozzle for analysis. The ability of this drop counting method to characterize spray locally allows measurements of drop sizes at various spray locations. To demonstrate this capacity drop statistics have been generated for the Jet A cruise flow condition at 2 cm, as well as 5 cm, downstream of the nozzle.

A subimage generated by application of the counting algorithm is shown in figure 64. Data obtained through image processing have been used to obtain the Sauter mean diameter, local cone angle, drop number density and pseudo volume fraction. The drop number density is the number of drops observed in the window divided by the window volume. The pseudo volume fraction is the density of fuel within the image space. It is the percentage of the total pixel matrix occupied by fuel and is felt to be representative of local spray density.

Data obtained for the three conditions studied are summarized in table 2. Cone angle trends reinforce subjective opinion of atomization behavior. The Jet A cone angle is initially large (38°), decreasing slightly due to flow turning to 32° at the farther window. The AMK cone angle is considerably less

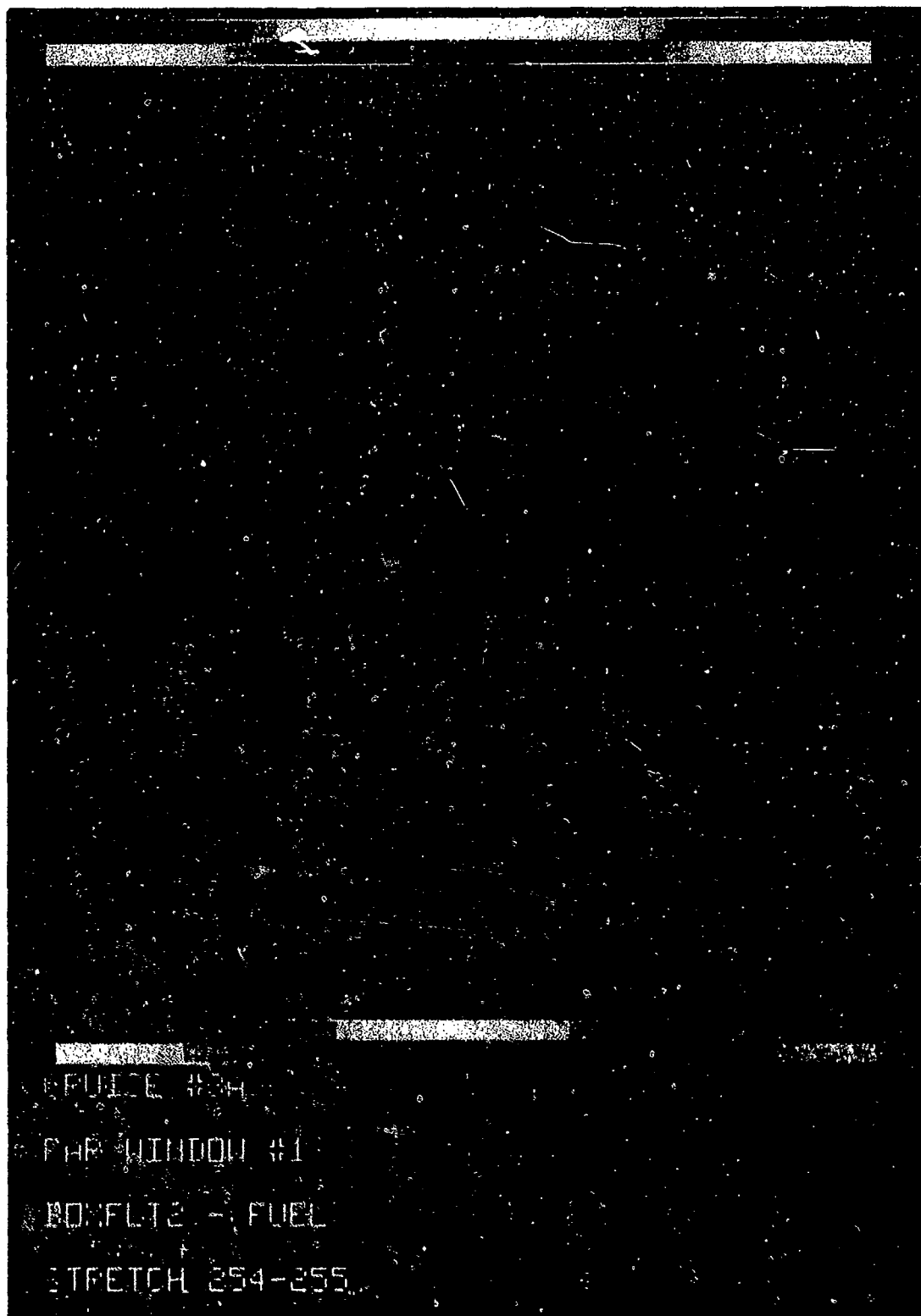


Figure 64. Portion of the Jet A fuel spray image 5 cm downstream of the nozzle cruise flow rate, after application of image processing.

TABLE 2

Drop Statistics Summary: Nozzle Spray Tests

	Jet A 5 cm Window	AMK 5 cm Window	Jet A 2 cm Window
Cone Angle, deg	32	11	38
SMD/ μm	79	65	63
Drop Number Density, ³ drops/mm ³	24	5.4	13
Drop Pseudo Volume Density,%	8.0	7.7	3.7

(11°), indicating dispersion of the fuel through the combustor volume would be poor. The lack of variation in the SMD's for apparently widely varying sprays is taken as an indication of data dilution by considerable noise. A complete summary of cone angle observations is given in table 3.

When looking at a picture of the large scale spray (e.g. fig. 58), none of the small drops is apparent. This is because of the averaging nature of the photographic process in imaging small details in negatives. Images of small drops are simply too small to be resolved when printed on the scale of figure 58. Many fewer droplets are observed for AMK than Jet A. Since the mass flow rates are identical, the AMK drops should therefore have been larger on the average. Pseudo volume fractions are also low for the AMK and Jet A sprays at 2 cm. This would also indicate larger overall drop volumes since fewer, larger drops will yield a lower image saturation than more, smaller drops. These values may indicate that much of the fuel spray was not counted in these images. This may have occurred because of maximum pixel limits imposed during processing. These limits are set to reject drops counted with apparent diameters greater than 2 mm in order to avoid counting stray objects in the viewing field such as illuminated portions of the nozzle itself or its supporting hardware. Many large drops may have been interpreted as this type of stray image and rejected from processing. The low coverage would thus be an indication of large pixel dropouts and hence the presence of many large drops.

Drop size histograms have also been generated from drop counting data, but at this stage should be considered a demonstration of system potential and not as a reliable description of the observed sprays. An example is shown in figure 65 for Jet A at 5 cm. This type of data presentation offers more complete spray information than is contained in just the Sauter mean diameter.

TABLE 3
Nozzle Spray Cone Angles

		Initial Angle, deg	Final Angle, deg
Jet A	Ignition	38	32
	Idle	35	27
	Cruise	38	32
	S.L.T.O.*	39	28
AMK (undegraded)	Ignition	0	0
	Idle	42	22
	Cruise	21	11
	S.L.T.O.*	43	40
AMK (84% degraded)	Ignition	0	0
	Idle	28	16
	Cruise	22	20
	S.L.T.O.*	36	25
AMK (90% degraded)	Ignition	0	0
	Idle	22	22
	Cruise	24	11
	S.L.T.O.*	35	35
AMK (93% degraded)	Ignition	0	0
	Idle	47	28
	Cruise	39	35
	S.L.T.O.*	30	35

*Sea Level Take Off

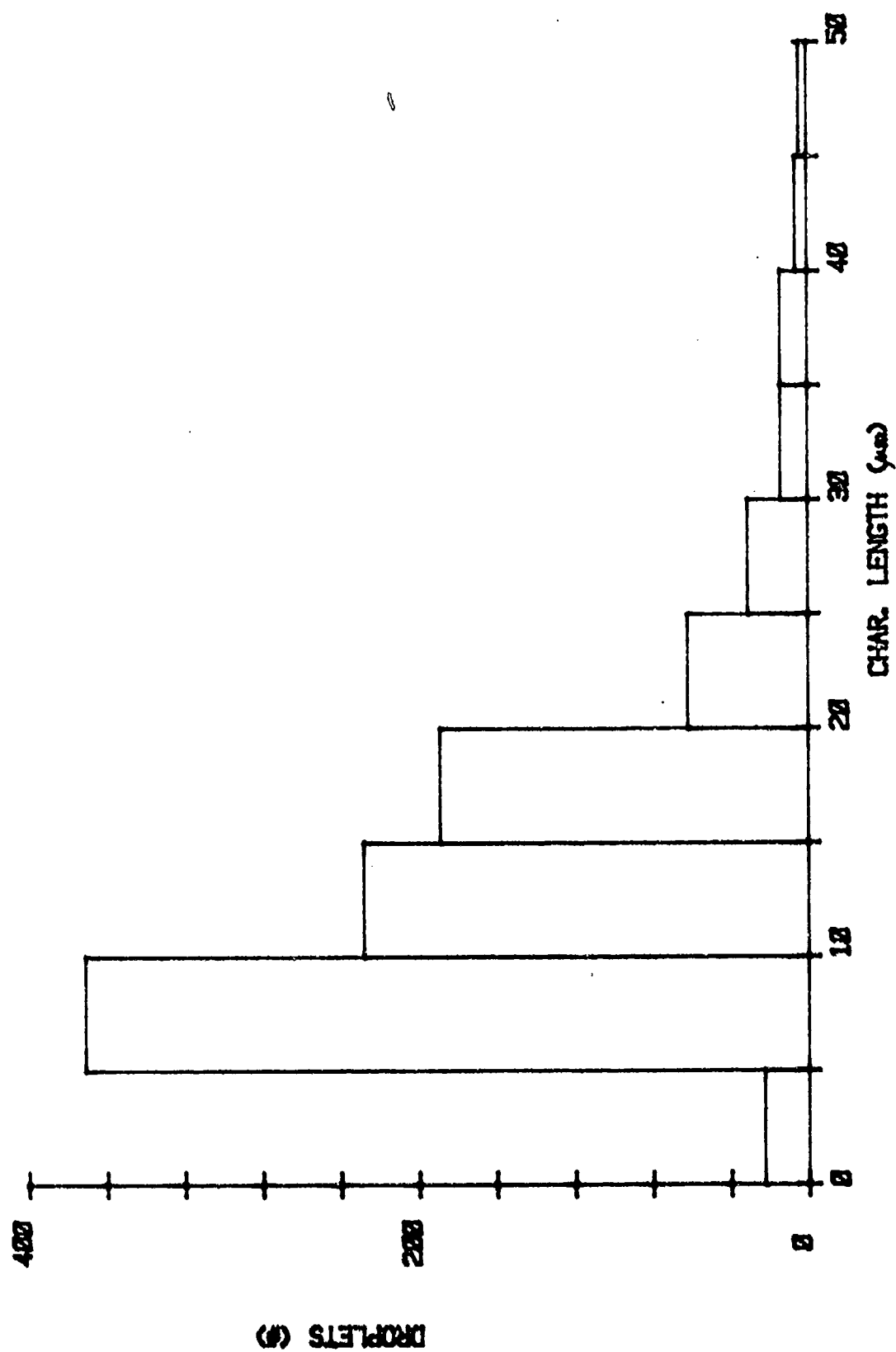


Figure 65. Histogram of drop sizes for the Jet A, cruise fuel flow rate spray, 5 cm downstream of the nozzle.

Because the histograms have been generated with linear bins, they do not show the complete dynamic range considered (up to 2000 μm). Even 1 or 2 drops in these very large bins have a large effect on computed SMD values. The statistical significance of such low numbers of particles is uncertain and their inclusion may also have biased the results. This is a question for future consideration.

To investigate correlations between spray characteristics and flammability, photographs were made of droplets formed in the mini wing shear experiment (section 4.1.1) and FCTA (section 4.1.2) under identical flow conditions to those used in flammability testing (Section 6.1). It is noted that for purposes of this study, operation of the FCTA was modified. This was done so that reduced temperatures could be computed from it for comparison with the mini wing shear experiments, and to attempt correlation of reduced temperature with spray characteristics. The results are included here primarily because the image digitization was somewhat improved over the mini wing shear data and therefore yielded more meaningful results. Until system improvements can be made, all these experimental results must be considered preliminary. Figure 66 shows the general flowfield surrounding the fuel source. Attention was focused on the region just downstream of the torch where fuel would pass through the flame of the ignitor. Figure 67 shows the viewing window with no flow and an inch ruler for scaling. Photographs were made for a matrix of experimental points spanning airspeeds of 60 to 96 m s^{-1} , fuel flow rates of 0.2 to 0.8 kg s^{-1} , and polymer concentrations up to 0.30%.

As a further test of the capabilities of the spray characterization methodology developed, a few of these photographs were digitally processed. The processed images were of clear pass and fail conditions for 0.30% FM-9 (60 m s^{-1} and 96 m s^{-1} airspeeds respectively, both at 0.60 kg s^{-1} flow rates),

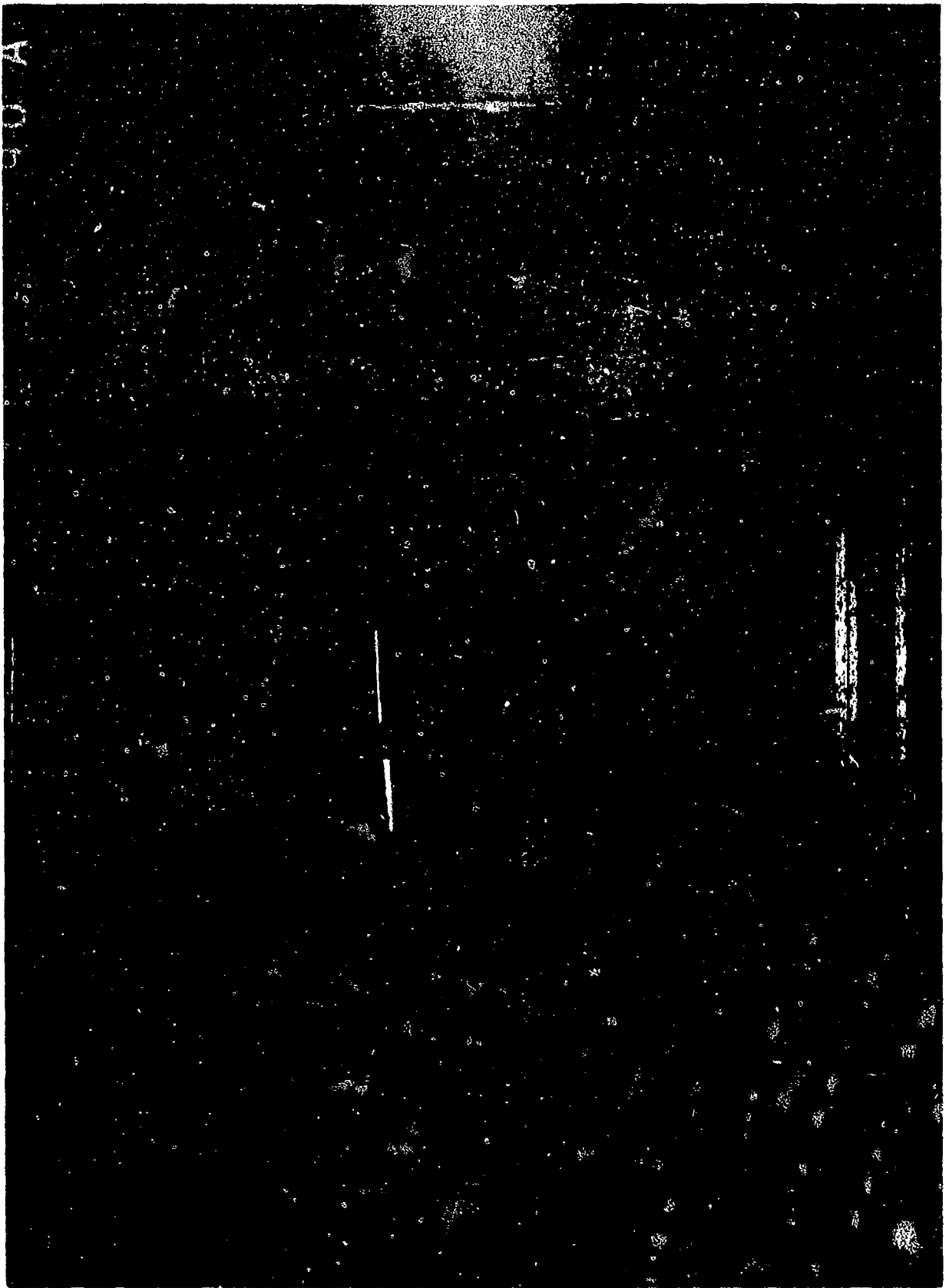


Figure 66. Apperance of liquid spray formed in the mini shear facility. Downstream (right) of the nozzle is the oxyacetylene torch with shroud used for fuel spray ignition.

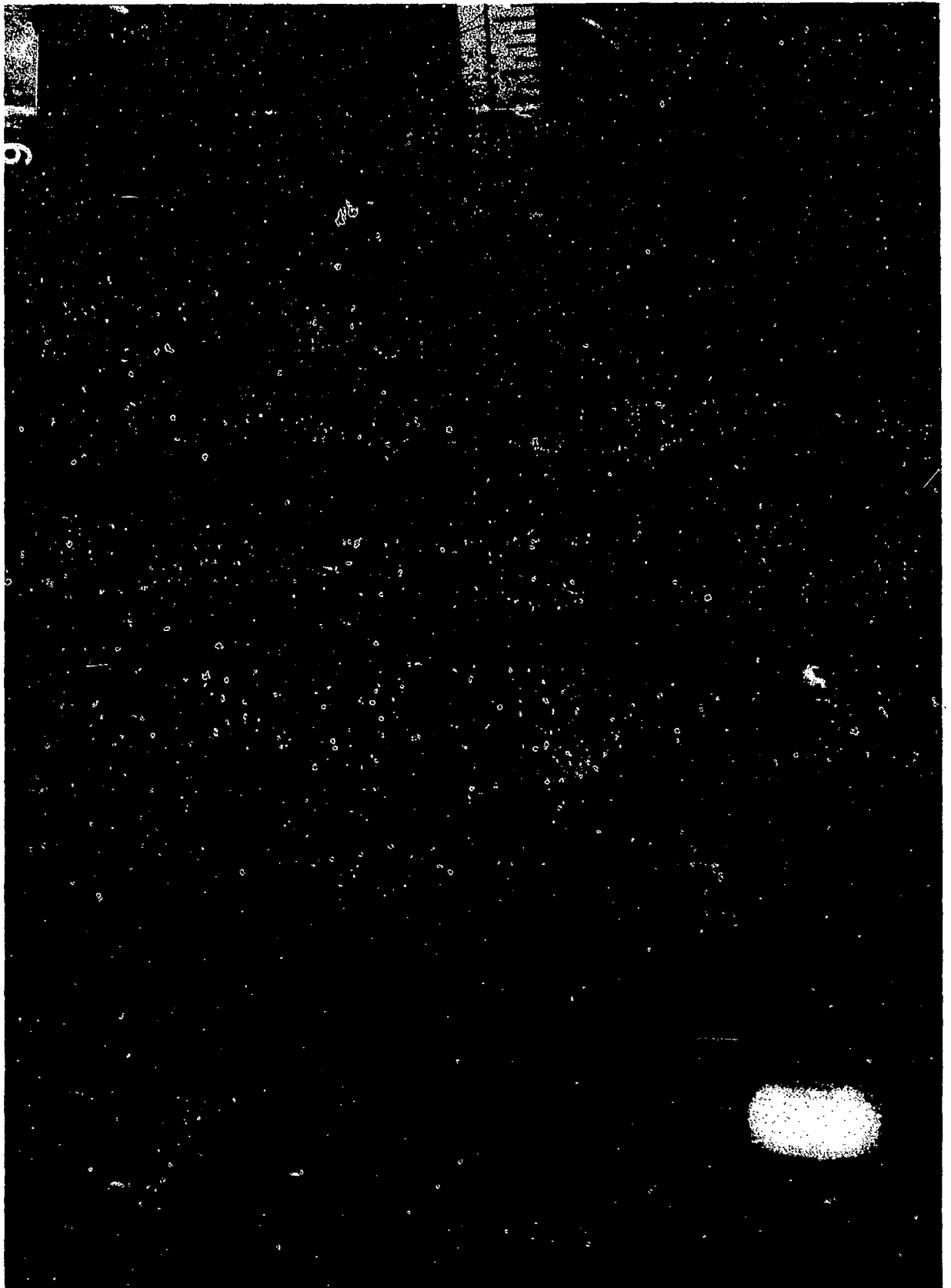


Figure 67. Viewing window for mini wing shear drop size measurements. The torch flame is visible below the 3-inch mark on the ruler.

and of a 60 m s^{-1} airspeed pass condition (with 0.25% FM-9 AMK) and marginal-to-fail conditions (with 0.20% FM-9 AMK). Thus the pass/fail boundary was examined both through variation of the polymer concentration and of airspeed. No conclusions may yet be drawn from these data because of the poor quality of A/O conversion.

FCTA tests were photographed over a range of polymer concentrations. The pass/fail boundary also occurred for these tests between 0.20% FM-9 and 0.25% FM-9 so these two cases were digitized and processed.

The six conditions treated in detail are: for the mini wing shear (all at 0.6 kg s^{-1} fuel flow rate), 0.30% FM-9 AMK at 60 m s^{-1} airspeed (pass) and 96 m s^{-1} airspeed (fail), 0.25% FM-9 AMK at 60 m s^{-1} airspeed (pass) and 0.20% FM-9 AMK at 60 m s^{-1} (marginal to fail) for the FCTA, both at a flow rate setting of 900 with a plenum pressure of 90 psi, 0.25% FM-9 AMK (pass) and 0.20% FM-9 AMK (fail).

Figures 68 and 69 show some of the raw images of the mini wing shear fuel sprays. The flow is left to right with the torch exit flange in the picture at the center left. The atomizing effect of the higher airspeed of figure 68 compared to figure 69 is apparent in the breakup of the central fluid filament. This explains why the pass condition (fig. 69) seems to contain less fuel than the fail condition (figure 68) despite their equal fuel flow rates.

Digitization of six images from the mini wing shear and FCTA devices was carried out for small windows corresponding to 43.7 mm^2 of the actual spray for the mini wing and 33.1 mm^2 for the FCTA. The windows analyzed were then vertically oriented rectangular regions at the approximate center of the images for the mini wing, and square boxes in the lower right hand corner for the FCTA.

Data derived from these images are listed in table 4 and presented in

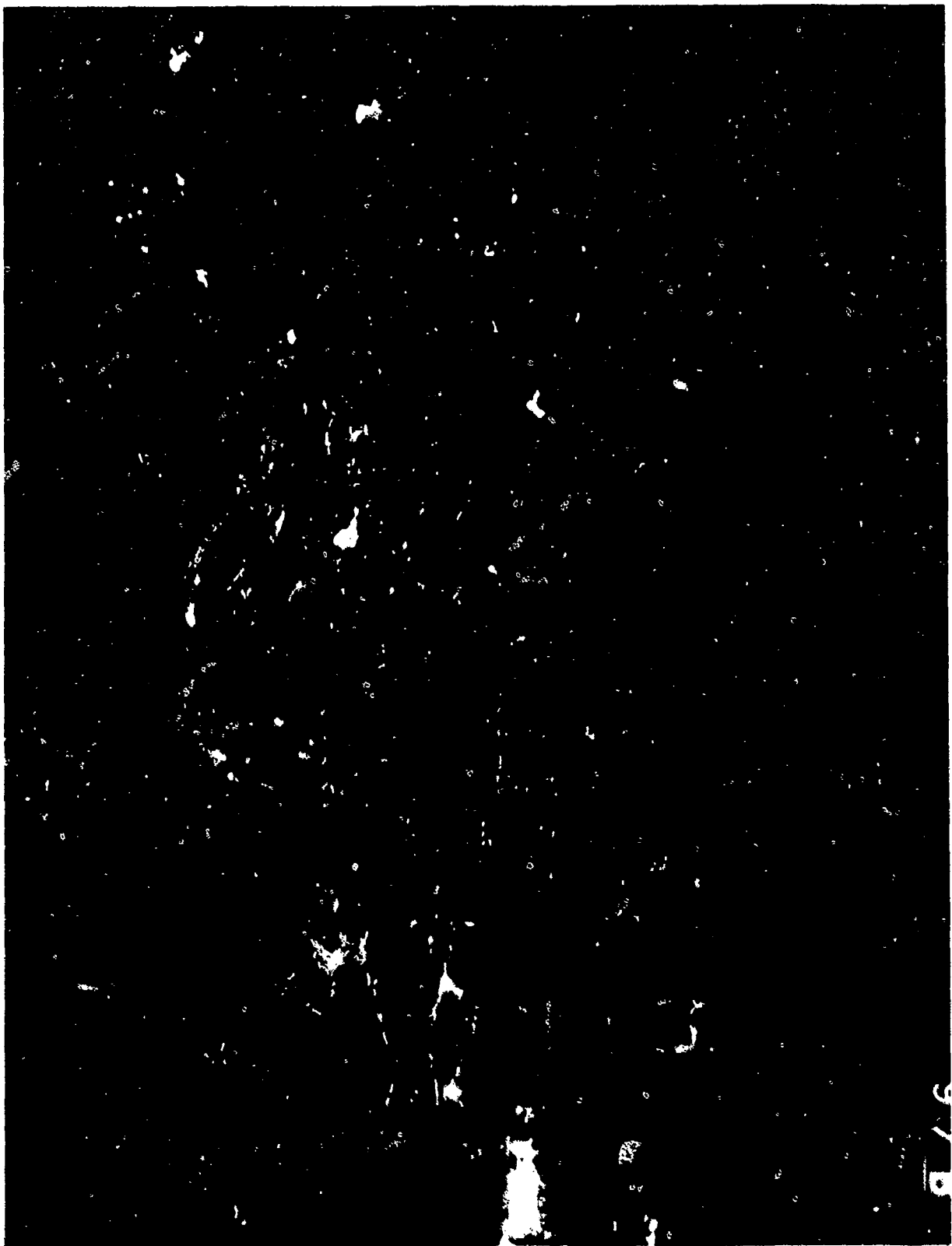


Figure 68. Drops formed by breakup of a Jet A + 0.03% FM-9 in an airstream of 96 m s^{-1} velocity (fire test failed under these conditions).

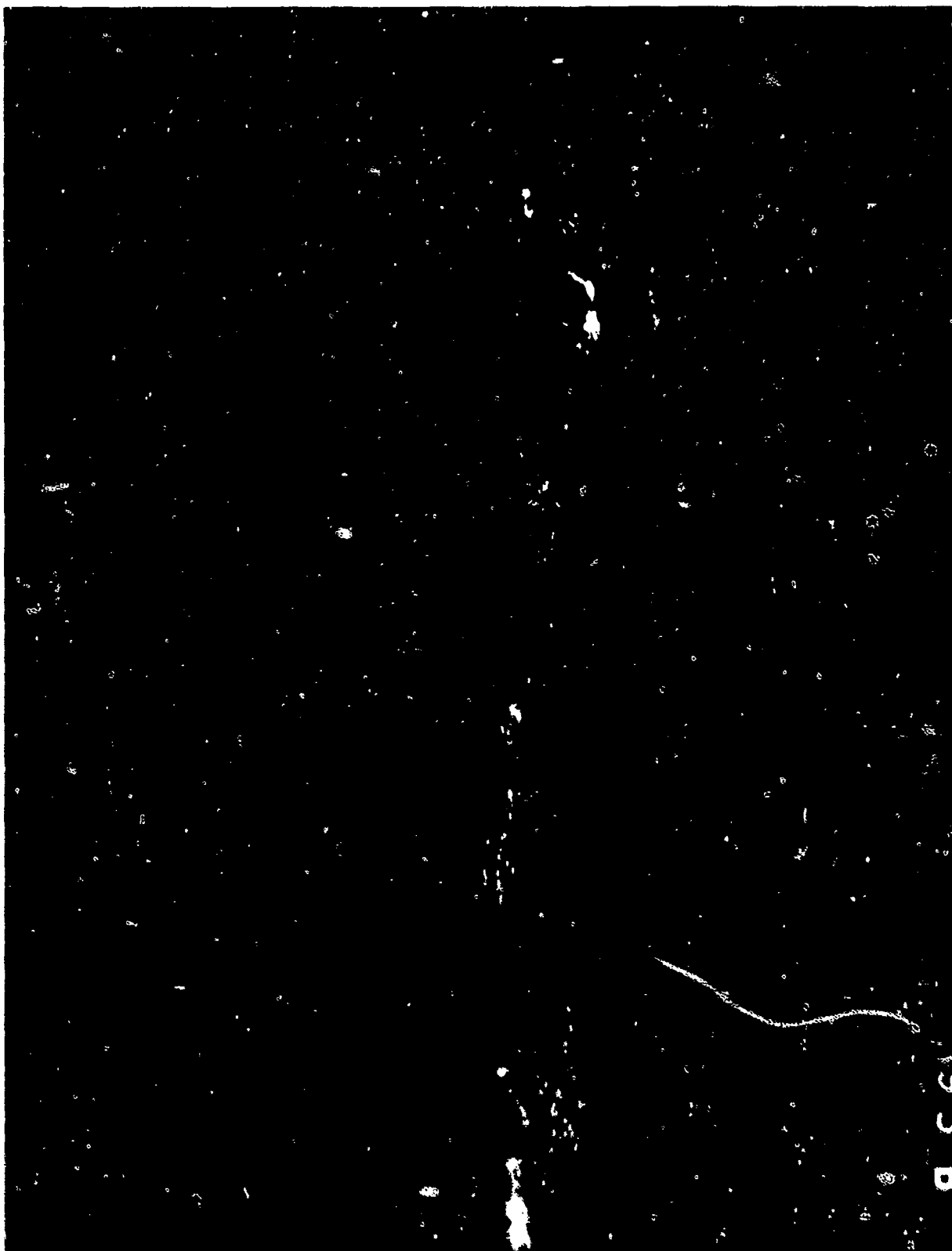


Figure 69. Drops formed by breakup of Jet A + 0.30% FM-9 in an airstream of 60 m s^{-1} velocity (fire test passed under these conditions).

histogram form in figures 70-75. Looking first at the table, SMD values have been computed based on alternative schemes. The upper (volume/area) value is computed from separate volume and area data derived from area and perimeter measurements as described in section 5.6. The lower (characterization) values are computed by forming the cube and square of a single characteristic length parameter for each drop. These values are then added and combined to form the SMD in the normal way. While the values derived in these two manners differ, the trends between them do not. The upper value is preferred as it is based upon more direct calculation of the total spray volume and area while the lower value rests on a more narrowly applicable characteristic length argument.

Results of the FCTA measurements show strong agreement of SMD and flammability data. The failure corresponds to a spray SMD less than 1/3 that of the pass SMD. As expected, the droplet number density decreases as the size increases because the flows contain equivalent fuel quantities. Pseudo volume densities reinforce earlier conjecture that a large number of small drops fill the pixel space more rapidly than a small number of larger drops.

As was the case with the nozzle spray, mini wing shear results seem to run counter to this trend. Large SMDs and relatively large fuel loadings correlate with failures, while drop number densities are apparently unrelated to flammability performance. This discrepancy will be more thoroughly investigated when better digitized images become available.

The histograms offer further insight into the nature of the pass/fail boundary relationship to counted drop sizes. The apparent difference between the pass and fail histograms for 0.30% FM-9 AMK (figs. 70 and 71, respectively) is mainly the much larger number of particles in the 0-60 μm diameter size range. This is the size range of drops which is expected to offer the

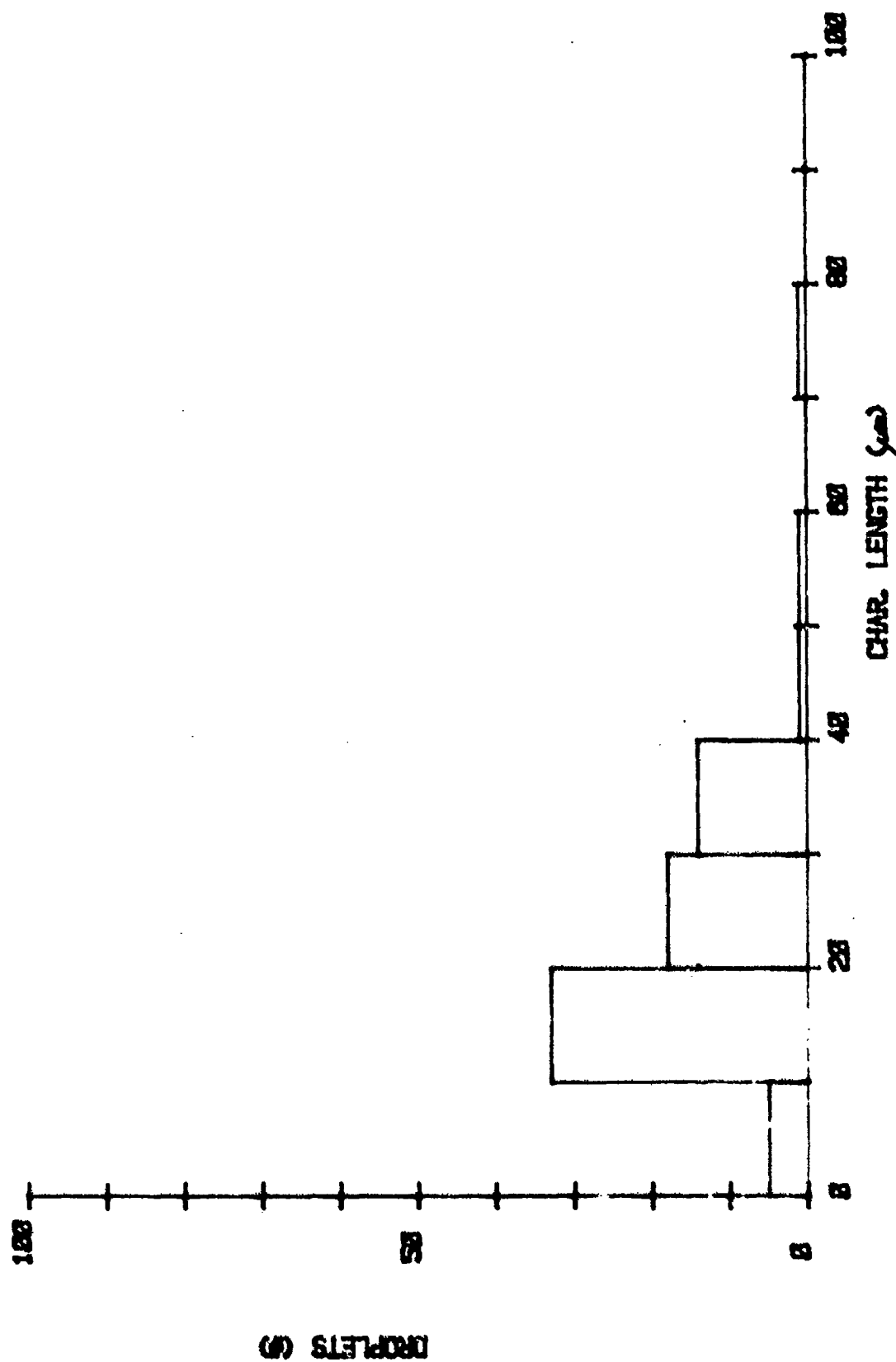


Figure 70. Histogram of drop characteristic length observed at the mini wing shear ignition source; Jet A + 0.30% Fm-9 fuel, 60 m s⁻¹ airspeed. (Fire suppression test passed under these conditions.)

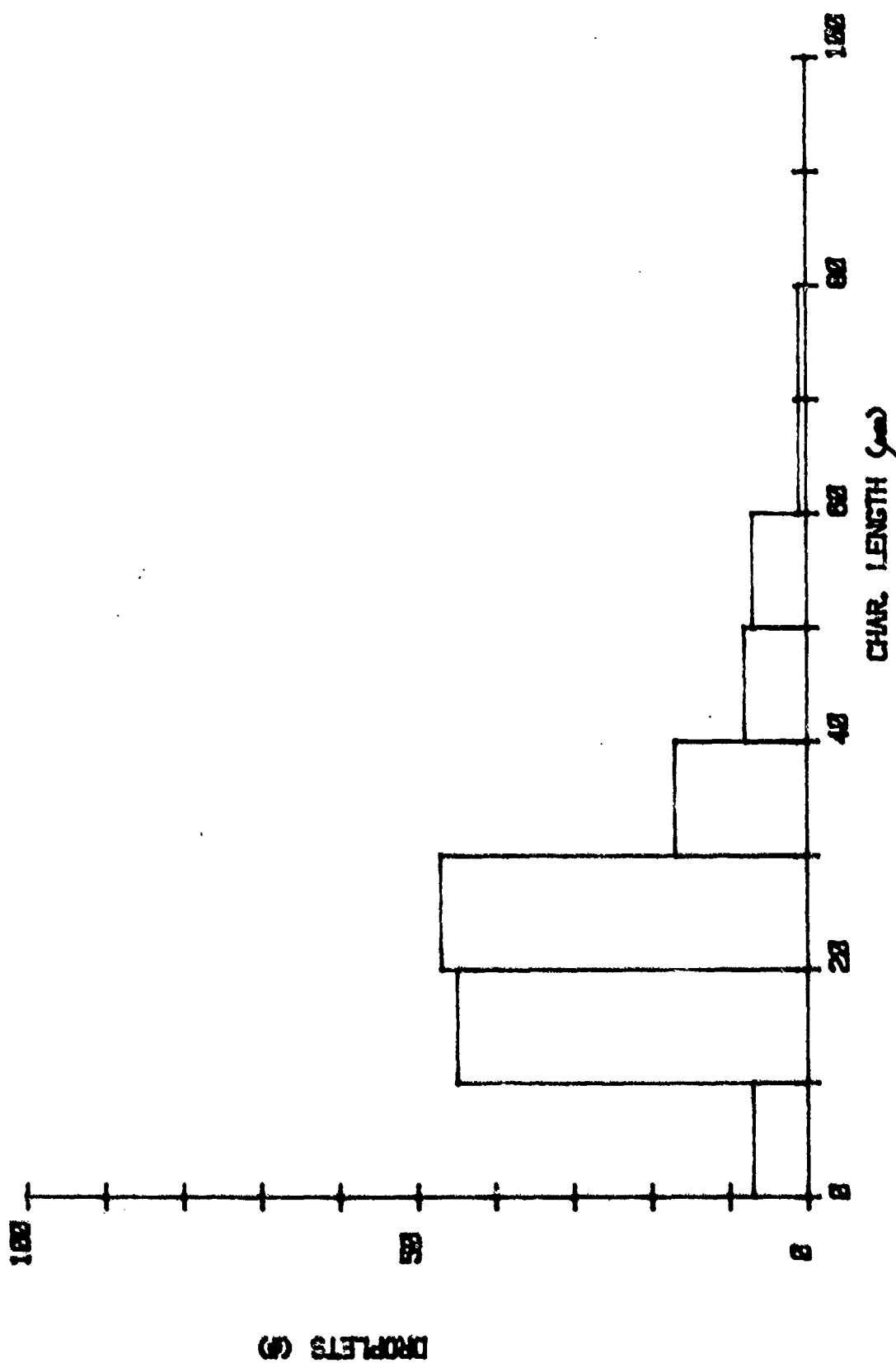


Figure 71. Histogram of drop characteristic length observed at the mini wing shear ignition source; Jet A + 0.30% FM-9 fuel, 96 m s⁻¹ airspeed (fire suppression test failed under these conditions).

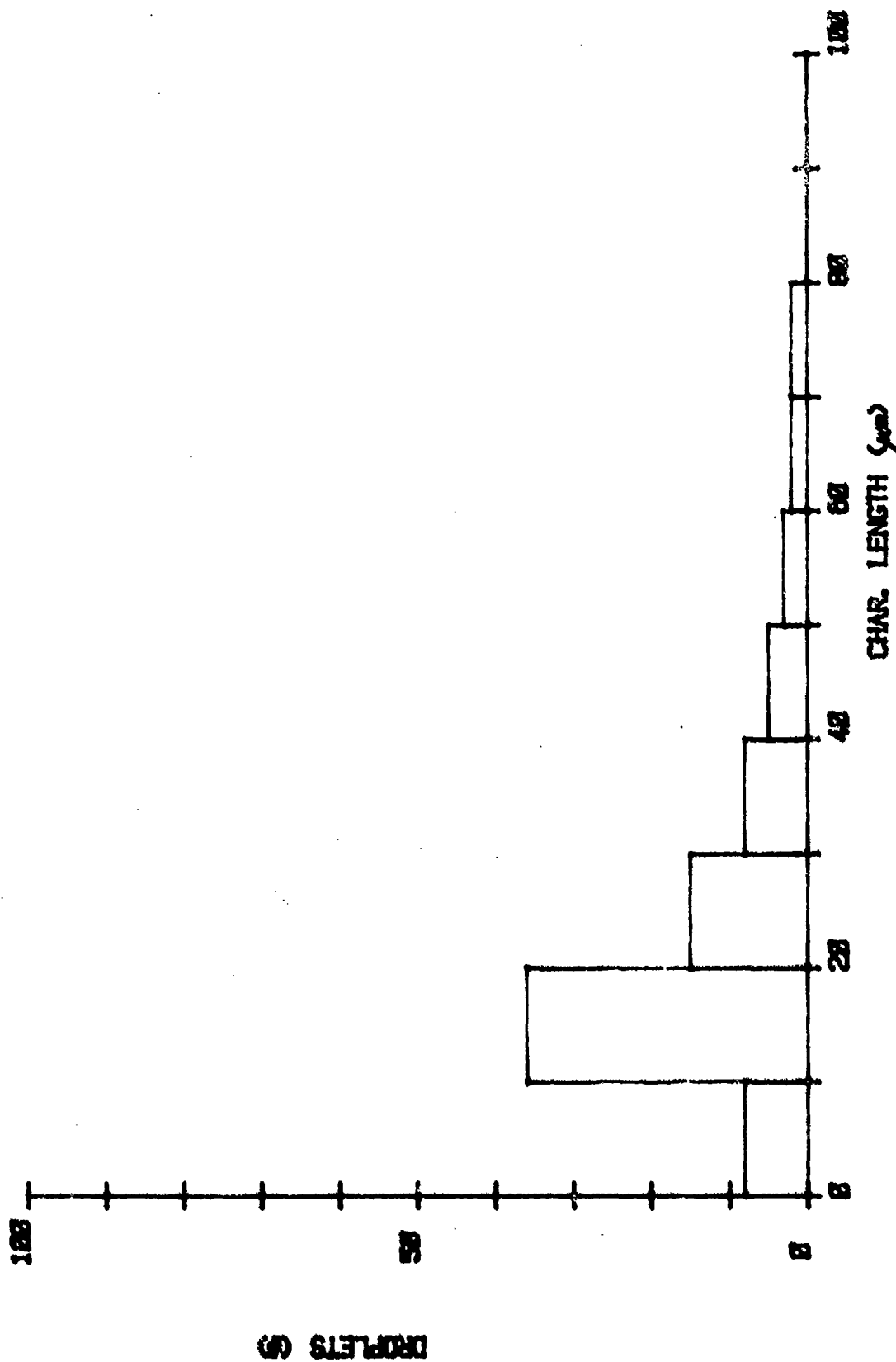


Figure 72. Histogram of drop characteristic length observed at the mini wing shear ignition source; Jet A + 0.25% FM-9 fuel, 60 m s⁻¹ air speed (Fire suppression test passed marginally under these conditions).

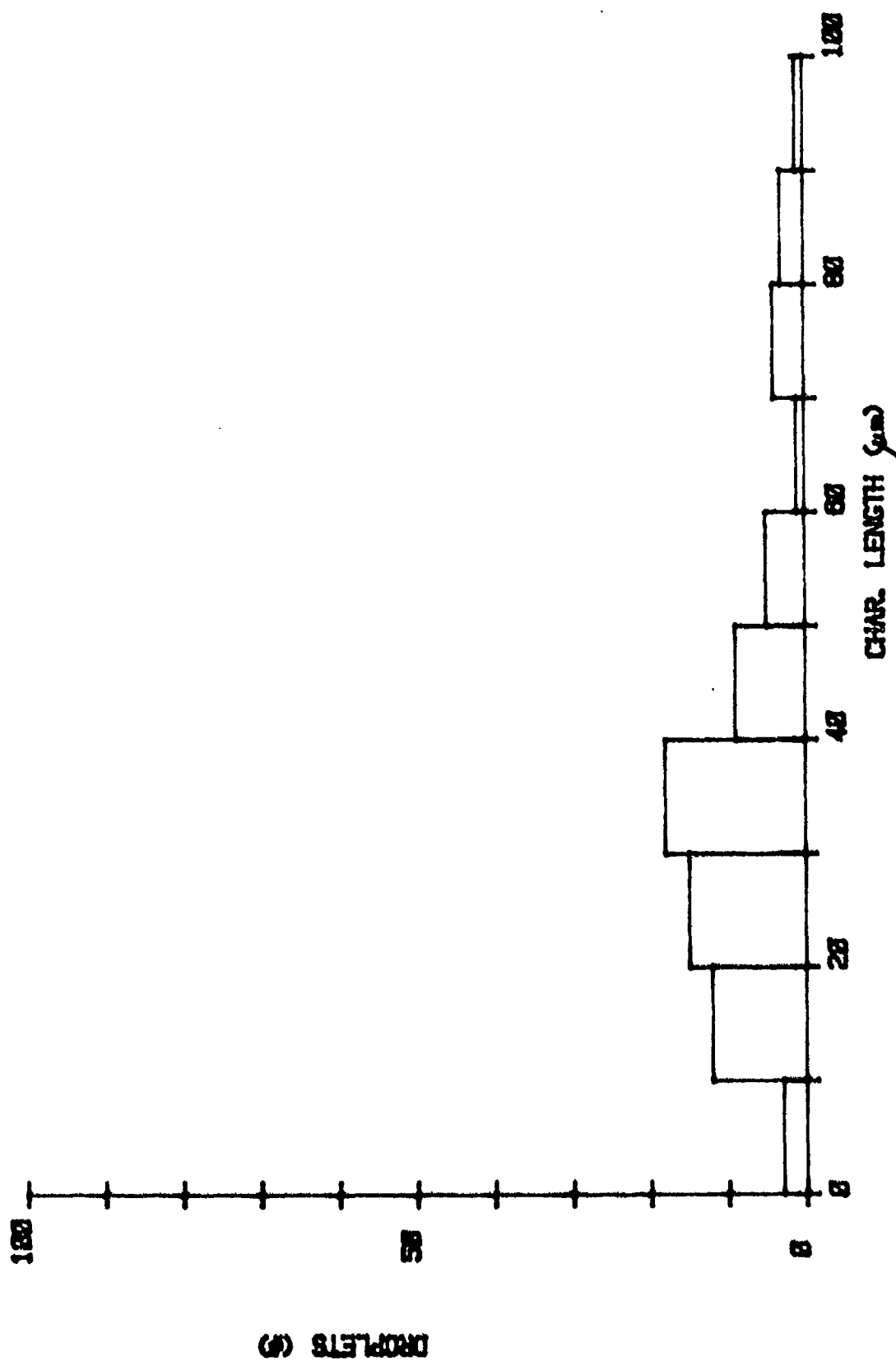


Figure 73. Histogram of drop characteristic length observed at the mini wing shear ignition source; Jet A + 0.20% FM-9 fuel, 60 m s⁻¹ airspeed (fire suppression test failed under these conditions).

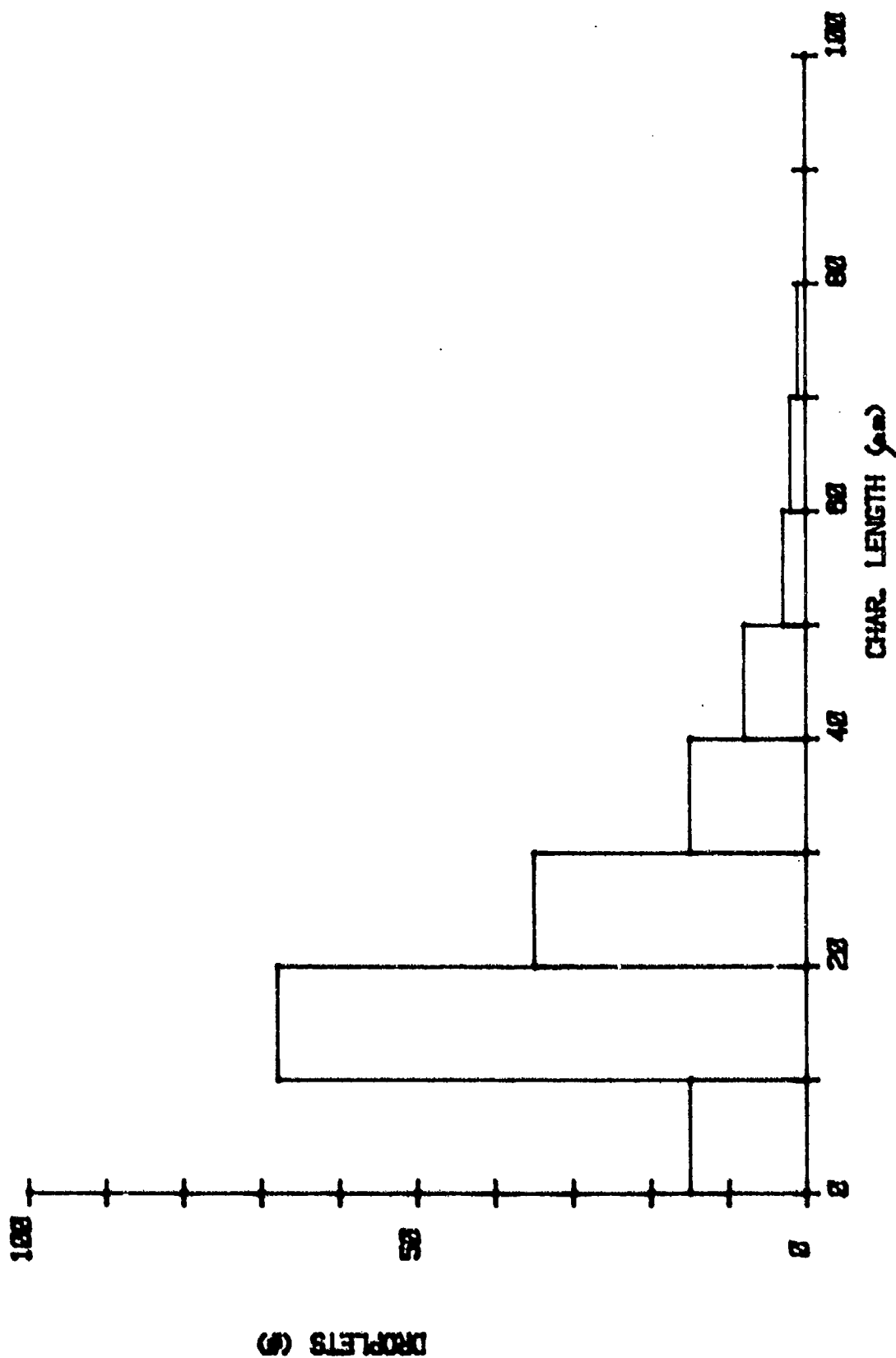


Figure 74. Histogram of drop characteristic length observed at the FCTA ignition source; Jet A + 0.25% FM-9 fuel, 6.1 atm accumulator pressure (fire suppression test passed under these conditions).

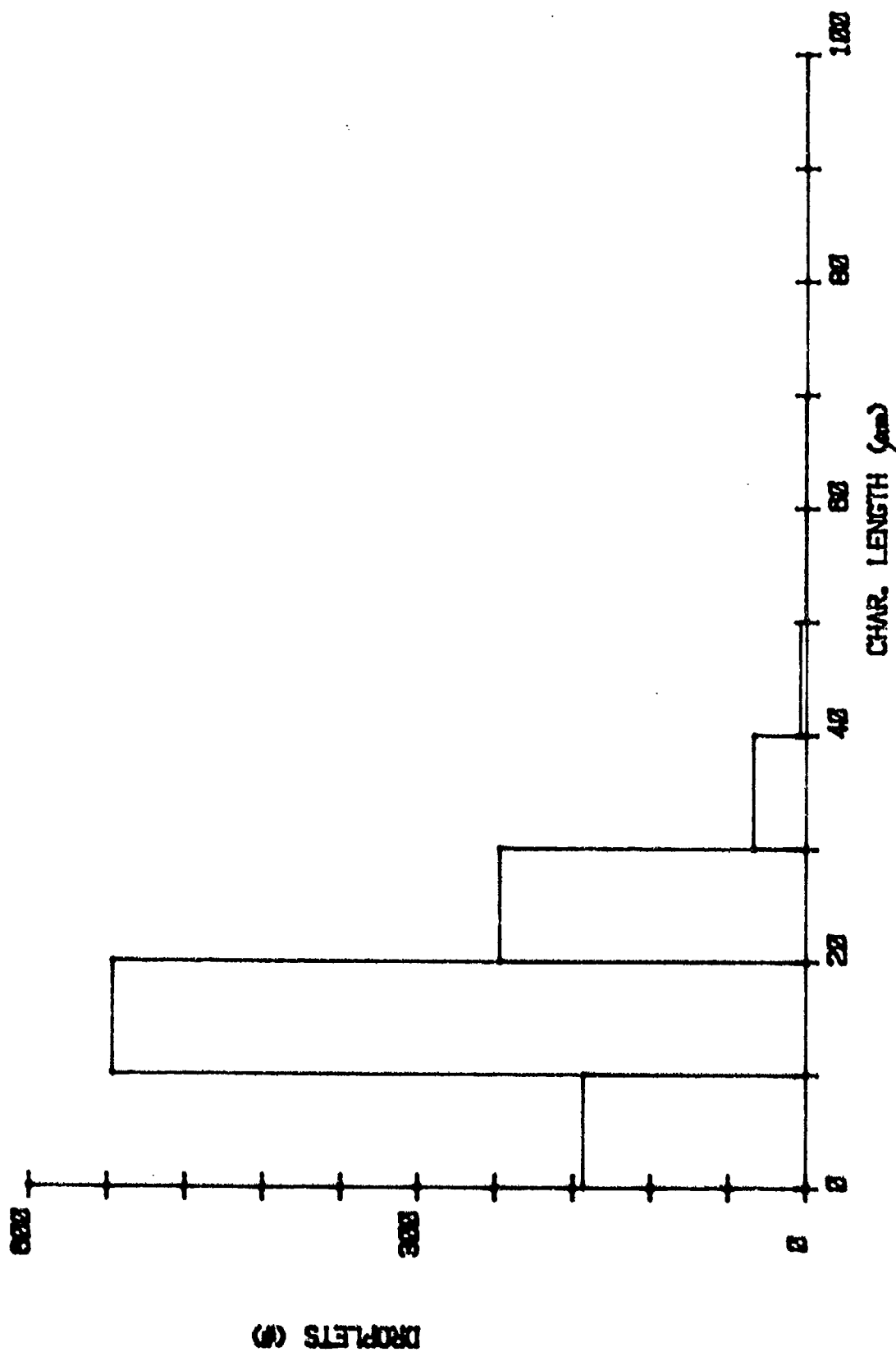


Figure 75. Histogram of drop characteristic length observed at the FCTA ignition source; Jet A + 0.20% FM-9 fuel, 6.1 atm accumulator pressure (fire suppression test failed under these conditions).

TABLE 4
Drop Statistics Summary: Mini Wing Shear and FCTA Tests

	Mini Wing Shear ($\dot{m}_f = 0.6 \text{ kg s}^{-1}$)				FCTA	
	Airspeed = 60 m s ⁻¹ 0.3% FM-9 Pass	Airspeed = 96 m s ⁻¹ 0.30% FM-9 Fail	Airspeed = 60 m s ⁻¹ 0.25% FM9 Pass	Airspeed = 60 m s ⁻¹ 0.20% FM-9 Margin/Fail	0.25% FM-9 Pass	0.20% FM-9 Fail
SMD/ μm (Volume/Area Computation)	37	320	94	180	290	89
SMD/ μm (characteristic length computation)	36	230	120	100	43	280
Drop Number ₃ Density/mm ³	1.7	3.2	2.0	1.7	30	4.5
Drop Pseudo Volume Density, %	0.46	7.9	6.4	10	0.35	2.3

most support to the spray combustion. This trend is also apparent in figures 74 and 75 displaying FCTA pass and fail drop data. Again (note the difference in Y axis scales) a significant difference exists in the raw number of particles of the size most supportive of combustion. The Sauter diameter indicates only a weighted average size not the total number of particles present. Also, since very large fuel droplets occur with very low frequency, their contribution to the SMD, which is significant, is very difficult to measure. Current trends indicate that both drop density and SMD combine to determine mist flammability. The low quality of the digital images used and some remaining software problems still existing at the time of writing do not permit formation of definite conclusions at this stage. Figure 76 permits a direct comparison of drop population changes at various pass/fail boundaries. Clearly in the FCTA tests for which the data were most reliable, the relative increase in number density is dramatic proceeding from the pass to the fail case.

6.3 Nozzle Flow Behavior

Engine manufacturer fuel nozzle specifications are stated in terms of fuel flow rate for each operating condition³. Because only fuel pressure is measured during operation of the nozzle spray facility, calibration of flow rate as a function of nozzle pressure drop was carried out. Results of this calibration for Jet A, AMK, and partially degraded AMK are shown in figures 77 and 78.

These data were reduced by representation in terms of the Reynolds number, Re , and the nondimensional pressure head, $2\Delta P/\rho V^2$. The pressure drop used is that between the storage tank and the nozzle exit plane, and thus represents the drop in pressure across various orifices and through some piping. The velocity is the average of that in the inlet piping. Similarly, the Reynolds number is based on the pipe diameter between the tank and the nozzle.

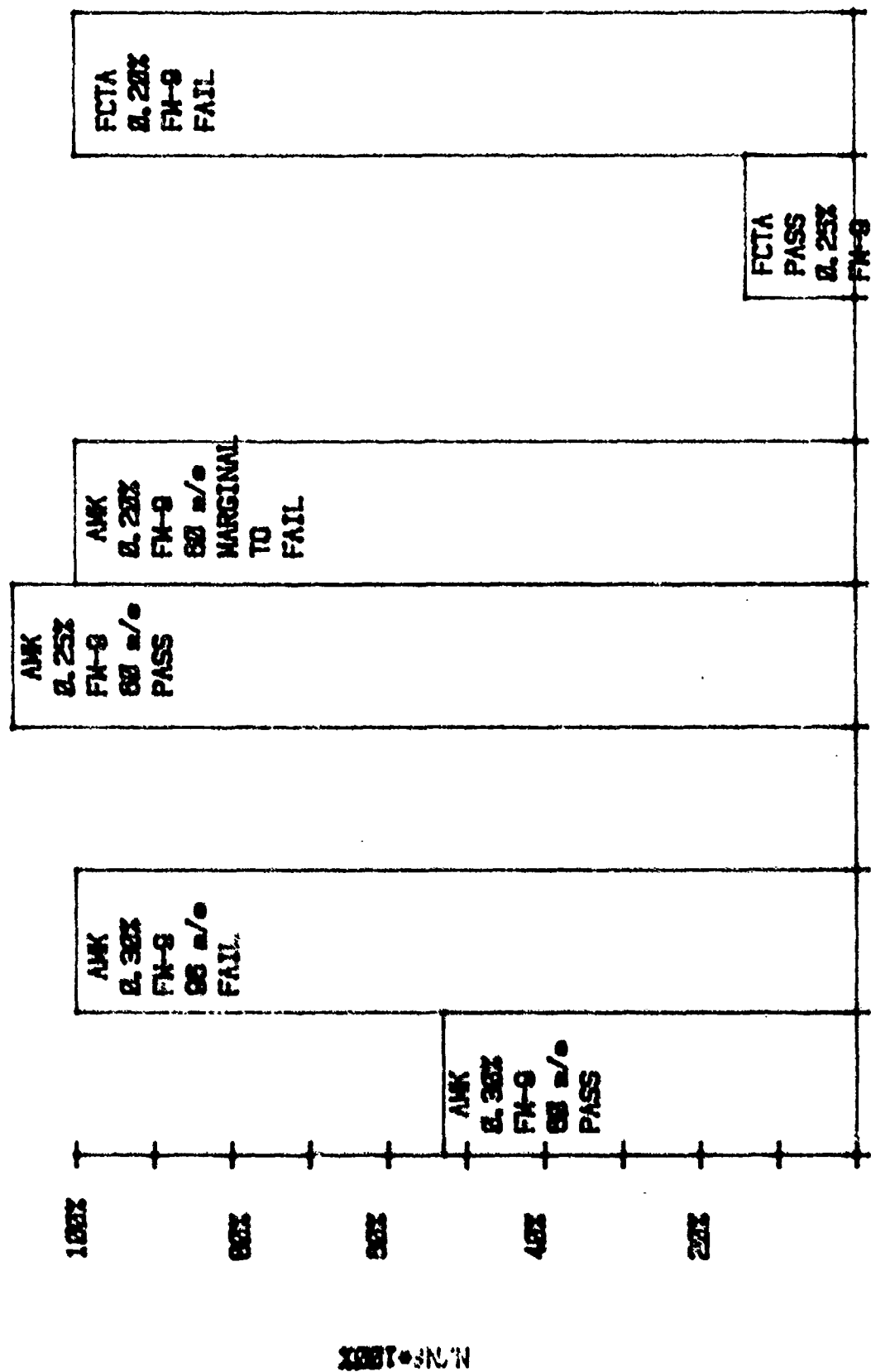


Figure 76. Total number of droplets identified for each test, normalized to the number identified in the test corresponding to failure of the fire suppression test.

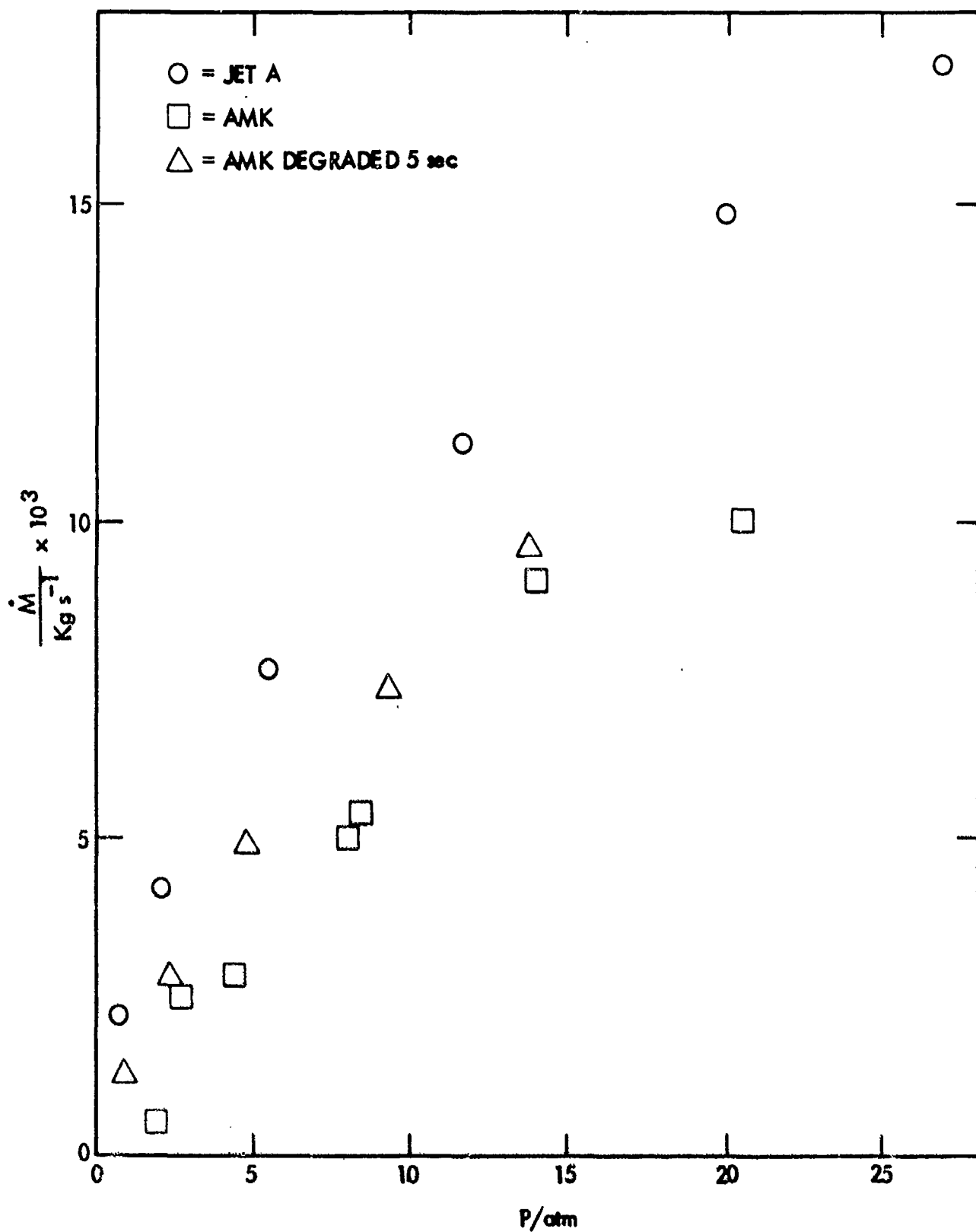


Figure 77. Fuel mass flow rate as a function of nozzle pressure drop; primary jet.

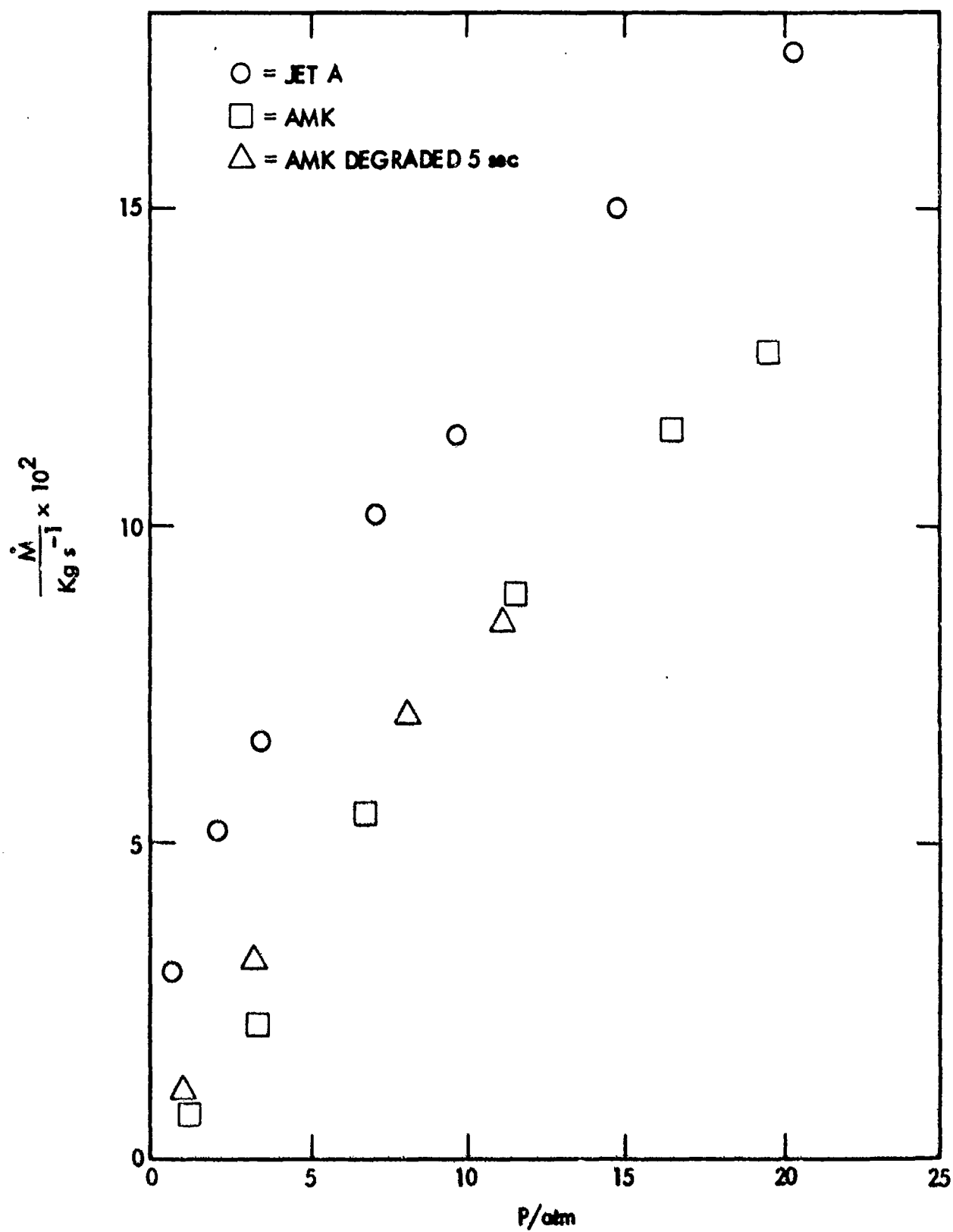


Figure 78. Fuel mass flow rate as a function of nozzle pressure drop; secondary jet.

It should be clear that the pressure drop is the result of combined viscous effects (including pipe and orifice flows) and flow acceleration. These data are plotted in figure 79.

Because the AMK will shear thicken as it flows through the pipes and nozzle, a measure of the pressure drop may equate to a measure of the shear thickening ability of the AMK. Since the AMK's ability to shear thicken is tied to its degradation level, it is suggested that a measure of the pressure drop across an arbitrary but specified flow network will equate to a measure of degradation level. To test this hypothesis, it is suggested that if the only reason for changes in the pressure drop at constant flow rate is shear thickening, then by just choosing the correct value of the viscosity, all of the pressure drop data plotted as a function of Reynolds number will fall on one line. The results of this attempt are shown in figure 80. The effective viscosity chosen for each sample to yield the best fit is shown in the accompanying table. The fact that the data do conform to one line just by varying the viscosity demonstrates that viscosity changes (shear thickening) alone do explain flow differences. If other, unrelated changes in the flow (e.g., turbulent transitions) were taking place, the curves would be shaped differently besides possibly being shifted, and simple variation in viscosity would not collapse the data.

The outcome of this analysis is that measurement of pressure drop across a flow circuit where shear thickening may occur might be a sensitive measure of fuel degradation level. The sensitivity of this technique is indicated by the very wide range of apparent viscosity shown in figure 80. It is suggested that in future work, a device should be built specifically for this purpose to further test the feasibility of this concept.

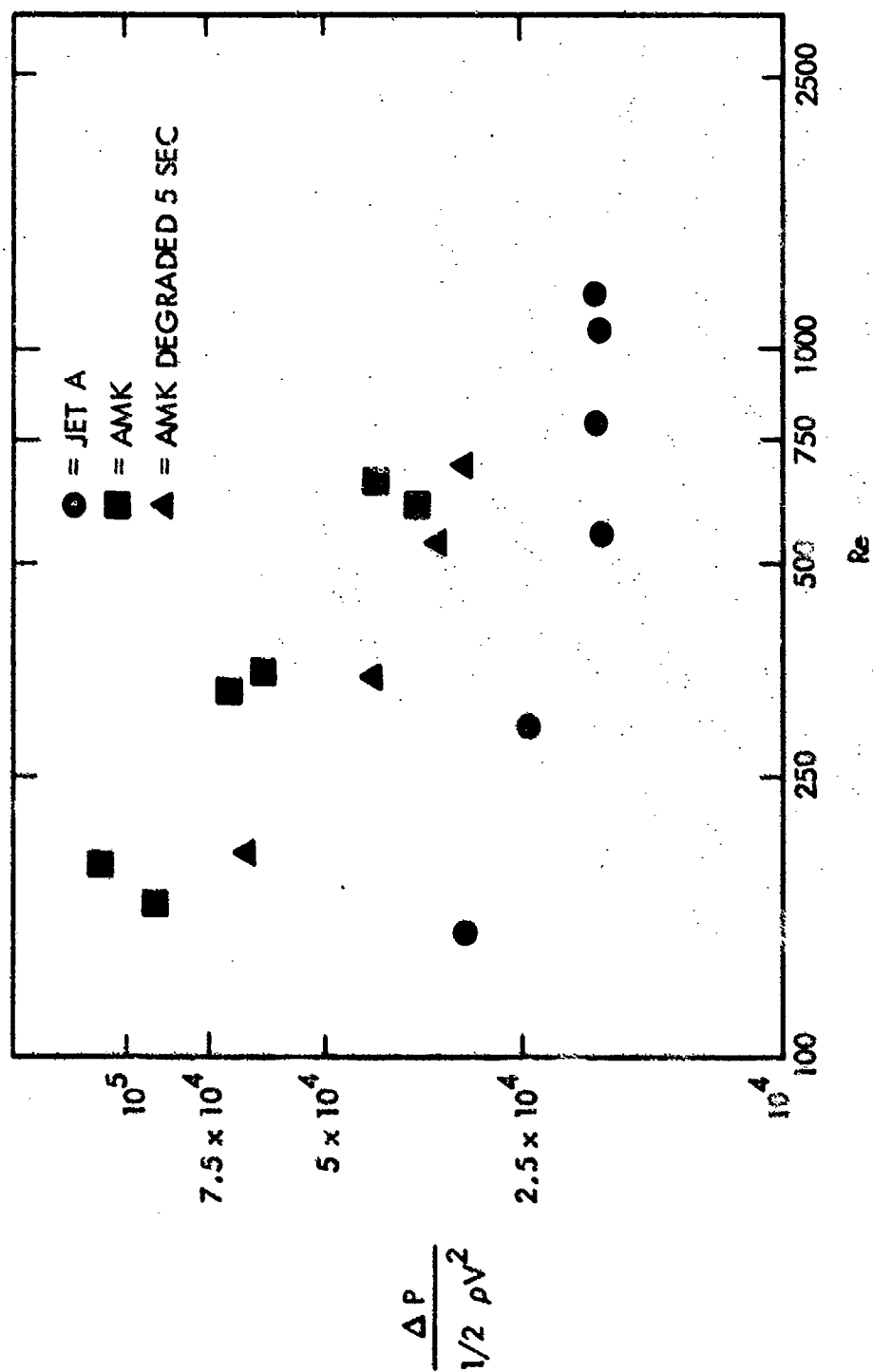
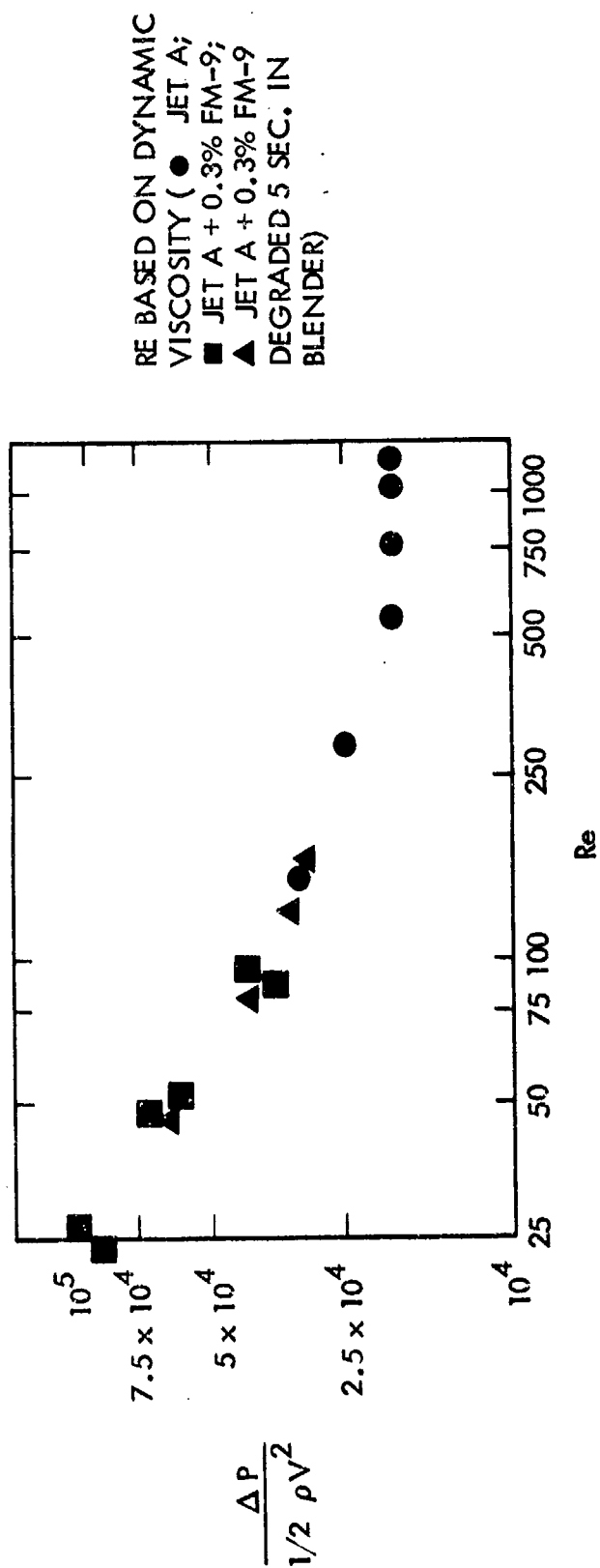


Figure 79. Dimensional analysis of nozzle calibration data.



SAMPLE	LOW SHEAR VISCOSITY, $\frac{\eta}{Pa \cdot s} \times 10^3$	DYNAMIC VISCOSITY, $\frac{\eta}{Pa \cdot s} \times 10^3$
JET A	1.76	1.76
JET A + 0.3% FM-9	2.79	19.3
JET A + 0.3% FM-9 DEGRADED 5S IN BLENDER	2.61	11.5

Figure 80. Reduction of nozzle calibration data using derived viscosity values.

VII. SCALING CONSIDERATIONS

7.1 Dimensional Analysis

The experimental variables that affect the breakup and atomization of the fuel jet include at least the following:

U_{∞} = airspeed

\bar{U}_L = area average velocity of the fuel jet

d = dimension of the fuel jet orifice

The physical constants that are important to breakup and atomization include at least the following:

ρ_A = air density ($\approx 1.22 \text{ kg/m}^3$)

ρ_L = fuel density ($\approx 800 \text{ kg/m}^3$)

η_A = viscosity of air ($\approx 1.8 \times 10^{-5} \text{ kg/m s}$)

η_L = viscosity of fuel ($\approx 3.1 \times 10^{-3} \text{ kg/m s}$ for 0.3% FM-9)

σ = surface tension of fuel ($\approx 0.028 \text{ Nt/m}$ for Jet A)

The non-Newtonian properties of the modified fuel, of course, dominate the dynamics of droplet formation. The information necessary for characterizing these non-Newtonian properties must include the critical shear rate, $\dot{\gamma}_C$, for the rapid onset of shear thickening. For 0.3% FM-9 at 24°C , $\dot{\gamma}_C = 3100 \text{ s}^{-1}$ (ref. 41).

After dimensional analysis, these nine parameters can be arranged into four independent nondimensional variables and two constants. We have selected the following groupings:

$$\frac{\delta}{d} = \text{Fn} \left\{ \frac{\bar{U}_L}{d\dot{\gamma}_C}, \frac{U_{\infty}}{d\dot{\gamma}_C}, \rho_L \frac{\bar{U}_L d}{\eta_L}, \rho_A \frac{U_{\infty}^2}{\sigma}; \rho_L/\rho_A, \eta_L/\eta_A \right\} \quad (7.1)$$

Thus, the droplet size, δ , depends on the following nondimensional variables:

a) $\frac{\tau_L}{d\dot{\gamma}_c} = De_L$, the hydrodynamic Deborah number of the fuel jet. It is

the ratio of liquid shearing rate to the critical shearing rate.

b) $\frac{U_\infty}{d\dot{\gamma}_c} = De_A$, the aerodynamic Deborah number, which is the ratio of

mean aerodynamic shearing rate to critical shearing rate.

c) $\frac{\rho_L U_L d}{\eta_L} = Re_L$, the hydrodynamic Reynolds number of the fuel jet

which is the ratio of inertial hydrodynamic forces to viscous forces.

d) $\rho_A \frac{U_\infty^2 d}{\sigma} = We$, the Weber number, which is the ratio of aerodynamic

forces to the surface tension of the fuel.

Any other nondimensional grouping of the parameters can be expressed in terms of these four. To this level of complexity, at least, we expect any two facilities and generating conditions to exhibit dynamic similarity if their values of De_L , De_A , Re , and We are in the same range.

7.2 Fuel Jet Parameter Space

The two nondimensional variables that should most affect the dynamic similarity of the fuel jets are hydrodynamic Reynolds number and hydrodynamic Deborah number. In figure 81 the FAA wing shear facility, the JPL wing shear facility, and the Flammability Comparison Test Apparatus (FCTA) are each located in the parameter space formed by Re_L and De_L .

With the FAA facility, the highest Deborah numbers and Reynolds numbers are produced at a massflow of 227 l/s (60 gal/s) through a 7.6 cm (3 inch) orifice. The lowest values are produced at a massflow of 38 l/s (10 gal/s) through a 19.7 cm (7 3/4 inch) orifice⁵.

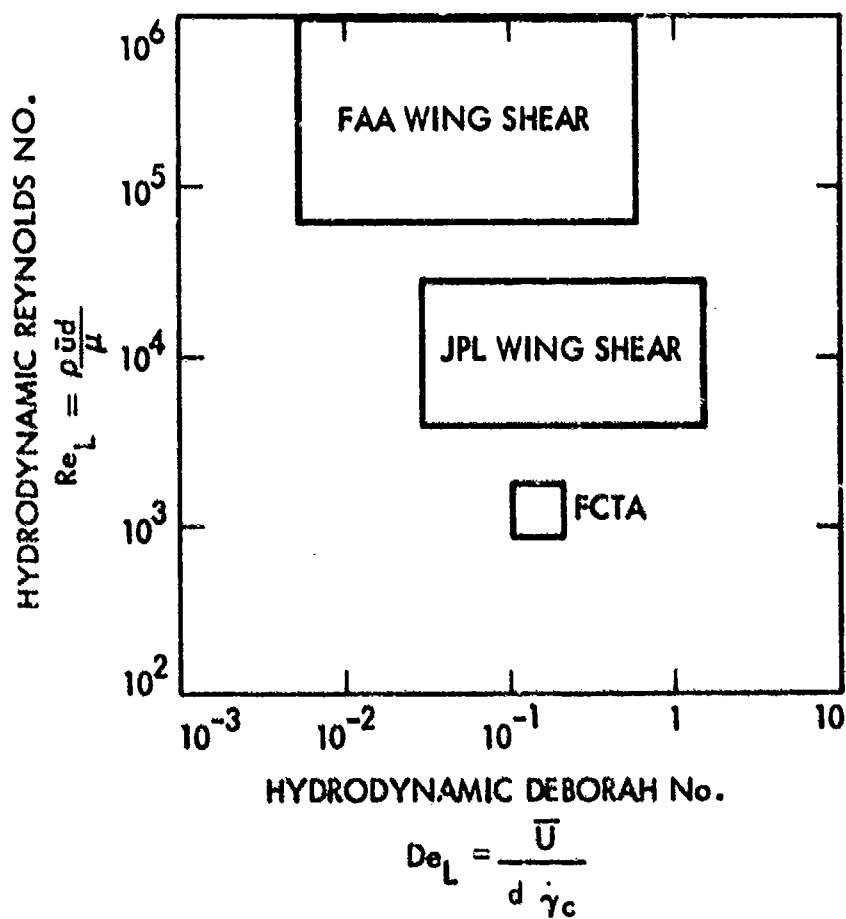


Figure 81. Parameter space relevant to fuel jet similarity. The Deborah number is referred to the fuel critical shear rate, $\dot{\gamma}_c$.

With the JPL facility the highest Deborah and Reynolds numbers were produced by a massflow of 0.68 l/s through a 0.79 cm orifice. The lowest were produced by a massflow of 0.28 l/s through a 2.15 cm orifice.

The massflow range tested with the FCTA was 11-22 g/s (speed control range of 400-950).

Based on figure 46, there is no change in the overall flammability as the liquid jet Reynolds number increases. At high Reynolds numbers typical of the FAA facility the jet breakup should be dominated by inviscid mechanisms. However, the relationship between Reynolds number and droplet size is not well understood. Most of the available research however is concerned with the breakup of low Reynolds number jets, such as occur in nozzle sprays. Flow visualizations by Hoyt and Taylor⁵¹ of high Reynolds number water jets indicate that the largest droplets scale with the jet instability which depends on jet speed and diameter. In their study the jet stability was insensitive to aerodynamic shearing and was insensitive to the addition of a drag reduction polymer. However, the size of the smallest droplets changes with aerodynamic shearing and with the polymer additive. These observations suggest that the distribution of droplet sizes is related to the distribution of turbulence scales in the jet. The range of turbulence scales becomes larger with increasing Reynolds number. This may tend to decouple the size of the smallest droplet from the size of the jet. For example, the smallest turbulence scale within the liquid jet is the dissipation scale, ζ_L , which is a function only of the kinematic viscosity ($\nu_L = \eta_L/\rho_L$) and the turbulent dissipation rate ϵ_L ⁴².

$$\zeta_L = (\nu_L^3/\epsilon_L)^{1/4} \quad (7.2)$$

The turbulence level, u_L' , and the dissipation rate, ϵ_L , are dominated by the largest turbulence scales represented by Λ_L , the integral scale. For example,

if the liquid was newtonian and the jet turbulence was isotropic and homogeneous,

$$\epsilon_L \sim (u'_L)^3 / \Lambda_L. \quad (7.3)$$

In that case

$$\zeta_L \sim \Lambda^{1/4} (\nu_L / u'_L)^{3/4} \quad (7.4)$$

and so the smallest scales increase much slower than the largest scales.

Strictly speaking, these scaling arguments apply only to Newtonian fluids. The presence of the FM-9 polymer will directly influence the smallest turbulence scales and, if the Deborah number is large, the jet dynamics will be modified as well. Experiments with the JPL wing shear facility and the FCTA over a range of Deborah number (figure 81) indicated that the hydrodynamic Deborah number did not have a strong effect on flammability (figure 45). In larger facilities the Deborah number will be smaller and so should influence the flammability even less.

Experimental evidence suggests no strong link between liquid jet Reynolds number and flammability. Figure 46 shows no apparent trend in flammability for either the mini wing or FCTA tests. Since drop size variations should influence the flammability, this indicates little relationship between the size of drops generated and the fuel jet diameter or Reynolds number.

The viscous terms in the turbulent energy budget are modified by the non-Newtonian effects, and so the turbulent dissipation is directly affected by the FM-9 additive. One way of visualizing this effect is in terms of the critical shearing rate, $\dot{\gamma}_c$, of the modified fuel. If the turbulent shearing rate, $\partial u_L / \partial x$, exceeds $\dot{\gamma}_c$ then rapid shear thickening should reduce the production rate of turbulent energy. Roughly speaking, turbulence production is equal to the turbulence dissipation rate, ϵ_L , which is expected to be limited by the critical shearing rate. We recall that for a Newtonian liquid

$$\epsilon_L = 15\nu_L \left(\frac{\partial u_L'}{\partial x} \right)^2 \quad (7.5)$$

It is then expected that the product $15\nu_L(\dot{\gamma}_C)^2$ will, in the case of AMK, form an upper bound on ϵ_L . The dissipation scale, ζ_L , would then be bounded by

$$\zeta_L = [\nu_L^3/\epsilon_L]^{1/4} > [\nu_L/3.9 \dot{\gamma}_C]^{1/2}$$

For the case of 0.3% FM-9, and $\dot{\gamma}_C = 3100 \text{ s}^{-1}$, eqn. (7.5) suggests that the dissipation scale is bounded by 20 μm . This number is quite small and may indicate that the inequality is much too conservative.

Based on these arguments, we would expect that the formation of small turbulence scales within the fuel during breakup is promoted by the combination of large hydrodynamic Reynolds number and small Deborah number.

7.3 Aerodynamic Parameter Space

The two nondimensional variables that most affect the external aerodynamics of fuel atomization are Weber number and aerodynamic Deborah number. In figure 82 the three facilities are located in this parameter space.

The range of airspeeds for the FAA facility was 57-82 m/s and the range of jet dimensions was 7.6-19.7 cm. The range of airspeeds used in the JPL facility was 60-100 m/s and the range of jet dimensions was 0.79-2.15 cm. The range of airspeeds tested in the FCTA was 50-80 m/s (5.1-6.8 atm plenum air pressure). The full-scale estimates were based on an airspeed of 80 m/sec and a jet dimension of 1 m.

The dynamics of jet breakup involve scales on the order of the jet dimension. In all three facilities the Weber numbers were large enough that surface tension was probably unimportant at those large scales. Turbulence scales are much smaller, however, and it is probably the combination of surface tension, turbulent shearing, and shear thickening that determines the

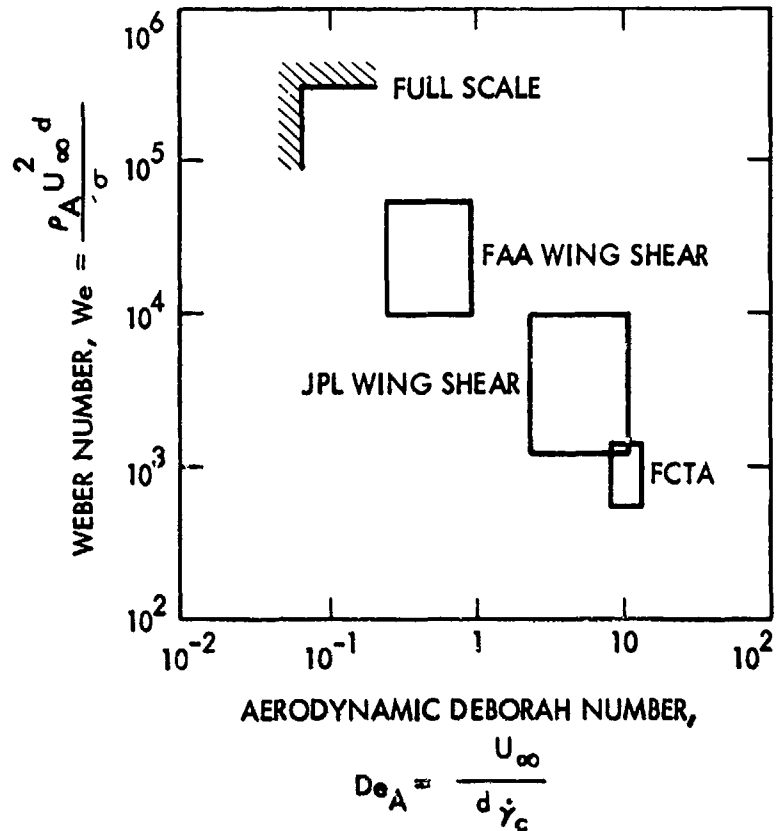


Figure 82. Parameter space relevant to aerodynamic similarity of fuel breakup and atomization. The Deborah number is referred to the fuel critical shear rate, $\dot{\gamma}_c$.

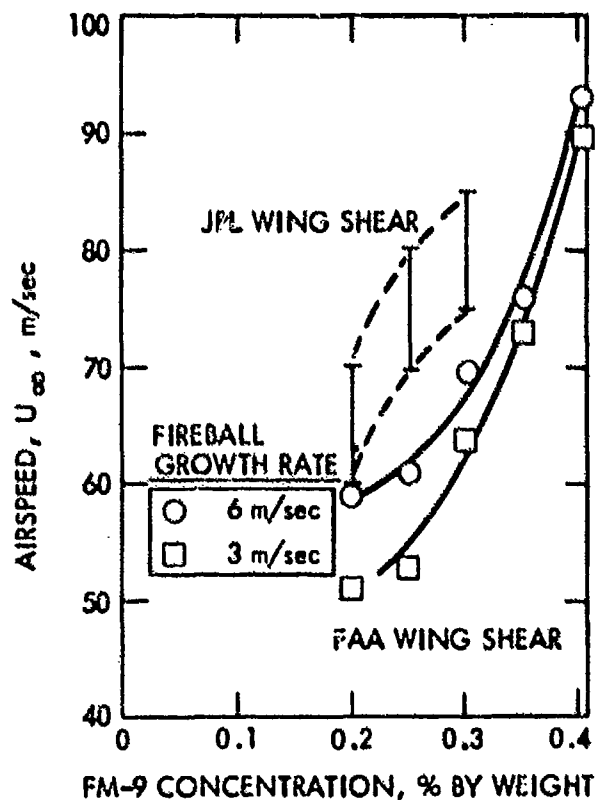


Figure 83. Comparison of pass-fail boundaries measured in JPL and FAA wing shear experiments. JPL data, from figure 50; FAA data, from ref. 5. Each set of curves denotes boundaries of marginal regions.

ultimate drop size. In that case, the combination of parameters that provides the poorest antimisting performance is large Reynolds number, large Weber number and small Deborah number.

Based on those arguments the FAA facility might be expected to produce less fire protection than the JPL facility or the FCTA. The primary flammability measurement used with the FAA facility was the growth rate of the fireball. Salmon reports that growth rates greater than 6 m/sec were considered to be in the "fail" region. His data is replotted in figure 83 as a pass/-fail boundary of airspeed vs. polymer concentration. Pass/fail bounds for the JPL facility, from figure 38, are also replotted here as a pass/fail boundary. In the JPL facility, fire protection is apparently provided up to airspeeds that are 10-15 m/sec higher than those of the FAA facility. The spread may be even larger than that because the FAA airspeeds are nominal values, and the actual airspeeds at the location of the wing were somewhat less. This comparison must be viewed with some caution, of course, because different flammability measures were used.

7.4 Aerodynamic Shearing

External aerodynamic shearing of the fuel by the airstream will always dominate the hydrodynamic shearing of the fuel by the orifice because fuel velocities are much smaller than the air velocity. Consequently, aerodynamic shearing is very important to the antimisting properties of the modified fuel. These shearing rates are difficult to scale because they are dominated by turbulent shearing at high Reynolds numbers. The turbulent shearing rate is directly related to the turbulence dissipation rate ϵ . If the turbulence is isotropic at viscous scales, from equations (7.3) and (7.5)

$$\frac{\partial u'^2}{\partial x} \sim \epsilon / 15\nu_A \sim (u')^3 / 15\Lambda_A \nu_A. \quad (7.7)$$

if the turbulence is isotropic at the largest scales (subscript A) and where u' is the rms turbulent velocity. This and subsequent Newtonian relations are employed as approximations for lack of a full rheological description of AMK and because non-Newtonian equivalents have not, in many cases, been devised. Their use only for estimation of the relative importance of various terms is further justified if the viscosity, ν , is considered that of the liquid at its local state (i.e., not necessarily the zero shear viscosity). The ratio of turbulent shearing rate to mean shearing rate is then

$$\frac{\partial u' / \partial x}{U_{\infty} / d} \approx \left[\frac{u'}{U_{\infty}} \right]^{3/2} \left[\frac{d}{15\lambda_A} \right]^{1/2} \left[\frac{U_{\infty} d}{\nu_A} \right]^{1/2}. \quad (7.8)$$

For turbulent shear flows, the turbulence level is typically in the range 10-20%. If $u' / U_{\infty} = 0.1$,

$$\frac{\partial u' / \partial x}{U_{\infty} / d} \approx 0.01 [d / \lambda_A]^{1/2} \left[\frac{U_{\infty} d}{\nu_A} \right]^{1/2}. \quad (7.9)$$

If the integral scale of the turbulence scales with d , the physical dimension of the fuel spill, then the ratio of turbulent to mean shearing depends on the Reynolds number of the flow. For Reynolds numbers, $U_{\infty} d / \nu_A$, greater than 10^4 turbulent shearing should dominate. Thus, we may conclude that all of the experiments (FCTA, mini wing, FAA wing shear) lie within the range of dominant turbulent shearing. In that respect they accurately model the aerodynamic breakup of an aircraft fuel spill. If any jet scaling effects do have importance they would tend to result in larger drops appearing in larger scale crashes. Since smaller drops form a more flammable mist, the laboratory experiments would be more critical than an actual crash in terms of flammable mist suppression.

VIII. Conclusions

- 1) The diverse nature of the jet breakup scaling parameters prevents perfect replication of all aspects of the full scale event simultaneously in the laboratory.
- 2) Theoretical scaling arguments suggest that the smallest relative drop sizes, d/Δ , should be observed for large Reynolds and Weber number flows with low Deborah numbers.
- 3) A reduced temperature has been defined which quantifies the extent of fuel mist combustion.
- 4) A correlation between increased drop size and increased fire suppression has been found for some FCTA tests. More information such as drop density is needed to fully characterize mist flammability. This information is, in principle, available in the photographs made for this investigation.
- 5) Mini wing shear and Flammability Comparison Test Apparatus (FCTA) results are found to be similar in terms of the reduced temperature.
- 6) Increasing reduced temperature with increased fuel/air ratio (e.g., figures 39 and 50) indicate that combustion is vapor limited (lean burning regime) in both the FCTA and mini wing shear devices.
- 7) A relationship of the form $\theta = \alpha c^{\beta}$ appears to exist between the antimisting polymer concentration, c , and the extent of combustion expressed as the reduced temperature, θ (α and β are constants) (see figure 47).

- 8) Radiometric calorimetry has been found capable of resolving a fire suppression pass/fail boundary. Thermocouples offer the advantages of increased spatial resolution and decreased sensitivity to the presence of radiating surfaces.
- 9) Measurement of apparent viscosity of the fuel during induced shear thickening in a nozzle flow provides a sensitive measure of polymer degradation level.

APPENDIX I

DERIVATION OF THE NON DIMENSIONAL TEMPERATURE, θ , AS A MEASURE OF FLAMMABILITY

Consider an experiment performed with certain air and fuel mass flow rates, with a resulting temperature rise reading in the combustion region. If the experiment is repeated identically except with a doubling of the air mass flow rate, a different temperature rise may be observed. Is this change in the temperature rise due to some fundamental difference in the fuel atomization and combustion as airflow increases, or is the temperature rise changed simply because in the second test the combustion region was diluted with twice the airflow of the first test? Furthermore, how may different flammability tests performed with widely varying fuel/air ratios be compared? Since the effect of antimisting additives is to isolate much of the fuel in large, incombustible fuel drops, the net antimisting effect is to decrease the fraction of the total fuel available which burns, i.e. the flammability.

For all of these reasons, comparison of different tests within one experiment, comparison of tests between different facilities, and measurement of the fraction of the total fuel available which is burned, a more sophisticated measure of flammability than simple temperature or heat flux measures is introduced. This new measure of temperature is called θ , the nondimensional temperature. Simply stated it is the ratio of the temperature rise observed in the combustion region to the temperature rise one would observe in the combustion region if all of the available fuel would have burned.

For many practical open combustion calculations the equation

$$\dot{q}_f = C_p T^* \dot{m} \quad (A-1)$$

is used where C_p is an average specific heat value of the combustion gases, T^* is the measured temperature rise and \dot{m} is the mass flow rate of combustion

gases. The term q_f is given by

$$\dot{q}_f = \dot{q}_f \dot{m}_f^* \quad (A-2)$$

where \dot{q}_f is the fuel "heat of combustion" and \dot{m}_f^* is the rate of fuel injection, assuming all fuel injected is burned. Thus

$$\dot{q}_f \dot{m}_f^* = C_p T^* \dot{m} \quad (A-3)$$

The further assumption is then made that C_p of the combustion products is approximately equal to C_p of air, and similarly that \dot{m} of the combustion gases is equal to \dot{m} of air. Both of these assumptions are based on the large flux of air compared to fuel typical of most combustion systems. The assumption is particularly valid in experiments like the mini wing shear where Air/Fuel mass flow ratios are typically greater than 10.

The temperature rise we would then expect to reach if the fuel injected were completely burned is then given by

$$T^* = \frac{\dot{q}_f \dot{m}_f}{C_{p(\text{air})} \dot{m}_{\text{air}}} \quad (A-4)$$

If only a fraction, x , of \dot{m}_f burns then by following an identical derivation to that which leads to eqn. (4) we reach an expression for a new temperature rise given by

$$T = \frac{\dot{q}_f (x \dot{m}_f^*)}{C_{p(\text{air})} \dot{m}_{\text{air}}} \quad (A-5)$$

T is the temperature rise measured when only a fraction, x , of the total fuel injected, \dot{m}_f^* , actually burns. T is thus the temperature rise measured in actual combustion experiments where complete combustion of the fuel does not occur. If we form the ratio T/T^* , we can measure x , the fraction of fuel burned, because

$$\frac{T}{T^*} = \frac{\frac{q_f(X\dot{m}_f^*)}{C_{p(\text{air})}\dot{m}_{\text{air}}}}{\frac{q_f\dot{m}_f}{C_{p(\text{air})}\dot{m}_{\text{air}}}} = x,$$

thus

$$x = \frac{T C_{p(\text{air})} \dot{m}(\text{air})}{q_f \dot{m}_f^*}.$$

The right hand side of the equation contains quantities which are available either during the experiment by direct measurement (T is the measured temperature rise, \dot{m}_f^* is the fuel mass flow rate, and $\dot{m}(\text{air})$ is the air mass flow rate) or from compiled tables of thermodynamic properties ($C_{p(\text{air})}$ and q_f). Thus for any given combustion experiment we can compute what the extent of combustion is. We see immediately too that if nothing is altered except a doubling of the air flux, and the extent of combustion, x , does not change, then T will be half as large which answers a question posed early in this discussion. Obviously for any experiment, $0 < x < 1$ because at $x = 0$, $T = 0$, and at $x = 1$, $T = T^*$, the maximum theoretically achievable temperature rise.

Finally, for convenience we define

$$\theta \equiv x$$

and call θ the "nondimensional temperature" or the "reduced temperature" because it is a measure of the achieved temperature rise compared to the maximum achievable temperature rise for the particular experimental conditions.

In the AMK program, we may now compare the flammability of fuel in, for example, a low airspeed test, to the flammability in a high airspeed test. We see that if T is the same for both tests, we may earlier have been tempted to

conclude that the flammability was the same. Now it is realized that in the high airspeed test, $\dot{m}_{(air)}$ is much greater, thus x or θ must be much greater for the same T , the same measured temperature rise. Finally, for these two hypothetical tests we may confidently conclude that at high airspeed, more of the available fuel was burned, and thus even though the observed temperature was no different, the fuel spray was more flammable at the high airspeed than at the low airspeed. This is because flammability in this context means how readily does the fuel burn and what fraction of the total available fuel is combusted, to which the answer is in measurement of θ .

Appendix II

AMK QUALITY CONTROL MEASUREMENTS

A special run procedure, described below, was devised for the FCTA to enable rapid relative flammability measurement for quality control tests only. This procedure yields a single point flammability measure and is not intended to replace standard FCTA procedure. It was incorporated because of the need to carry out testing on a routine basis.

1. The speed control dial which controls the fuel injection rate is set at 900.
2. The air accumulator tank pressure which determines the air flow rate is allowed to climb to 6.5 atm (95 lb in⁻²). This reading is taken at the highest pressure reached during the run and occurs just as the air begins to flow through the nozzle.
3. Temperature measurements are made with a 0.76 mm diameter lead, chromel-alumel thermocouple. The probe is placed level with and 25cm downstream of the exit flange tip, Thermocouple readings are made with a strip chart recorder set so that a 1 mm deflection (the minimum resolvable) corresponds to a 24° temperature change.
4. A series of runs is performed until these tests yield results consistent within the measuring precision of $\pm 12^{\circ}\text{C}$.
5. A photograph is taken of each run, exposed 9 seconds after the set switch is tripped. Kodacolor print film (400 ASA, 35 mm size) is exposed for 0.008 of a second at f2. The 35 mm camera equipped with a 55mm focal length lens is placed 3 meters from the apparatus so that the edge of the FCTA is visible on one side and as much of the flame is visible as possible. These provide a qualitative record of each test.

References

1. T.I. Eklund and W.E. Neese, Design of an Apparatus for Testing the Flammability of Fuel Sprays, FAA Report FAA-RD-7854 (1978).
2. A.M. Ferrara, Laboratory Scale Testing of Modified Fuels, FAA report to be published.
3. A. Fiorentino, R. De Saro and T. Franz, An Assessment of the Use of Antimisting Fuel in Turbofan Engines, NASA Report No. NASA-CR-165258 pp. 42-43, 1980.
4. A.H. Yavrouian, M. Sarbolouki and V. Sarohia, Influence of Liquid Water and Water Vapor on Antimisting Kerosene (AMK), JPL Technical Publication (to be published).
5. R.F. Salmon, Wing Spillage Tests Using Antimisting Fuel, FAA Report FAA-CT-811, 1981.
6. Alan Williams, Combustion of Sprays of Liquid Fuels, Gresham Press, England, 1976.
7. B.J. Azzopardi, "Measurement of Drop Sizes," Int. J. Heat Mass Transfer, 22, pp. 1245-1279, 1979.
8. A.R. Jones, "A Review of Drop Size Measurement," The Application of Techniques to Dense Fuel Sprays," Prog. Energy Combustion Sci., 1, pp. 225-234, 1977.
9. C.G. McCreath and J.M. Beer, "A Review of Drop Size Measurements in Fuel Sprays," Applied Energy, 2, pp. 3-15, 1976.
10. A. Burkholz, "Messmethoden zur Tropfengrößenbestimmung" Chemie Ingenieur Technik, 45, p. 1, 1973.
11. J.G. Skifstad, "Fuel Spray Measurements with an Imaging-Type Atomizer," AIAA paper No. 81-0262, AIAA, New York, 1981.
12. Arthur H. Lefebvre, "Airblast Atomization," Prog. Energy Combustion Sci. 6 pp. 233-261, 1980.
13. V. Sarohia and R.F. Landel, Influence of Antimisting Polymer in Aviation Fuel Break-up, AIAA Paper No. 80-1287, presented at 16th Joint Propulsion Conference, Hartford, CT 1980.
14. R.L. Stoker, "A Method of Determining the Size of Droplets Dispersed in a Gas," J. Appl. Phys., 17, pp. 243-245, 1946.
15. K. R. May, "The Measurement of Airborne Droplets by the Magnesium Oxide Method," J. Sci. Instr., 27, pp. 128-130 1949.

16. R.D. Stainer and C.D. Stow, "Direct Methods for the Measurement of Small Water Drops," New Zealand J. Sci., 19, pp. 135-143, 1976.
17. R. Biggs and R.L. McMillan, "The Errors of Some Haematological Methods As They Are Used in the Laboratory," J. Clin Path. 1, p. 269, 1948.
18. H. Heywood, "A Comparison of Methods of Measuring Microscopical Particles," Trans. Inst. Mining Metall., 55, p. 391 1945.
19. S. Nukiyama and Y. Tarasawa, Experiment on the Atomisation of Liquid by Means of an Airstream., III, Distribution of the Size of Drops, Trans. Soc. Mech. Engrs., Japan 4, p. 86, 1938.
20. H.H. Watson and D.F. Mulford, "A Particle Profile Test Strip for Assessing the Accuracy of Sizing Irregularly Shaped Particles with a Microscope", J. Appl. Phys., Suppl. No. 3 S., 105, 1954.
21. B.L. Wignall, "Operator Interaction with the Quantimet 720 Image Analyser," in Remote Sensing Data Processing, University of Sheffield, pp. 129-142, 1975.
22. H.C. Simmons and D.L. Lapers, "A High Speed Spray Analyzer for Gas Turbine Fuel Nozzles," Paper presented at the ASME Gas Turbine Conference, Cleveland, Ohio 1969.
23. Jean Graf, "Sizing with Modern Image Analyzers" in Particle Size Analysis, J.D. Stockham and E.G. Fochtman eds. Ann Arbor Science Publishers, Michigan, pp. 35-44, 1978.
24. Kenneth R. Castleman, Digital Image Processing, Prentice Hall, New Jersey, 1979.
25. William B. Green, "Future Trends in Image Processing Software and Hardware," Proceedings of 1979 Machine Processing of Remotely Sensed Data Symposium, IEEE 1979.
26. Jean J. Lorre, Application of Digital Image Processing Techniques to Astronomical Imagery 1980, Publication 81-8, Jet Propulsion Laboratory, 1981.
27. P.R. Paluzzi, R.D. Toaz, D.G. Roberts, R.C. Searle and Michael L. Somers, "Computer Rectification and Mosaicking of Side-Looking Sonar Images," paper presented at the Offshore Technology Conference, Houston, Texas, 1981.
28. A.B. Kahle, D.P. Madura and J.M. Soha, "Middle Infrared Multispectral Aircraft Scanner Data: Analysis for Geological Applications," Applied Optics, 19, pp. 2279-2290, 1980.
29. J.F. Benton, A.R. Gillespie and J.M. Soha, "Digital Image Processing Applied to the Photography of Manuscripts," International Review of Manuscript Studies, 33, pp. 40-55, 1979

30. F.W. Skidmore and R.E. Pavia, "Techniques for Examining Drop Size Spectra in Water Sprays and Clouds," Aeronautical Research Laboratories (Australia) Paper No. AR-001-729, 1979.
31. V. Caloi and V. Castellani, " 'Il Quantimet' Come Analizzatore Di Immagini Astronomiche," Societa Astronomica, Italiana, Memorie 47, pp. 85-93, 1976.
32. De Anza Systems, Inc., IP 5000 Image Array Processor, Data sheet, 118 Chariot Avenue, San Jose, CA 18131.
33. Boller and Chivens PDS Microdensitometer Program Manual, Boller and Chivens Division, The Perkin-Elmer Corporation, 915 Meridian Avenue, South Pasadena, CA 91030, November 1973.
34. Paul L. Jepsen, The Software/Hardware Interfacer for Interactive Image Processing at the Image Processing Laboratory of the Jet Propulsion Laboratory; Proceedings of the Digital Equipment Computer Users Society, Las Vegas, Nevada, December 1976.
35. G.A. Hotham, "Particle Sizing by Laser photography," meeting paper, Society of Photo-Optical Instrumentation Engineers, San Diego, California 1977.
36. "Kodak Technical Pan Film (Estar - AH Base) 50-115," Data Release P-255, Eastman Kodak Company, 1977.
37. "1981-82 Photo Products Reference Guide", Consumer, Professional and Finishing Markets Publications No. R-50, p. 28, Eastman Kodak Company, 1981.
38. J. B. Seidman and A. Y. Smith, VICAR Image Processing System--Guide to System Use, Publication 77-37, Revision 1, Jet Propulsion Laboratory, December, 1979.
39. "Equipment Specification for the Dicomed Model D48 Color Film Recorder" Dicomed Corporation, Minneapolis, Minnesota, May 1976.
40. William B. Green, "Computer Image Processing - The Viking Experience," 18th Annual IEEE Chicago Spring Conference on Consumer Electronics, Chicago, Illinois, June 1977.
41. T.J. Peng and R.F. Landel "Rheological Behavior of Progressively Shear Thickening Solutions," J. Appl. Phys., to be published.
42. H. Tennekes and J. L. Lumley, A First Course in Turbulence, MIT Press, 1972.
43. Kuo-Hui Wang, "Atomization and Drop Size Distribution of Polymer Solutions," PhD Thesis, Syracuse University, 1969.
44. Gyorgy Sitkei, "Contribution to the Theory of Jet Atomization", NASA Technical Translation, F-129. 1963.

45. Lane, W.R., and Green, H.L, The Mechanism of Drops and Bubbles, Survey in Mechanics, Edited by Batchelor, G.K., and Davies, R.M., Cambridge University Press, 1956.
46. Simpkins, P.G., and Bales, E.L., "Water-Drop Response to Sudden Acceleration," J. Fluid. Mech., Vol. 55, Part 4, 1972, pp. 629-639.
47. Merrington, A.D, and Richardson, E.G., "The Breakup of Liquid Jets," The Proceedings of The Physical Society, Vol. 59, Part 1, January 1947, pp. 1-13.
48. P.W. James, "On the Atomization of Elastico-Viscous Liquids," Rheol. Acta 15, pp. 238-241, 1976.
49. J.W. Hoyt, J.J. Taylor, and C.O. Range, "The Structure of Jets of Water and Polymer Solution in Air," J. Fluid Mech., 63 pp. 635-640, 1974.
50. Joseph A. Scheiz and Atol Pudhye, "Penetration and Breakup of Liquids in Subsonic Airstreams," AIAA J. 15, pp. 1385-1390, 1977.
51. J. W. Hoyt and J. J. Taylor, "Waves on Water Jets", J. Fluid. Mech., 83, pp. 119-237, 1977.